NASA CR-135017

QUIET CLEAN SHORT-HAUL EXPERIMENTAL ENGINE (QCSEE) AERODYNAMIC AND AEROMECHANICAL PERFORMANCE OF A 50.8 cm (20 in.) DIAMETER 1.34 PR VARIABLE PITCH FAN WITH CORE FLOW

August 1977

by

R.G. Giffin
R.A. McFalls
B.F. Beacher

Prepared For

National Aeronautics and Space Administration

NASA Lewis Research Center
NAS3-18021

TABLE OF CONTENTS

LIST OF ILLUSTRATIONS

LIST OF ILLUSTRATIONS (Continued)

LIST OF ILLUSTRATIONS (Continued)

LIST OF ILLUSTRATIONS (Concluded)

LIST OF TABLES

SECTION 1.0

SUMMARY

This report covers the aerodynamic and aeromechanical performance of a scale model of the QCSEE UTW fan and inlet, with simulated core flow, tested at the General Electric Corporate Research and Development Aero/Acoustic Anechoic Facility in Schenectady, New York. The 18-bladed fan rotor has adjustable-pitch capability, being mechanically resettable at zero speed. The 33 vanes comprising the bypass OGVs are positioned downstream of the rotor trailing edge a distance equal to 1.5 rotor tip chords, and are composed of five different geometries around the annulus to minimize flow distortions otherwise imposed by the pylon. Immediately downstream of the rotor, the fan hub flow passes under an annular ring with 96 OGVs, separated by a full-circumferential axial gap from the main flow splitter leading edge where the flow is divided into a bypass portion and a core portion.

In the forward thrust mode, tests were conducted at three rotor pitch settings of 0° (nominal) pitch, -5° (open) pitch, and +5° (closed) pitch. The fan was designed at the 0° (nominal) pitch setting to deliver a bypass pressure ratio of 1.34 at a total fan flow of 32.4 kg/sec (71.4 lbm/sec). It actually produced 5.5% less flow and 3.0% less pressure ratio at design speed on the operating line. At this condition, the estimated stage adiabatic efficiency was between 0.86 and 0.87, compared to the required design-point value of 0.867. Fan performance at +5° (closed) and -5° (open) exhibited the expected trends of speed lines shifting to higher flow as the pitch is opened and to lower flow as the pitch is closed. Peak efficiency is higher at the more closed rotor pitch settings and drops off less rapidly with speed increase than at the more open pitch settings. Conditions required to attain the takeoff and maximum cruise flow and pressure ratio would be met with a 2° to 3° more open rotor pitch setting than predicted. The fan hub (core) region produced a pressure ratio slightly in excess of the design-point objective of 1.23 and a (higher than predicted) adiabatic efficiency of 84%. Fan hub efficiency increased along all speed lines, for all pitch angles, as the fan was throttled; a peak was not reached in the flow range tested.

Basic fan performance data in the forward mode was obtained with a bellmouth inlet. Radial profiles of rotor pressure rise and efficiency show that throttling of the fan increased the tip pressure rise significantly more than in the hub portion, which is typical of low-radius ratio designs, but without any large changes in efficiency. Efficiency profiles remained smooth over the throttling range and free of any localized depressions which would indicate trouble areas. The simulated core inlet flow profiles were of the same shape and magnitude as predicted by design. Measured bypass-OGV loss levels were higher for the open 2 (-10° outlet flow angle) vanes and lower for the closed 2 (+10° outlet flow angle) vanes, consistent with the higher aerodynamic loadings of the open vane sets. Bypass-OGV performance was

found to be dependent upon the condition of the upstream flow, improving when the bypass ratio was reduced, and when high-loss flow which passes under the island and through the core OGV spills over the splitter and into the bypass duct. Circumferential-flow distortions induced by the nonaxisymmetric OGV row were small enough to avoid significant detrimental effects on the fan rotor. Bypass-ratio migrations had little effect upon the operation of the rotor and indicated satisfactory performance of the splitter at the nominal bypass ratio. Forward mode performance with the accelerating inlet showed no severe reduction in fan efficiency.

The operational limit line was determined for 0° (nominal) pitch angle only, and it met or exceeded the objective stall line at all speeds. Constant-speed stall margins were estimated as 20% at takeoff and 15% at maximum cruise speeds. The fan was tested with a tip radial distortion over the outer 40% of the inlet annulus area, having a value of the distortion severity parameter (maximum minus minimum pressure divided by maximum pressure) of 16% at the maximum flow. Stall limits for the distorted flow measured well above anticipated engine operating conditions at corrected speeds of up to 90%.

In the reverse thrust mode, tests were conducted in the reverse-through-stall direction at -95°, -100°, and -105° (open from nominal), and in the reverse-through-flat direction at +78° and +73° (closed from nominal). The accelerating inlet was used in place of the bellmouth to be more representative of the UTW engine configuration. Fan performance data revealed a significant change in operating line with rotor pitch angle change, and adiabatic efficiency was observed to fall off with increasing speed and flow. High rotor stress limited the vehicle maximum speed to 65% at a pitch setting of +78°, thus preventing attainment of the objective thrust in the reverse-through-flat pitch direction. However, the objective reverse thrust was obtained at each of the three pitch angles tested in the reverse-through-stall-pitch direction. The simulated core inlet experienced a total pressure loss equivalent to 1.25 times the dynamic pressure at the OGV leading edge, with a slight tip radial distortion in the pressure profile. Cycle calculations indicated that the engine system could produce the objective 35% reverse thrust even with the low core inlet recovery.

SECTION 2.0

INTRODUCTION

The General Electric Company is currently engaged in the Quiet, Clean, Short-Haul Experimental Engine Program (QCSEE) under Contract NAS3-18021 to NASA Lewis Research Center. A major objective of the QCSEE Program is to develop and demonstrate the technology required to meet the stringent noise requirements anticipated for commercial short-haul turbofan aircraft. The experimental program explores a wide range of pertinent technology involving both a variable-pitch under-the-wing (UTW) and a fixed pitch over-the-wing (OTW) propulsion system. Overall UTW engine detailed design characteristics are presented in Reference 1.

The UTW 50.8 cm (20 inch) Simulator test program was designed to evaluate, from a 1:3.55 scale model of the variable-pitch UTW fan, the aerodynamic and acoustic performance of the fan and inlet. Tests were conducted in the Aero/Acoustic Facility at the GE Research and Development Center in Schenectady, New York. This report covers complete details and data from the fan aerodynamic performance tests. Details of the UTW fan aerodynamic design may be found in References 2 and 3. Results of the acoustic performance tests are presented in Reference 4.

Basic UTW fan aerodynamic test objectives were to:

- Obtain base operating maps of the bypass and core portions of the fan at several conventional forward thrust rotor pitch settings.
- Determine the effect of off-design bypass ratio on performance.
- Determine the degree of circumferential-flow distortion induced by nonaxisymmetric bypass OGV and pylon configuration.
- Obtain fan performance in a hybrid-inlet environment.
- Evaluate fan forward thrust performance sensitivity to a tip radial inlet distortion.
- Determine reverse thrust performance over a range of through-flat-pitch and through-stall-pitch settings.
- Obtain core duct recovery and distortion characteristics during reverse pitch operation.

The data reported herein have been used to update the fan performance representation in the cycle deck prior to the full-scale engine operation. The procedure adapted for performance map definition for the UTW fan is discussed in Appendix B. Fan bypass performance and fan hub performance are treated separately in the forward mode, with adjustments made to the raw data to arrive at the most accurate estimates of stage efficiency. Further details of the fan map update, particularly in the reverse mode, are described in Reference 2. Aeromechanical response characteristics of the 50.8 cm (20 inch) fan are discussed in Appendix C.

LIST OF SYMBOLS

A	Effective flow area, m^2 ($in.^2$)
BPR	Bypass ratio
C_p	Specific heat at constant pressure
DV	Discharge valve
F_g	Gross fan thrust, N (lbf)
g	Gravitational constant
N	Rotational speed, rpm
P	Pressure, MN/m^2 ($lbf/in.^2$); total unless subscripted with s
R	Gas constant
r	Radius, cm (in.)
T	Temperature, K (° R); total unless subscripted with s
W	Weight flow, kg/sec (lbm/sec)
α	Absolute air angle, degrees
β	Rotor pitch setting (nominal or design setting = 0), degrees
γ	Ratio of specific heats
δ	Ratio: (total pressure)/(standard pressure)
η	Adiabatic efficiency
θ	Ratio: (total temperature)/(standard temperature)

Subscripts

F	Fan
h	Hub
m	Property of gas mixture
s	Static condition
t	Total (stagnation) condition
0	Ambient condition
1	Fan inlet
14	Outlet guide vane discharge
25	Core duct discharge

SECTION 3.0

FAN AERO DESIGN AND DESCRIPTION

The adjustable pitch 50.8 cm (20 inch) Simulator Fan is an exact linear scale (scale factor of 20.0 divided by 71.0) of the QCSEE Under-the-Wing (UTW) variable-pitch fan, except for the transition duct that guides the fan hub flow into the core compressor. Use of an existing facility drive shaft required minor modification to the simulated core flowpath in this region.

The aerodynamic design point for the UTW fan is selected midway between takeoff and altitude cruise engine operating conditions. Design-point corrected tip speed is 306 m/sec (1005 ft/sec) with an average fan-bypass pressure ratio of 1.34 and an average fan core pressure ratio of 1.23. For the simulator fan, the design-corrected fan flow is 32.4 kg/sec (71.4 lbm/sec) and the tip diameter is 50.8 cm (20 inch). The hub tip radius ratio is 0.443, which results in a specific flow of 199 kg/sec m^2 (40.8 lbm/sec ft^2) of annulus area. Design-point bypass ratio is 11.3, and the objective adiabatic efficiencies were 88.0% for the bypass portion and 78.0% for the core portion. Detailed UTW fan aero and mechanical design data are presented in Reference 2.

A cross section of the UTW engine fan is shown in Figure 1. There are 18 variable-pitch rotor blades with a solidity of 0.95 at the OD and 0.98 at the ID. Circumferential grooved casing treatment is incorporated over the rotor tip. The vane frame is positioned at an axial distance downstream of the rotor trailing edge equal to 1.5 true rotor-tip chords. The 33 vanes in the vane frame are composed of five different geometries around the annulus to minimize flow distortions that would otherwise be imposed by the pylon. The vane-to-blade ratio is 1.8. Immediately following the rotor, in the hub region, is an annular ring or island. The 96 OGVs for the fan hub flow are in the annular space between the underside of the island and the hub. A full-circumference axial gap separates the island trailing edge from the leading edge of the splitter which divides the flow into a bypass portion and a core portion. The island configuration was selected specifically to permit the attainment of high-hub-supercharging pressure ratio during forward pitch operation without causing a large core-flow-induction pressure loss during reverse pitch operation. There are six struts in the core flow transition duct.

Design rotor-tip relative Mach number is 1.13. The outer portion of the blade employs a profile shape that is specifically tailored to minimize excessive shock losses on the suction surface and still be compatible with the inlet flow and energy-addition requirements. Blade meanline shape and point of maximum thickness vary radially. The blade shape is similar to a double-circular arc profile in the hub region. Profile shapes at other radii are generally similar in appearance to the NASA multiple-circular arc sections in which a small percentage of the overall camber occurs in the forward

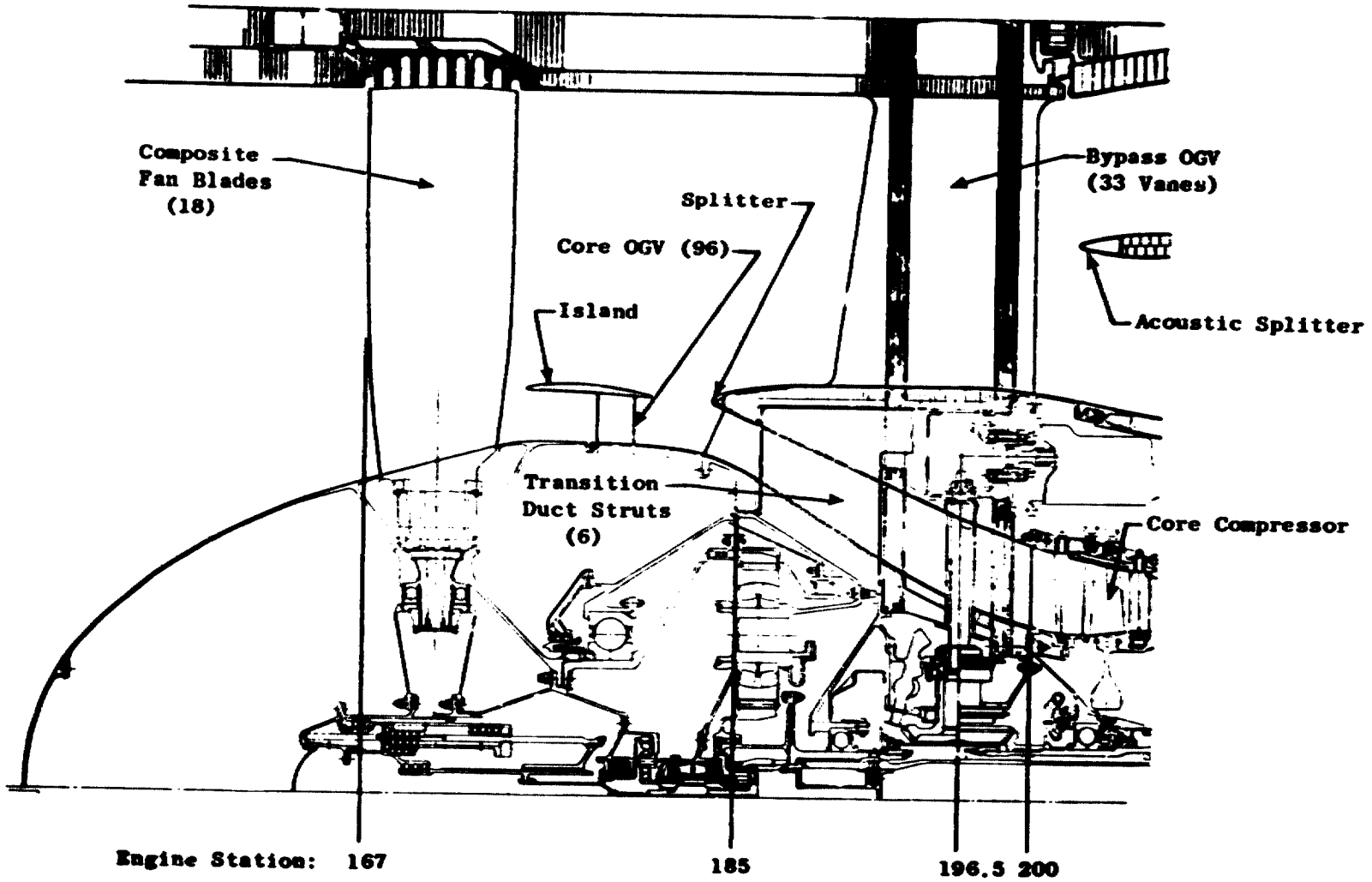

Figure 1. Cross Section of UTW Variable-Pitch Fan.

portion of the blade. Figure 2 shows a tip and hub section of two adjacent rotor blades in nominal (forward), reverse-through-feather (stall), and reverse-through-flat-pitch orientations.

The engine vane frame performs the dual function of an outlet guide vane for the bypass flow and a frame support for the engine components and nacelle. It is integrated with the pylon which protrudes forward into the vane row. A conventional OGV system turns the incoming rotor outlet flow to axial. However, the housing requirements of the pylon dictate a geometry in which the OGVs underturn approximately 10° on one side and overturn approximately 10° on the other side. The vanes must be tailored to downstream vector diagrams which conform with the natural flow field around the pylon to avoid creating velocity distortions in the upstream flow. Ideally, each vane would be individually tailored. However, to avoid excessive costs, five vane geometry groups were selected as adequate. Figure 3 is an unwrapped section at the ID of the vane frame which illustrates the different vane groupings and shows an approximate streamline pattern derived from an analysis of the circumferential flow field.

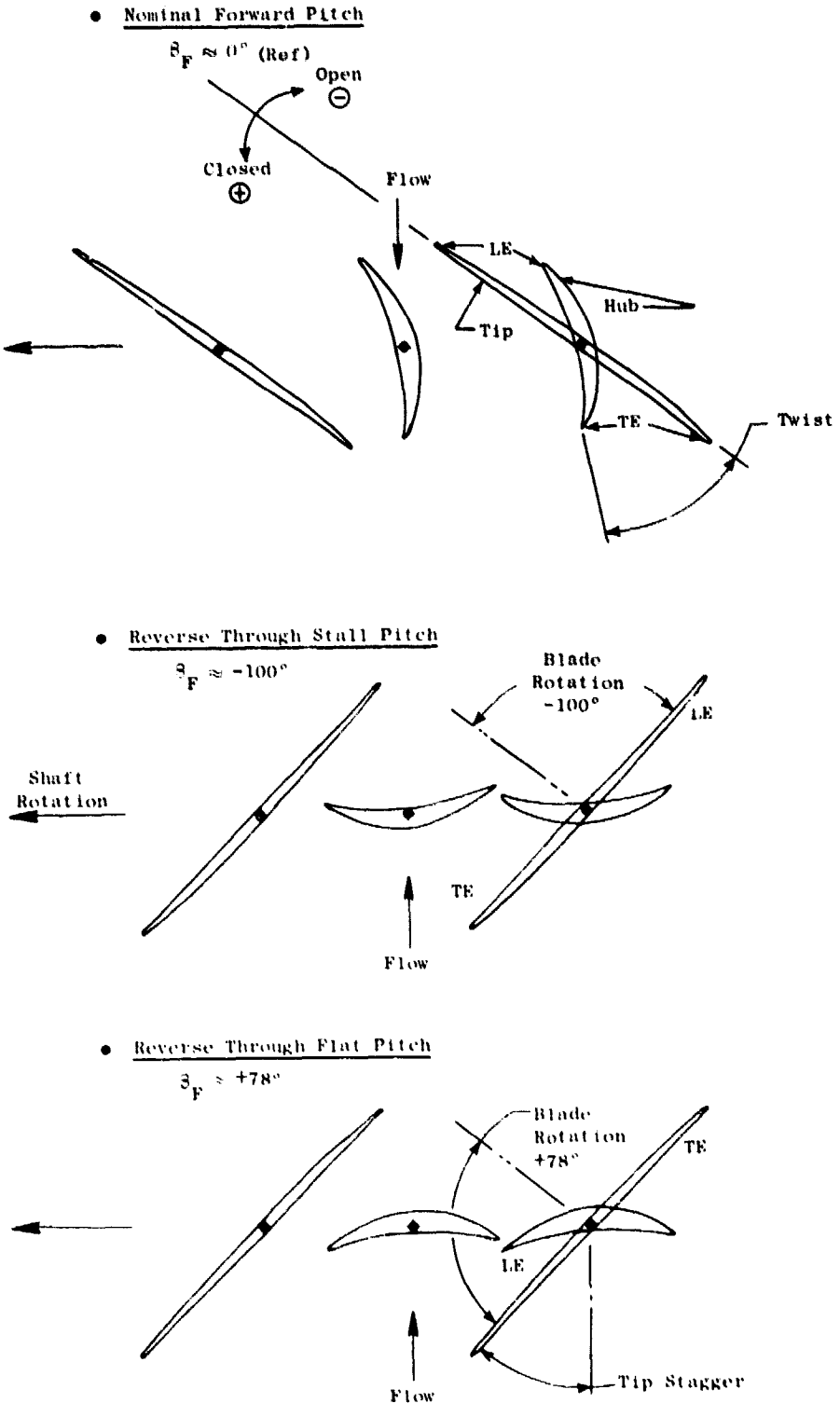

Figure 2. UTW Fan Blade Geometry at Different Blade Pitch Angle Settings.

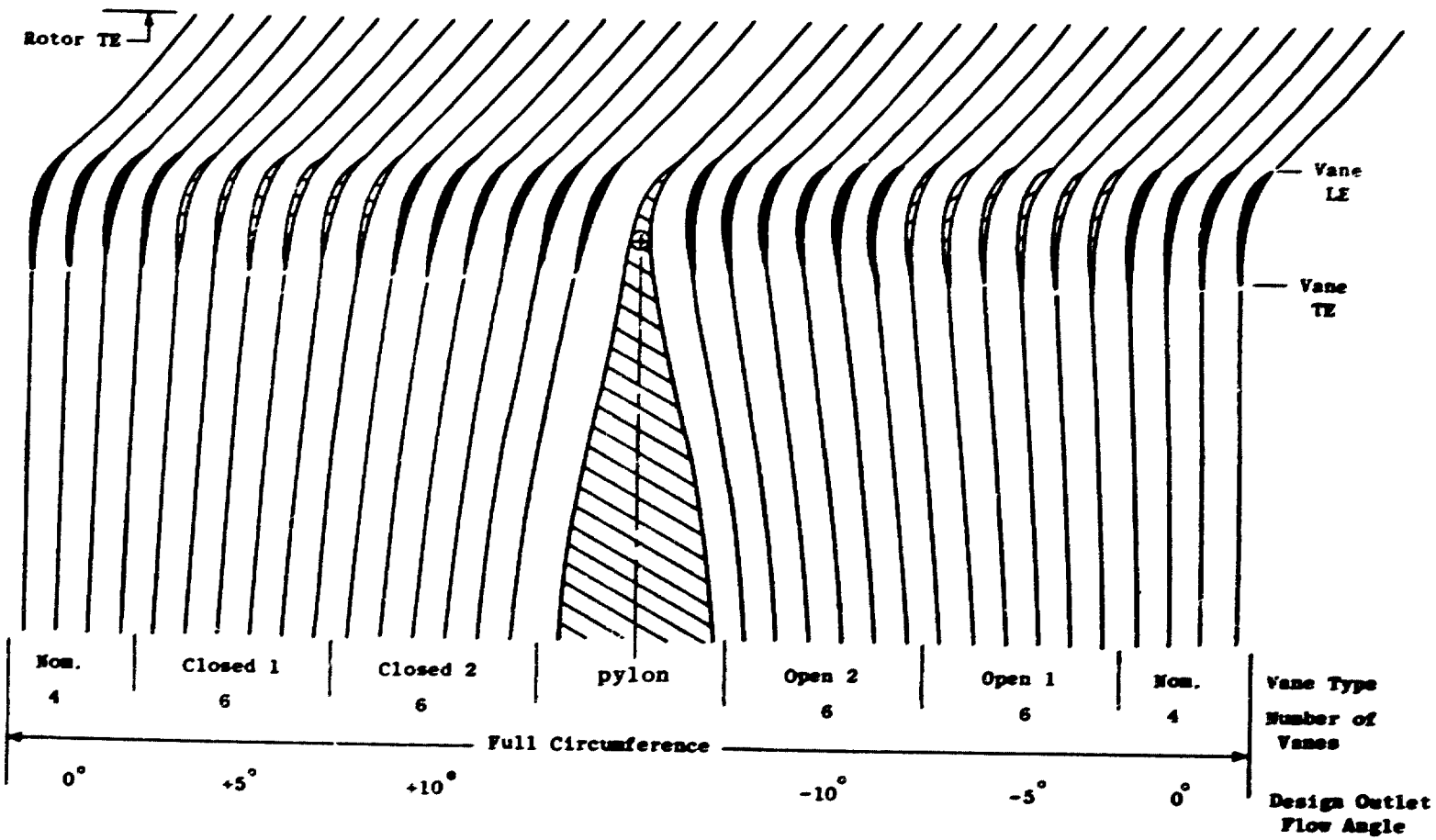

Figure 3. Vane Frame Unwrapped Section at ID.

SECTION 4.0

APPARATUS AND PROCEDURE

4.1 TEST FACILITY

Tests were conducted in the anechoic environment of the General Electric Corporate Research and Development Aero/Acoustic Facility in Schenectady, New York. A schematic view of the facility is shown in Figure 4, and a photograph of the facility is presented in Figure 5. It is comprised of:

- A 2500 HP drive system for speeds up to 15,000 rpm.
- An anechoic chamber approximately 10.67m (35 ft.) wide, by 7.62m (25 ft.) long, by 3.05m (10 ft.) high-designed for less than ± 1 dB standing wave ratio at 200 Hz. All walls, floor, and ceiling are covered with an array of 71.1cm (28 in.) polyurethane foam wedges.
- Porous walls for minimum inflow distortion to the fan when measuring inlet radiated noise.
- Mountings and drive system for the fan allowing evaluation of both forward and exhaust-radiated noise.
- Equipment for farfield inlet-radiated noise measurement on a 5.2m (17 foot) arc from 0° to 110° relative to the inlet centerline.

In the forward mode, inlet flow entered the test cell through the porous walls of the anechoic chamber. After passing through the fan, it was split at the fan discharge into a bypass portion and a core portion. The bypass flow was ducted radially outward through a horizontally-sliding cylindrical ring discharge valve and exited out the exhaust stack. The core flow was collected in a manifold and exhausted through two pipes, one on each side of the vehicle, to a set of pumps. These pumps were located outside the test chamber and independently controlled the core flow rate.

In the reverse mode, the incoming flow entered through the bypass exhaust stack. Part of this flow was discharged out the fan inlet, while the rest was swallowed by the core and discharged in the same manner as in the forward mode.

4.2 FAN TEST CONFIGURATION

The test vehicle featured adjustable-pitch fan blades that were mechanically resettable at zero speed. In the forward thrust mode of operation, tests were conducted with the blades set at nominal or 0° pitch, -5° (open) pitch, and +5° (closed) pitch. In the reverse thrust mode of operation,

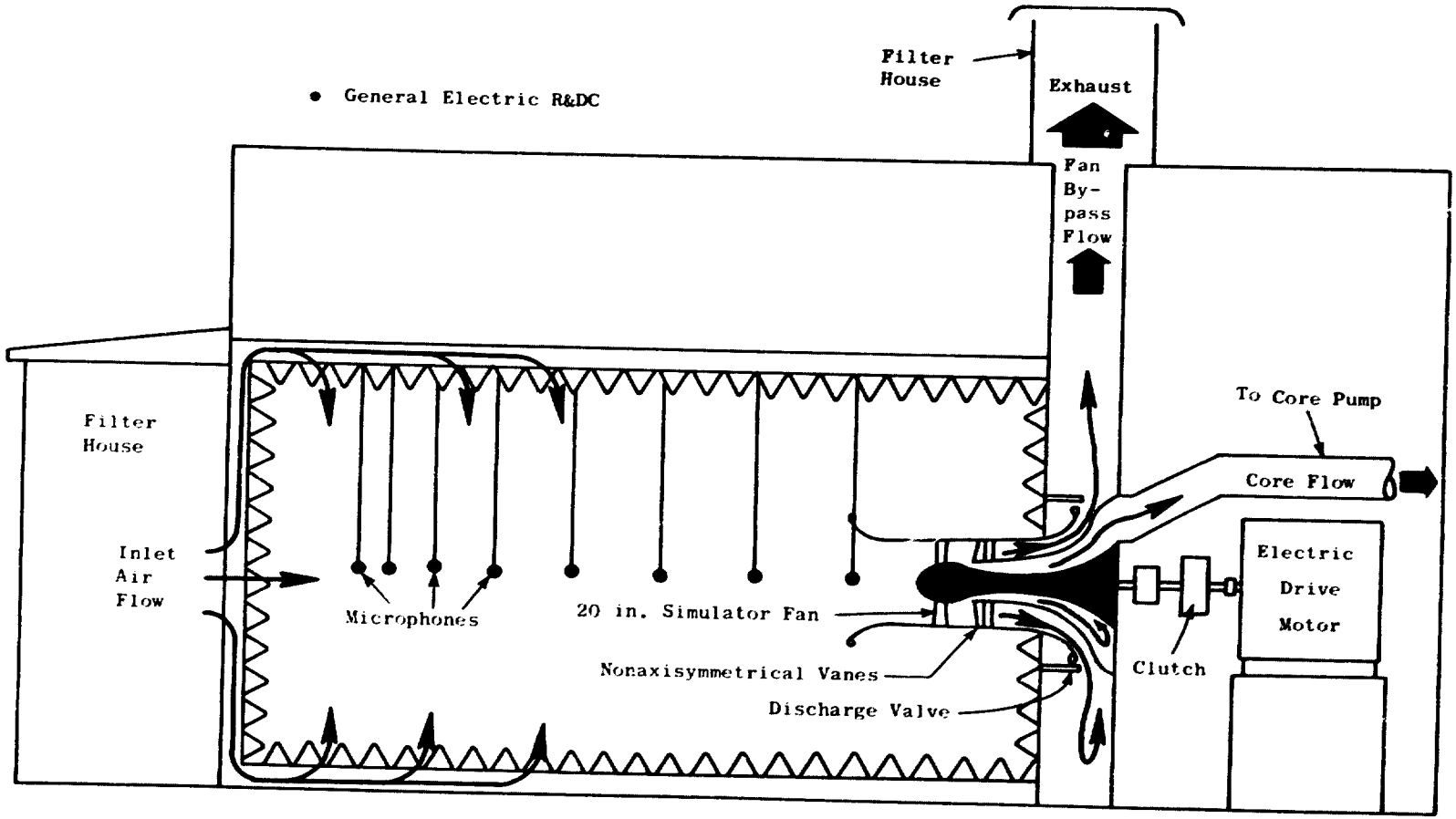

Figure 4. Schematic of GE Anechoic Chamber.

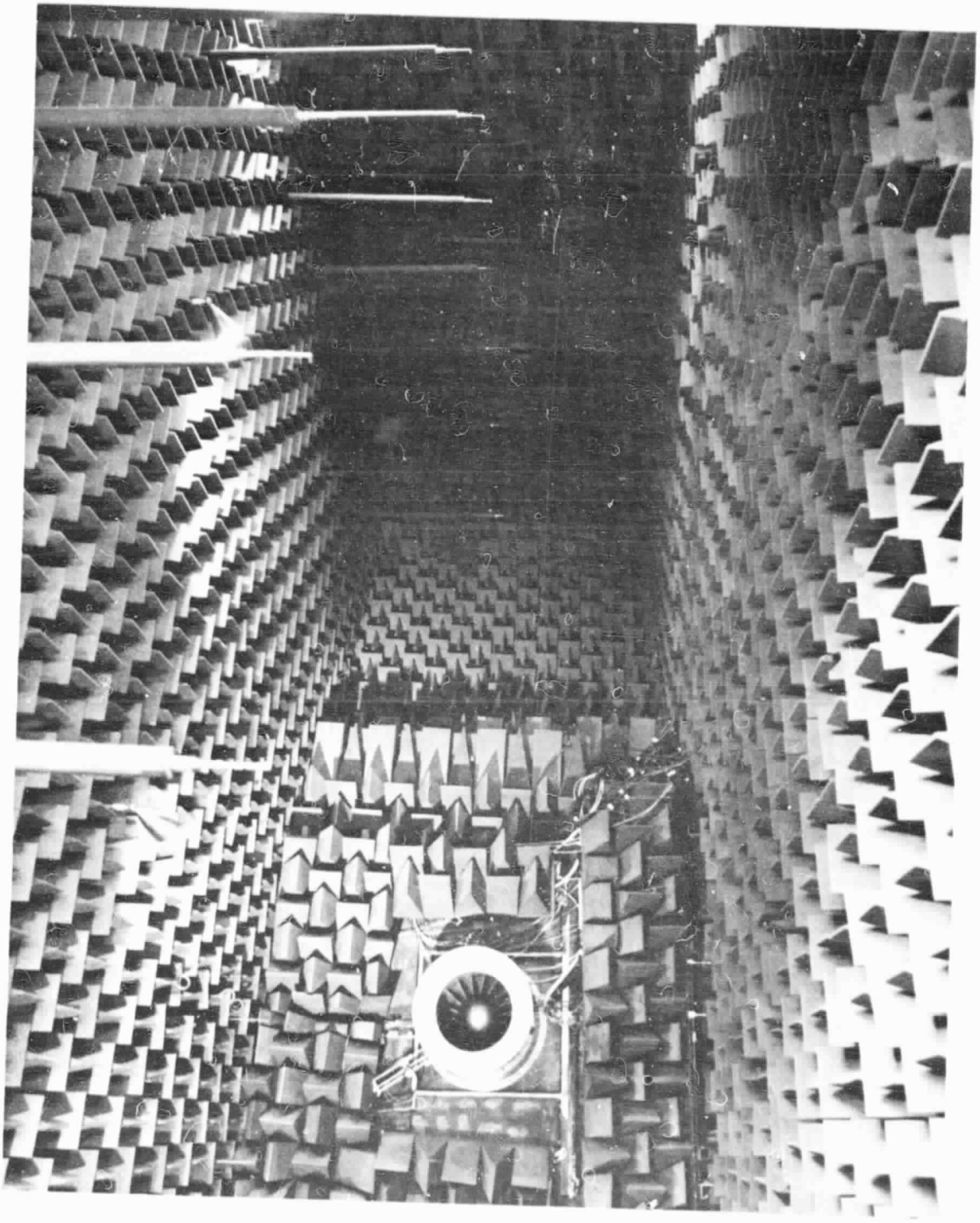

Figure 5. Photo of GE Anechoic Chamber.

tests were conducted in the reverse-through-stall direction at pitch settings of -95° (open), -100°, and -105°; and in the reverse-through-flat direction at pitch settings of +78° (closed) and +73°. All tests were conducted with the hardware as designed. The average vehicle running tip clearance at 100% speed was estimated to be 0.61 mm (0.024 in.).

Test vehicle cross sections are shown in Appendix A. Figure 44 illustrates the forward mode configuration with the inlet bellmouth that was used for most of this testing. The accelerating (high Mach) inlet was also tested briefly in the forward mode. Figure 45 presents the reverse mode test configuration with its accelerating (high Mach) inlet geometry. Both figures indicate flow directions and schematics of the exhaust ducting.

4.3 FAN AERODYNAMIC INSTRUMENTATION

The fan aerodynamic instrumentation used in both forward and reverse mode testing is described in Appendix A. In the schematics of the test vehicle (Figures 44 and 45), all rakes, probes, and static taps are identified. Fixed radial rakes were used to measure total pressures and total temperatures in the fan inlet, bypass duct, and core duct. Radially-traversing arc rakes were employed behind the bypass OGVs, in the forward mode only, to measure circumferential profiles of total pressure and total temperature at 7 discrete immersions. Cobra probe radial traverses were obtained at three axial positions downstream of the rotor in the forward mode, and both cobra and wedge probes were simultaneously traversed in the throat region of the accelerating inlet in the reverse mode. Cobra probes measured radial profiles of total temperature, total pressure, and flow angle, and the wedge probe measured radial distribution of static pressure and flow angle. Figure 46 shows, on an unwrapped ID section of the bypass OGVs, the circumferential locations at which the rakes and probes were positioned.

4.4 TEST PROCEDURE

The pretest plan called for the following testing to accomplish the fan aerodynamic goals:

- Clean inlet
  - Speed-line mapping for the nominal, +5°, and -5° rotor pitch angles. This range encompassed the important design and operating points.
  - Bypass ratio investigation.
- Distorted inlet
  - Speed-line mapping at nominal pitch angle with a tip-radial-distortion screen designed for approximately 15%.

$$\frac{P_{max}-P_{min}}{P_{max}}$$ at takeoff flow

- Accelerating (high Mach) inlet
  - Speed-line mapping at nominal pitch angle.
  - Reverse-pitch testing at three flat-pitch and three stall-pitch settings.

Discharge valve (DV) closure settings, plus blade speed and blade setting angle, were the independent parameters that uniquely determined a test condition. The core discharge valve position was uniquely related to that of the bypass DV for any given bypass ratio. Accordingly, it was appropriate, as well as convenient, to identify a given test condition by the bypass discharge valve closure setting. Figure 6 shows representative speed lines for the three forward-mode pitch angles tested and identifies a bypass discharge valve closure setting with each of the test points. The aerodynamic design point and two of the most significant engine fan operating conditions, takeoff and maximum cruise, are shown. Operating lines for these conditions are discharge valve closure settings of approximately 7.85, 7.70, and 7.88, respectively. These settings correspond to percent changes in fan discharge throttle area of 0, -11, and +2% respectively. Note that numerically larger discharge valve closure settings correspond to higher fan backpressure and lower fan flow. Thus, numerically lower values indicate a more open discharge valve and higher fan flow. Table I gives the discharge valve closure setting for each of the data points.

Pretest cycle calculations for the UTW engine system yielded bypass ratio as a function of fan speed and operating line. This relationship was used in selecting discharge valve closure settings for bypass and core flows for the actual test conditions. Separate bypass ratio-corrected speed schedules were followed for forward and reverse pitch testing.

The procedure for initial running of all forward-pitch configurations was as follows:

- Slowly accelerate to 50% speed at a DV closure setting yielding a slightly lower-than-nominal operating line.
- Adjust DV to nominal operating line and continue to maximum speed (not to exceed 110%), taking data in 10% speed increments from 70% up, along the nominal operating line and bypass ratio schedule.
- Map speed lines, beginning at 70% speed, by repeating the above procedure at other DV closure settings.

Reverse-pitch testing was performed along a sea level standard operating line only: the only two control variables were speed and core flow. Unlike the engine, which enters the reverse mode at speed by varying pitch angle, the simulator started from zero fan speed with the rotor blades already set in reverse pitch. The bypass discharge valve position was kept constant throughout the majority of reverse-pitch testing.

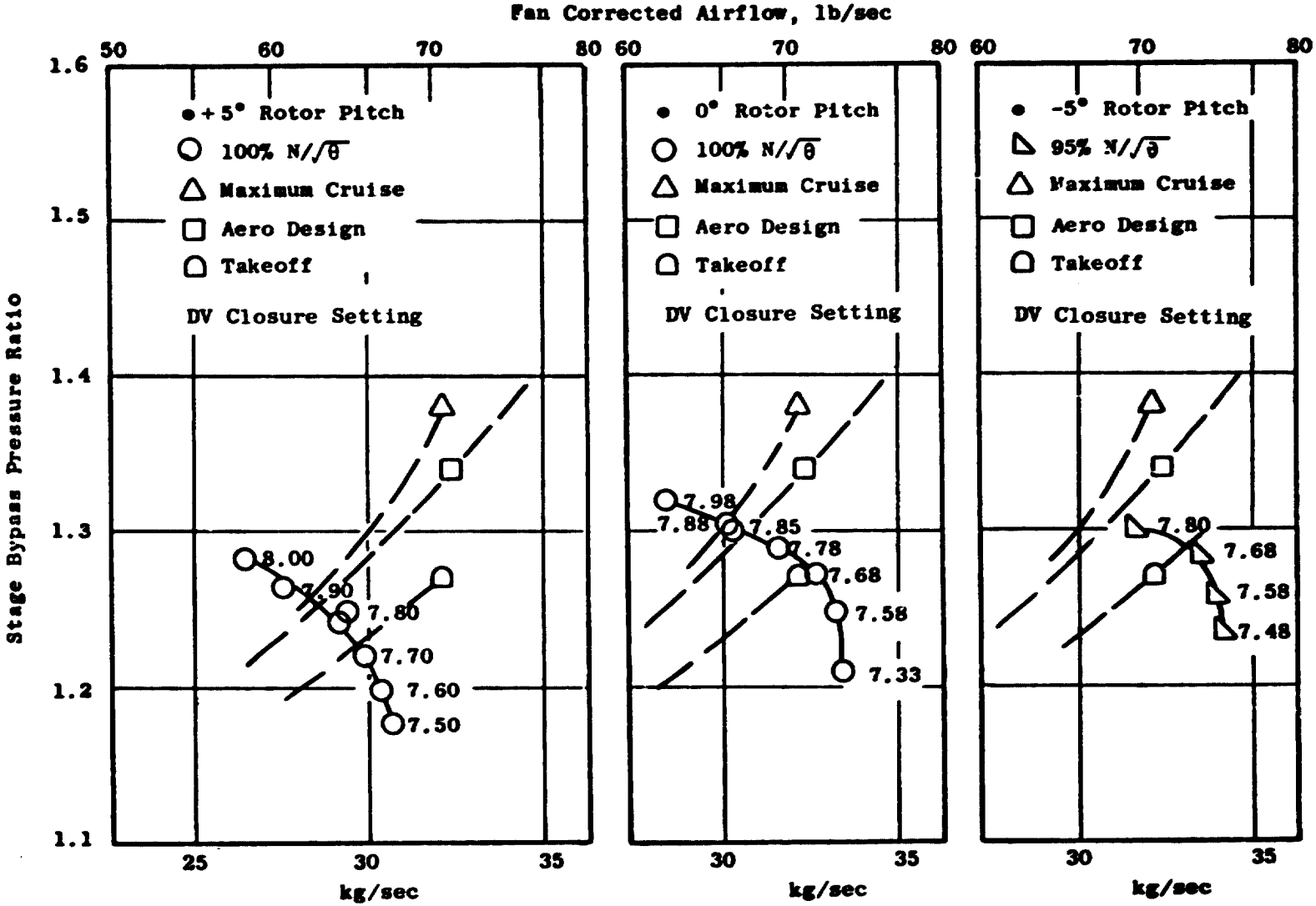

Figure 6. Location of Discharge Valve Closure Settings on Fan Map.

4.5 PERFORMANCE CALCULATION PROCEDURE

Data reduction procedures were specified for 7 separate data modes, as described in Appendix A. These modes were characterized by the vehicle configuration (forward mode, reverse mode, or acoustic test) and the type of instrumentation installed (fixed rakes, traversing rakes, or probes). Real gas effects and humidity corrections were introduced through variations in γ, R, and C_p. Pressures and temperatures sensed by the rakes were arithmetically-averaged circumferentially and mass-averaged radially to obtain overall discharge conditions. All data were grouped and displayed in the following categories: Inlet, Bypass OGV Exit, and Core Duct. Flow was calculated at each of these regions by using assumed-area coefficients and the averaged values of pressure and temperature sensed by the rakes and probes, along with local static pressure averages. The total fan flow was determined from data obtained from the three inlet rakes at Station 44.23 and the casing static pressure taps at Station 36.0. An orifice located in the core suction system was used to accurately measure physical core flow and provided a consistency check on the other calculated flows.

4.6 PRESENTATION OF OVERALL FAN PERFORMANCE

Basic aerodynamic design of the UTW fan incorporates radial variations in discharge total pressure and total temperature. Additionally, off-design fan operating conditions will produce differing radial variations. Accurate UTW engine cycle representation of the fan component requires recognition of these variations to accurately match fan and core engine operating points. Accordingly, overall fan forward-thrust aerodynamic performance is presented in the form of two maps to distinguish the performance characteristics in the fan-bypass and fan-core regions. One map presents fan bypass total-pressure ratio and efficiency versus total fan flow. The second map presents fan hub total-pressure ratio and efficiency, which are also plotted, versus total fan flow. In essence, this method of presentation for UTW engine operation assumes that the fraction of the total flow that passes under the island depends only upon the combined equivalent discharge valve closure setting and is independent of the individual discharge valve closure settings. The axial gap between the island trailing edge and the splitter leading edge does tend to decouple the fan from the independent throttling of the bypass and core streams by virtue of the radial streamline shift that occurs within the axial gap in forward mode operation, thereby, justifying the above assumptions.

SECTION 5.0

FORWARD MODE PERFORMANCE (CLEAN INLET)

Forward mode performance was obtained with simulated core flow with a scale model of the engine inlet bellmouth installed. This is the vehicle configuration and instrumentation layout shown in Figure 44. The overall fan performance is presented at each rotor pitch angle setting with two maps to distinguish the performance characteristics of the fan bypass and fan core regions. Figures 7 through 9 present fan bypass measured test data that have been adjusted by the methods described in Appendix B. The forward mode aerodynamic data listing is presented in Table I. Additional forward mode aero data were taken with an accelerating (high Mach) inlet installed and is discussed in Section 5.8.

5.1 FAN BYPASS REGION

A fixed-area operating line through the aero design point is shown as a dashed line on the fan bypass maps in Figures 7 through 9. At design speed and nominal blade angle, the measured flow of 30.6 kg/sec (67.5 lbm/sec) and bypass pressure ratio of 1.30 were, respectively, 5.5% and 3.0% less than the design values of 32.4 kg/sec (71.4 lbm/sec) and pressure ratio of 1.34. The major reason for the deficiency was that the pressure ratio at which the flow began to diminish was lower than design intent, which indicated a rotor deviation angle larger than design intent. Several factors complicated the task of determining an overall stage efficiency, as explained in Appendix B, resulting in uncertainties in the calculated results. However, the estimated design speed adiabatic efficiency of 0.86 to 0.87 compared favorably with the required design point of 0.867.

Maximum flow at design speed exceeded design flow, indicating that the flow-passing capacity of the fan was not limited by the suction surface incidence angle or by throat area restrictions. Above design speed, flow increased less rapidly with speed along a given operating line than at lower-than-design speeds. This rate of increase of maximum flow with speed at greater-than-design speeds was significantly less than observed on most other fans. Peak efficiency occurred on an operating line slightly less throttled than design, and held relatively constant up to about 105% of design speed. A significant deterioration in peak efficiency was noted at 110% of design speed.

Fan performance at +5° (closed) and -5° (open) rotor pitch angles exhibited expected trends. Speed lines shifted to higher flow when the rotor pitch was opened from nominal, and shifted to lower flow as the rotor pitch was closed. Peak efficiency was slightly higher for the closed pitch angles at comparable speeds, but dropped significantly as the rotor pitch was opened. Peak efficiency occurred at or near 100% $N/\sqrt{\theta}$ for the +5° (closed) blade angle and dropped off less rapidly with overspeed than for the nominal blade angle.

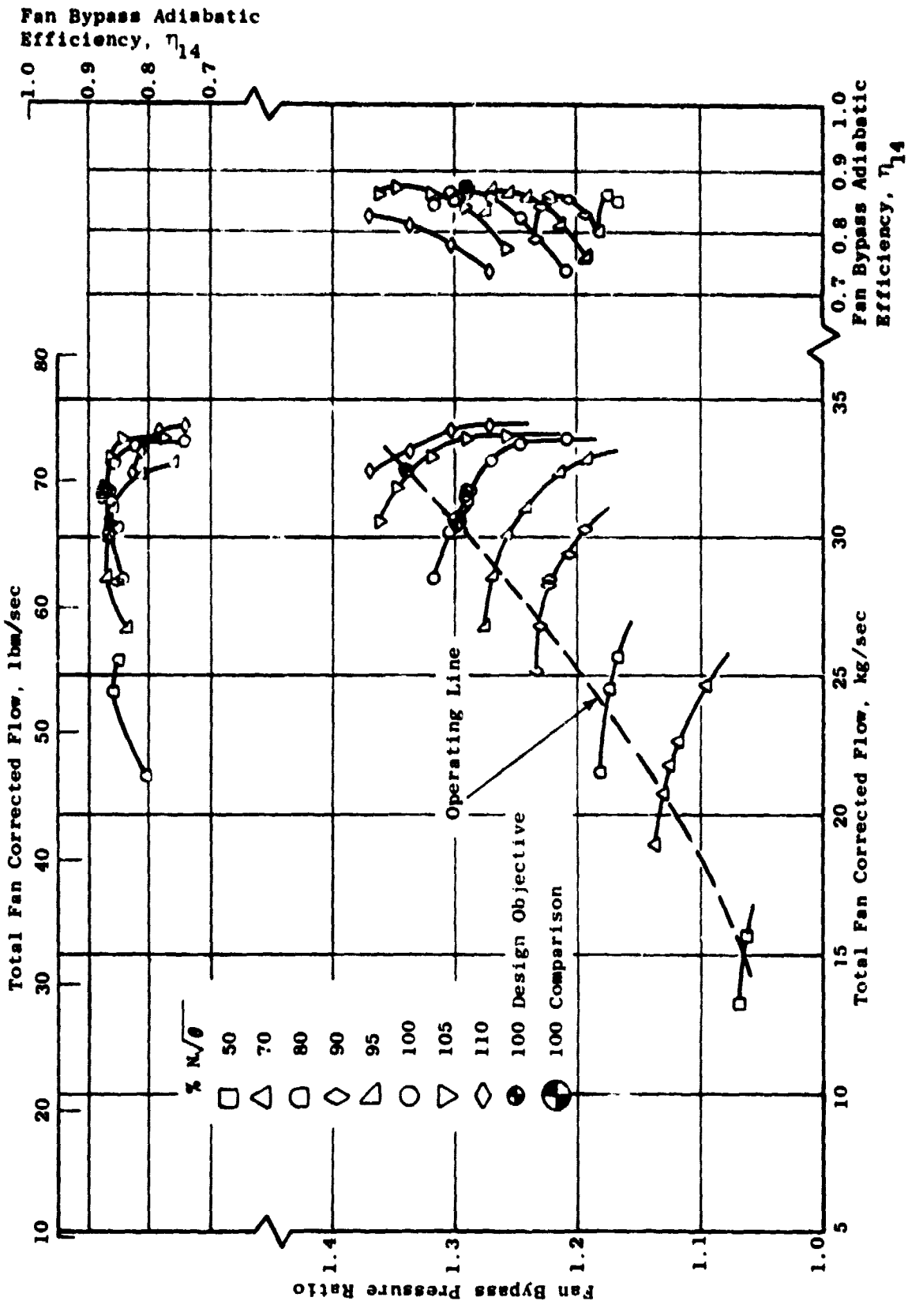

Figure 7. Fan Bypass Performance at Nominal Pitch Setting ($\beta_P = 0°$).

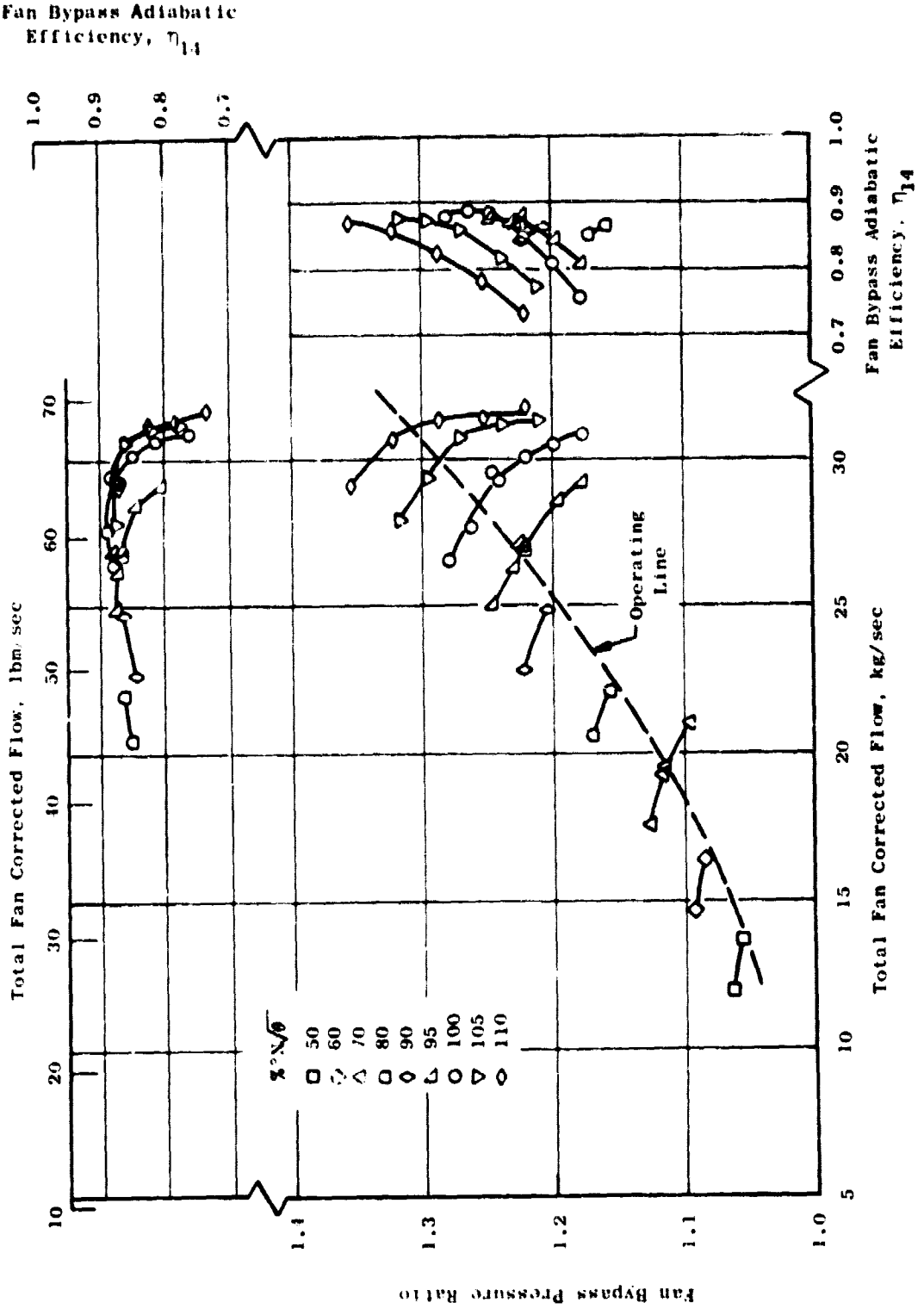

Figure 8. Fan Bypass Performance at +5° (Closed) Pitch Setting.

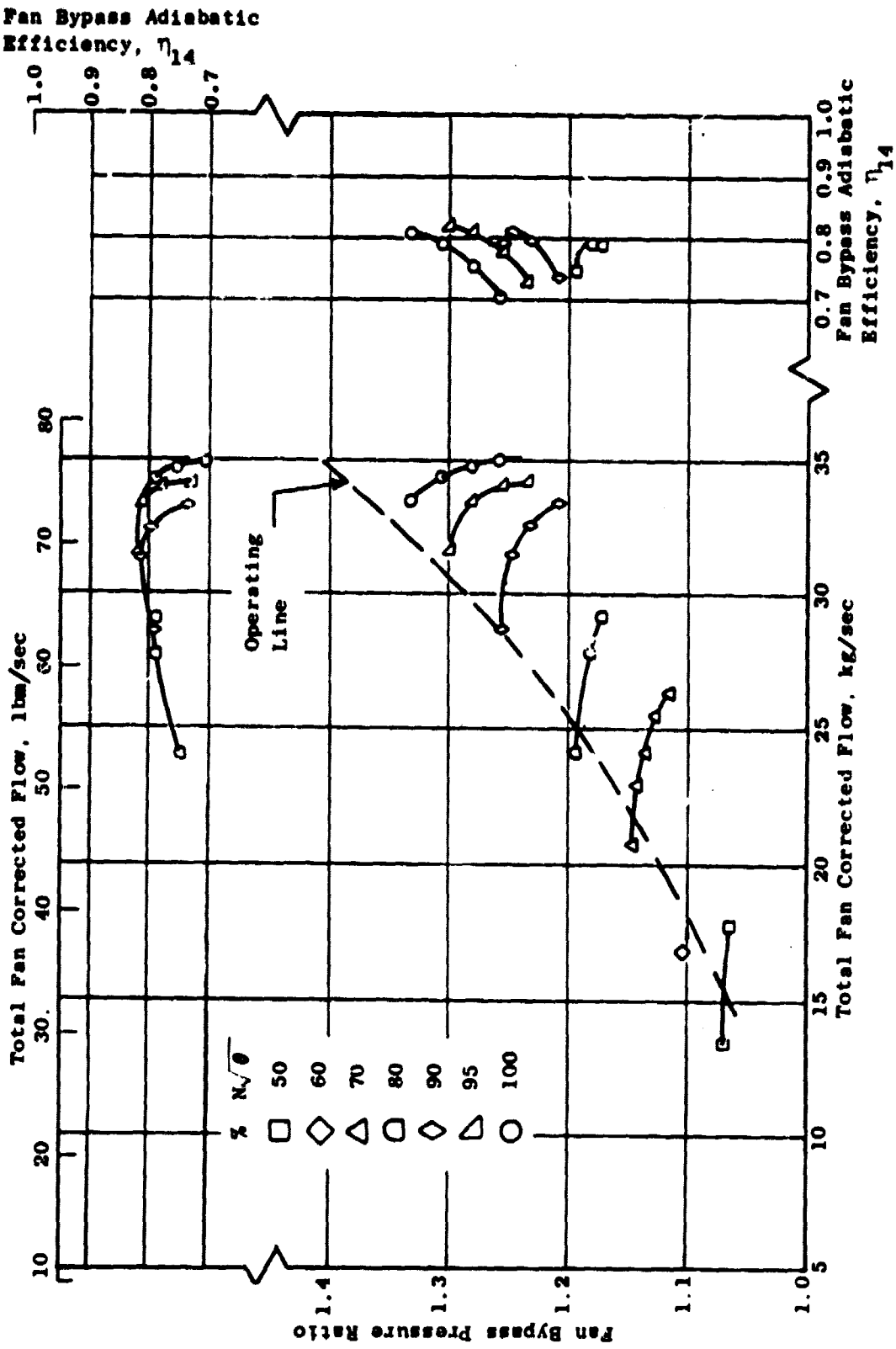

Figure 9. Fan Bypass Performance at -5° (Open) Pitch Setting.

Table 1. UTW Simulator Data Tabulation, Forward Mode, Inlet Bellmouth.

Run	Rdg	β	$\%N/\sqrt{\theta}$	DV Closure Setting	BPR	$W_1\sqrt{\theta_1}/\delta_1$ kg/sec	Stg P/P	Stg η
1	6	0°	80.0	7.73	12.9	25.52	1.1660	0.8508
1	7	0°	80.0	7.83	12.4	24.39	1.1736	0.8594
1	8	0°	90.0	7.78	12.0	28.32	1.2253	0.8535
1	9	0°	95.0	7.78	12.1	30.01	1.2565	0.8643
1	10	0°	100.0	7.78	12.1	31.63	1.2909	0.8657
1	12	0°	100.1	7.78	12.0	31.59	1.2903	0.8712
1	13	0°	100.1	7.58	13.5	33.27	1.2471	0.8265
1	14	0°	100.0	7.88	11.5	30.10	1.3042	0.8663
1	15	0°	100.1	7.68	12.9	32.68	1.2705	0.8596
1	16	0°	50.1	7.78	13.0	15.49	1.0624	0.8959
1	17	0°	50.1	8.08	10.5	12.98	1.0685	0.8285
1	18	0°	70.1	8.03	11.1	18.73	1.1370	0.8151
1	19	0°	80.0	8.03	10.8	21.33	1.1816	0.8053
1	21	0°	100.0	7.78	12.2	31.42	1.2913	0.8773
1	22	0°	100.0	7.98	10.8	28.40	1.3180	0.8466
1	23	0°	95.0	7.98	10.8	26.65	1.2754	0.8368
1	24	0°	95.0	7.88	11.8	28.46	1.2693	0.8711
1	25	0°	95.1	7.68	12.5	30.97	1.2419	0.8602
1	26	0°	95.0	7.53	13.3	32.24	1.2148	0.8155
1	27	0°	95.0	7.33	13.7	32.60	1.1932	0.7609
1	28	0°	95.0	6.93	13.9	32.66	1.1934	0.7637
1	29	0°	95.0	7.78	11.8	29.87	1.2563	0.8684
1	30	0°	100.0	7.78	12.2	31.57	1.2890	0.8777
1	31	0°	100.2	7.33	13.5	33.42	1.2105	0.7413
1	32	0°	105.1	7.78	12.3	32.84	1.3186	0.8645
1	33	0°	105.0	7.88	11.6	31.76	1.3470	0.8764
1	34	0°	105.1	7.96	11.0	30.48	1.3617	0.8637
1	35	0°	105.0	7.68	12.6	33.47	1.2907	0.8446

Table 1. UTW Simulator Data Tabulation, Forward Mode, Inlet Bellmouth (Continued).

Run	Rdg	β	$\%N/\sqrt{\theta}$	DV Closure Setting	BPR	$W_1\sqrt{\theta_1}/\delta_1$ kg/sec	Stg P/P	Stg η
7	1	0°	100.1	7.85	11.3	30.30	1.2997	0.8525
7	2	0°	100.1	7.78	12.4	31.25	1.2886	0.8638
7	3	0°	105.0	7.58	12.8	33.52	1.2582	0.7749
7	4	0°	110.2	7.58	12.9	33.92	1.2720	0.7399
7	5	0°	110.1	7.68	12.5	33.76	1.3032	0.7843
7	6	0°	110.0	7.78	12.0	33.04	1.3368	0.8164
7	7	0°	110.0	7.88	11.0	32.30	1.3685	0.8305
7	8	0°	90.0	7.58	13.3	30.16	1.1934	0.8295
7	9	0°	90.0	7.68	12.6	29.23	1.2073	0.8536
7	10	0°	90.0	7.88	11.2	26.67	1.2310	0.8431
7	11	0°	90.0	7.98	10.5	25.04	1.2342	0.7944
7	12	0°	90.1	7.78	13.2	28.16	1.2226	0.8600
7	13	0°	90.0	7.78	9.0	28.55	1.2176	0.8660
7	14	0°	89.9	7.78	7.8	28.78	1.2135	0.8644
7	15	0°	90.0	7.78	15.8	27.24	1.2214	0.8558
7	16	0°	90.0	7.78	25.0	26.75	1.2220	0.8454
7	17	0°	70.1	7.88	11.6	20.55	1.1297	0.8393
7	18	0°	70.1	7.78	12.2	21.57	1.1249	0.8565
7	19	0°	70.1	7.68	12.8	22.46	1.1177	0.8467
7	20	0°	70.0	7.33	14.7	24.50	1.0958	0.7976
8	1	-5°	50.1	7.68	13.2	17.59	1.0664	0.7642
8	2	-5°	50.1	8.05	9.7	13.24	1.0696	0.6943
8	3	-5°	60.0	8.03	8.9	16.67	1.1034	0.7104
8	4	-5°	70.0	7.68	12.0	24.04	1.1355	0.7853
8	5	-5°	70.0	7.98	10.1	20.61	1.1452	0.7326
8	6	-5°	80.0	7.68	12.1	27.78	1.1805	0.7925
8	7	-5°	80.1	7.91	10.2	24.04	1.1929	0.7490
8	8	-5°	90.0	7.68	12.6	31.42	1.2472	0.8156

Table 1. UTW Simulator Data Tabulation, Forward Mode, Inlet Bellmouth (Continued).

Run	Rdg	δ	$\%N/\sqrt{\theta}$	DV Closure Setting	BPR	$W_1\sqrt{\theta_1}/\delta_1$ kg/sec	Stg P/P	Stg η
8	9	-5°	90.1	7.83	11.2	28.65	1.2554	0.7953
8	10	-5°	95.0	7.68	11.9	33.42	1.2815	0.8165
8	11	-5°	95.0	7.80	11.3	31.62	1.2987	0.8215
8	12	-5°	100.0	7.68	11.9	34.31	1.3068	0.7935
8	13	-5°	100.0	7.78	11.6	33.48	1.3321	0.8107
8	14	-5°	100.1	7.58	12.2	34.71	1.2809	0.7570
8	15	-5°	100.0	7.48	12.3	34.93	1.2583	0.7070
8	16	-5°	95.0	7.58	12.5	33.97	1.2559	0.7810
8	17	-5°	95.1	7.48	12.5	34.12	1.2346	0.7310
8	18	-5°	90.0	7.58	12.7	32.54	1.2316	0.7997
8	19	-5°	90.0	7.38	12.9	33.39	1.2083	0.7391
8	20	-5°	80.0	7.58	12.7	29.12	1.1721	0.7895
8	21	-5°	70.1	7.58	13.2	25.45	1.1273	0.7903
8	22	-5°	70.1	7.38	13.3	26.26	1.1152	0.7540
8	23	-5°	70.1	7.78	11.5	22.83	1.1417	0.8021
10A	1	+5°	49.9	7.90	11.9	13.49	1.0564	0.8528
10A	2	+5°	49.9	8.10	10.7	11.73	1.0630	0.8357
10A	3	+5°	60.0	7.90	12.6	16.19	1.0840	0.8695
10A	4	+5°	60.0	8.10	11.1	14.48	1.0929	0.8373
10A	5	+5°	70.0	7.90	12.3	19.08	1.1170	0.8663
10A	6	+5°	70.0	8.05	11.3	17.40	1.1269	0.8550
10A	7	+5°	80.0	7.90	11.8	21.95	1.1567	0.8655
10A	8	+5°	80.0	8.05	10.9	20.41	1.1700	0.8532
10A	9	+5°	90.0	7.90	12.1	24.71	1.2055	0.8656
10A	10	+5°	90.0	8.05	11.1	22.70	1.2229	0.8461
10A	11	+5°	95.0	7.85	12.1	26.95	1.2270	0.8690

Table I. UTW Simulator Data Tabulation, Forward Mode, Inlet Bellmouth (Concluded).

Run	Rdg	β	$\%N/\sqrt{\theta}$	DV Closure Setting	BPR	$W_1\sqrt{\theta_1}/\delta_1$ kg/sec	Stg P/P	Stg η
10B	1	+5°	50.1	7.90	12.1	13.39	1.0567	0.8809
10B	2	+5°	95.0	7.85	12.4	26.88	1.2230	0.8834
10B	3	+5°	95.0	8.00	11.3	24.92	1.2470	0.8788
10B	4	+5°	100.0	7.80	12.9	29.47	1.2477	0.8846
10B	5	+5°	99.9	8.00	11.2	26.45	1.2810	0.8802
10B	6	+5°	100.0	7.90	11.9	27.57	1.2634	0.8903
10B	7	+5°	105.0	7.80	12.5	30.61	1.2704	0.8618
10B	8	+5°	105.0	8.00	10.8	27.81	1.3171	0.8789
10B	9	+5°	105.0	7.90	11.5	29.27	1.2946	0.8765
10B	10	+5°	105.0	7.70	13.0	31.08	1.2383	0.8195
10B	11	+5°	105.0	7.60	13.6	31.19	1.2113	0.7770
10B	12	+5°	110.0	7.80	12.2	31.22	1.2872	0.8274
10B	13	+5°	110.0	8.00	10.9	29.05	1.3548	0.8714
10B	14	+5°	110.0	7.90	11.7	30.57	1.3225	0.8614
10B	15	+5°	110.1	7.70	12.3	31.31	1.2530	0.7862
10B	16	+5°	110.1	7.60	13.3	31.64	1.2216	0.7351
10B	17	+5°	100.0	7.80	12.8	29.15	1.2414	0.8713
10B	18	+5°	100.1	7.70	13.2	29.91	1.2211	0.8488
10B	19	+5°	100.0	7.60	13.7	30.36	1.1986	0.8105
10B	20	+5°	100.0	7.50	14.0	30.68	1.1773	0.7588
10B	21	+5°	95.0	7.85	12.5	26.72	1.2217	0.8679
10B	22	+5°	95.0	7.90	12.3	26.16	1.2305	0.8726
10B	23	+5°	94.9	7.70	13.0	28.47	1.1966	0.8471
10B	24	+5°	95.0	7.60	13.3	29.08	1.1788	0.8096
10B	25	+5°	70.0	7.90	12.4	19.33	1.1152	0.8664
10B	26	+5°	70.0	7.65	13.7	20.84	1.0956	0.8192

For the -5° (open) pitch setting, peak efficiency occurred at about 95% speed and appeared to fall off more rapidly with speed increase than for the nominal pitch setting. Also, a deterioration in peak efficiency was noted at lower speeds.

To meet the UTW engine-required takeoff fan flow and bypass pressure ratio at 94.5% corrected speed, the rotor must be opened approximately 3° from nominal rather than the pretest estimate of 1° open. Increased speed at less open pitch setting, however, would also satisfy the takeoff thrust and flow requirements and would additionally improve efficiency because of the efficiency trend with pitch angle noted earlier. Therefore, from the fan performance standpoint, it would be desirable to match the required takeoff flow and pressure ratio with the most closed blade pitch setting possible. The potential detrimental impact of the resulting speed increase on the acoustic signature of fans, however, needs to be weighed carefully. Engine flow and pressure ratio requirements at maximum cruise conditions may be satisfied at about 108% speed, by opening the blade pitch approximately 1° from nominal rather than the predicted 2° closed setting. Fan speed at the maximum cruise condition is set by the maximum mechanical rpm available from the low-pressure turbine; for this reason a trade between a more closed pitch setting and higher fan speed is not available. It should be noted that maximum cruise flow and pressure ratio were not obtained experimentally and are extrapolated values.

Operating limits of the fan near stall were determined at the nominal forward pitch angle only, replacing the bellmouth inlet with the accelerating inlet configuration. These stall-line limits are shown in Figure 10. Since the blades were readjusted to the nominal pitch angle for stall testing, a separate fan bypass map is employed to avoid confusion between data scatter and ability to reset the same blade angle. Estimated tolerance on blade pitch angle setting was ±0.5°. At all speeds tested, except 95% speed, rotating stall was limiting. At 95% speed, first flex mode instability was limiting. A more complete description of the aeromechanical response is given in Appendix C. The objective nominal pitch stall line was met or exceeded at every speed, indicating sufficient stall margin for all engine operating conditions. Constant speed stall margins were estimated as 20% at takeoff and 15% at maximum cruise.

5.2 FAN HUB (CORE) REGION

Measured performance of the fan hub flow, Figures 11 through 13, was close to design-point objective. Comparison was made at design speed and nominal blade angle at a flow of 30.6 kg/sec (67.5 lbm/sec). This flow was significant because it was the measured flow along an operating line through the design point on the bypass portion map, as shown in Figure 7. Measured hub pressure ratio slightly exceeded the design point objective of 1.23. Core adiabatic efficiency of 0.84 was six points higher than the predicted value of 0.78. As with the bypass performance, speed lines shifted to higher flows and pressure ratios when the rotor blade was opened and shifted to lower flows and pressure ratios as the blade was closed. Efficiency increased along all speed lines for all pitch angles as the fan was throttled,

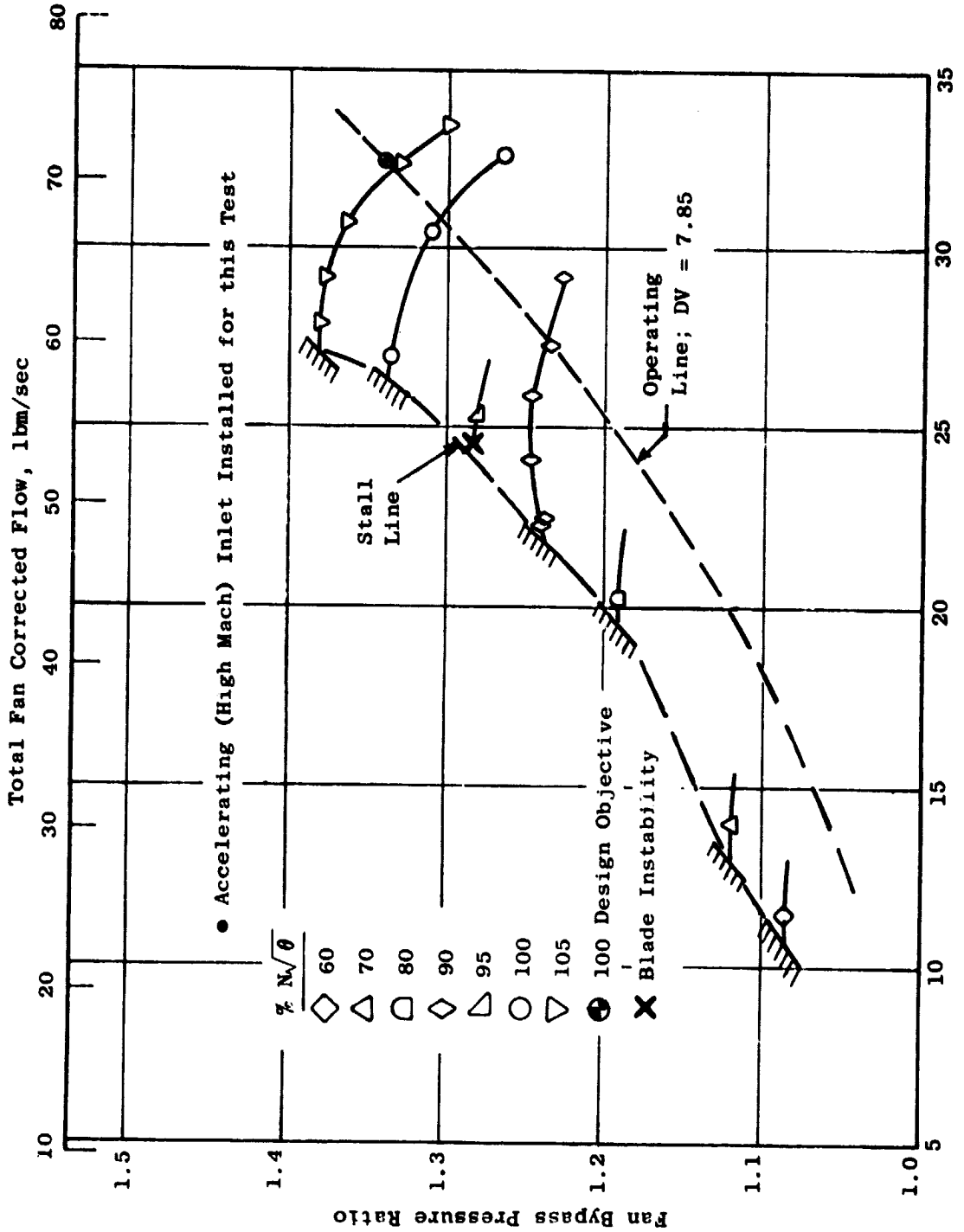

Figure 10. Fan Bypass Stall Line at Nominal Pitch Setting (β_F = 0°).

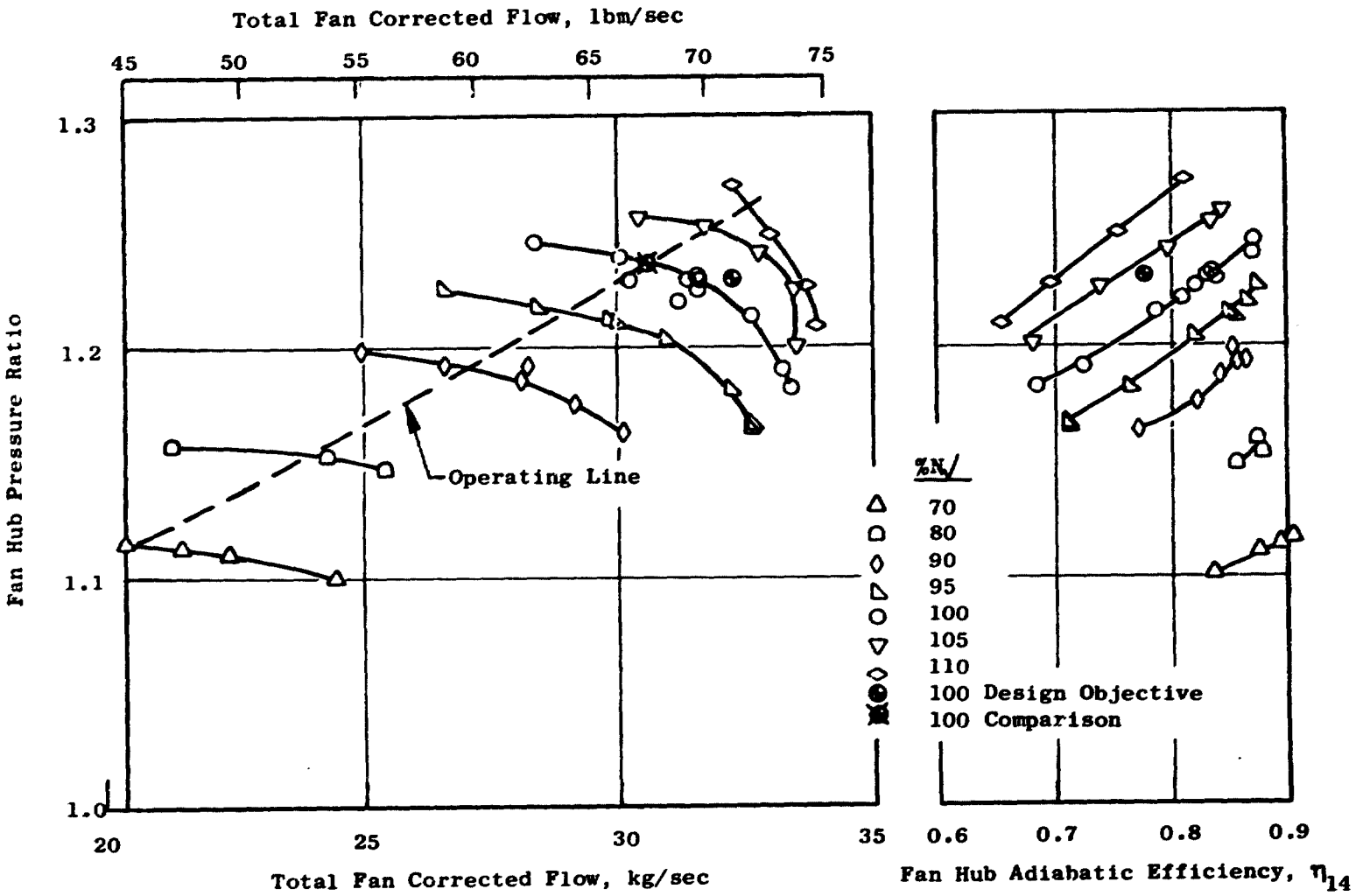

Figure 11. Fan Hub Performance at Nominal Pitch Setting (β_F = 0°).

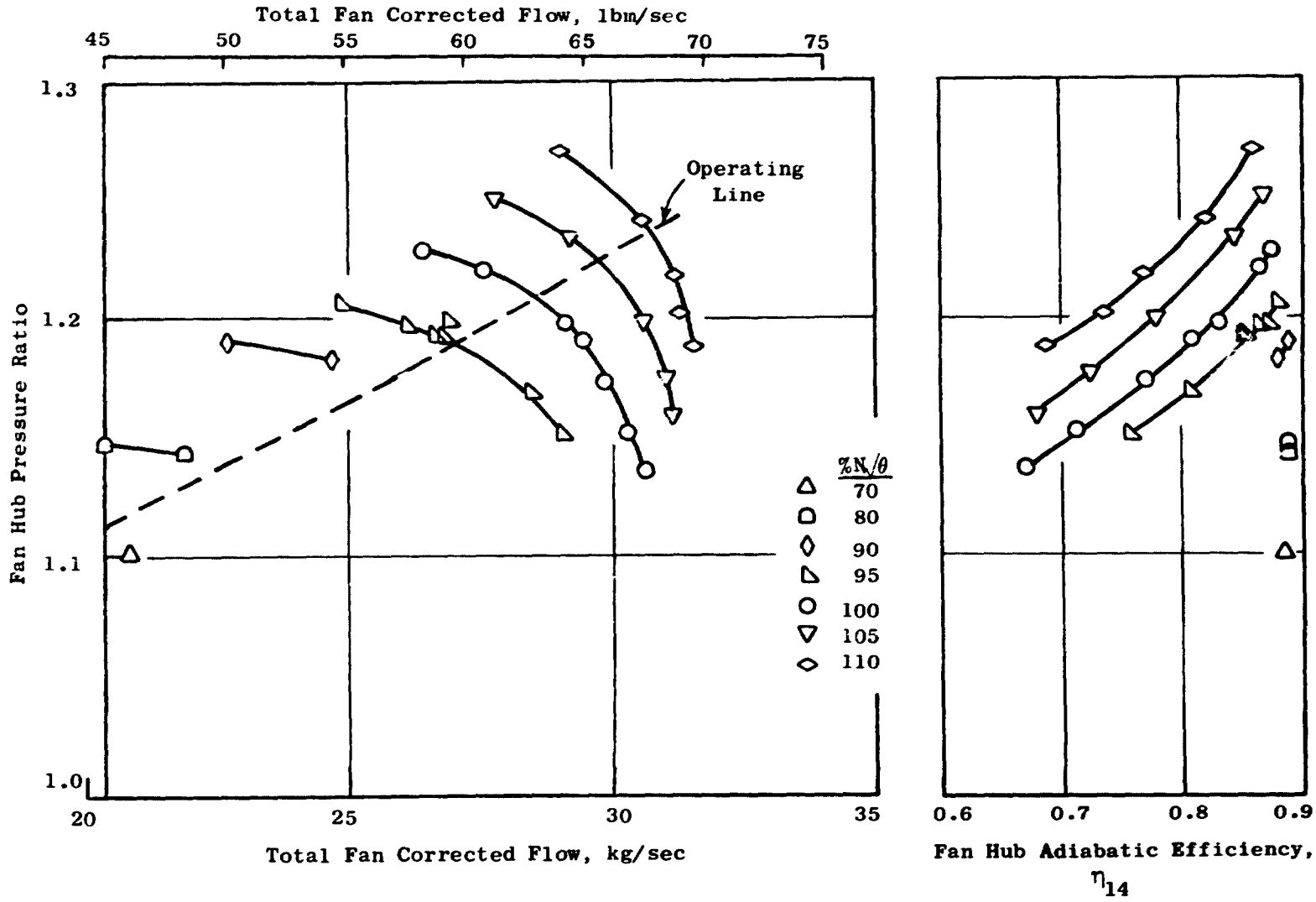

Figure 12. Fan Hub Performance at +5° (Closed) Pitch Setting.

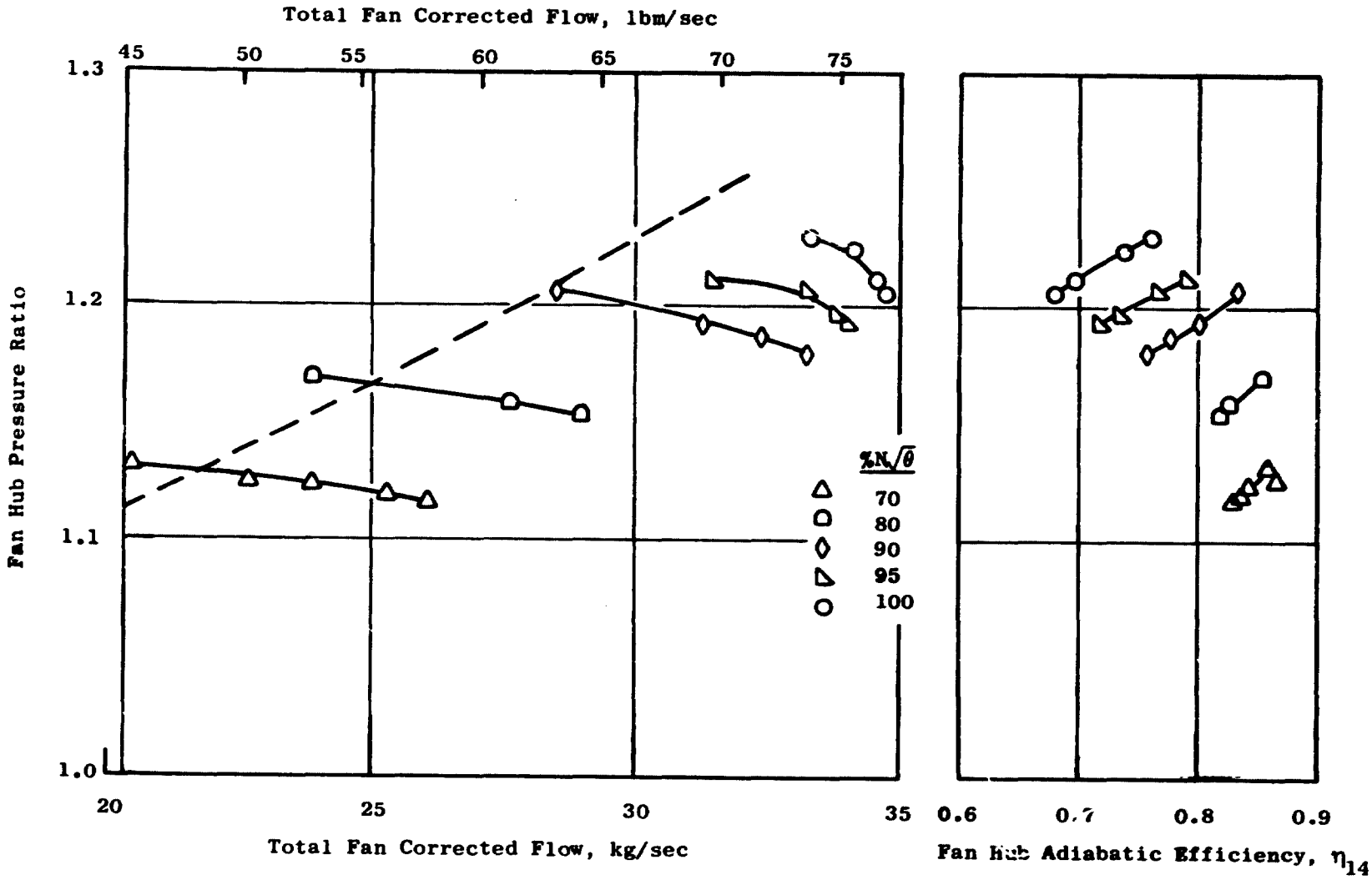

Figure 13. Fan Hub Performance at -5° (Open) Pitch Setting.

without reaching a peak over the range tested. Similar to the bypass region, fan hub (core) efficiency was slightly higher for the +5° (closed) pitch angle but dropped significantly at the -5° (open) blade pitch angle. Maximum fan hub efficiency achieved was 0.88, measured at 95% $N/\sqrt{\theta}$ for the most throttled bypass discharge valve closure setting at nominal pitch.

Engine-required fan hub pressure ratio, at takeoff conditions, was 1.20. The value achieved at takeoff fan flow for the nominal rotor pitch setting and 95% speed was 1.19. Since the rotor blade must be opened or oversped to achieve the bypass pressure ratio, the objective hub supercharging should be achieved. Maximum cruise engine-hub-required pressure ratio is 1.25. This requirement was slightly exceeded at maximum cruise fan flow and 100% speed for the nominal pitch setting. Since maximum cruise speed is 108%, the maximum cruise hub pressure ratio will probably be exceeded. Cycle redefinition will be required, however, to determine where the system will ultimately balance-out with the measured fan maps to determine the core supercharging available.

5.3 ROTOR EXIT RADIAL PROFILES

Radial profiles of rotor bypass pressure rise and efficiency were available from three sources:

- Fixed radial rake (Mode 1) data adjusted for discrepancies as discussed in Appendix B. [Based on 3 fixed radial ($5P_T$, T_T elements) rakes between vanes about 1/2 chord downstream of bypass OGV trailing edge.]

- Arc rake radial traverse data which assumed that the rotor exit pressure was an average of the three highest rake element pressures. [Based on radial traverse of four (13 P_T, T_T elements) arc rakes about 3/4 chord downstream of bypass OGV trailing edge.]

- Cobra radial traverse data (0° rotor pitch only) at several rotor outlet axial stations.

Primary observations from the nominal pitch ($\beta_F = 0°$) data presented in Figures 14 and 15 were:

- Rotor bypass discharge pressure profile was essentially flat for a relatively unthrottled (high flow) condition (Figure 14b, DV = 7.64); throttling the fan increased the tip pressure rise significantly more than in the hub portion. This observation is further illustrated in Figure 15, which shows throttling effects on both pressure and temperature rise profiles. The temperature rise in the hub portion of the bypass rotor flow remained essentially unchanged over the range of throttle conditions.

- Rotor efficiency profiles showed efficiencies greater than unity near the hub and efficiency dropoff in the tip regions. The

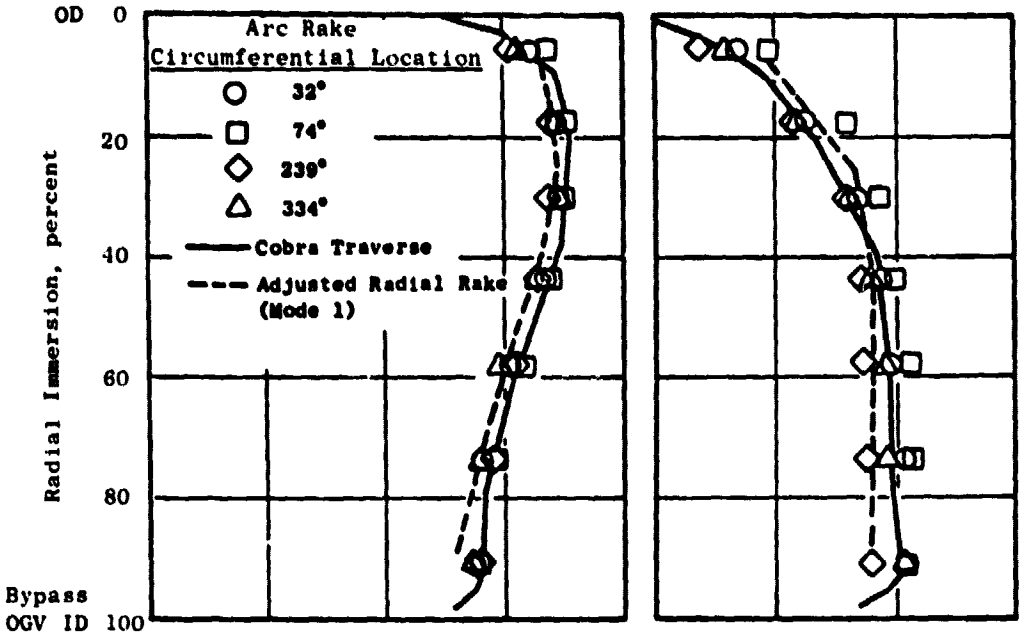

(a) Operating Line (DV = 7.84), $100\%N/\sqrt{\theta}$, W_F = 30.3 kg/sec (66.8 lbm/sec)

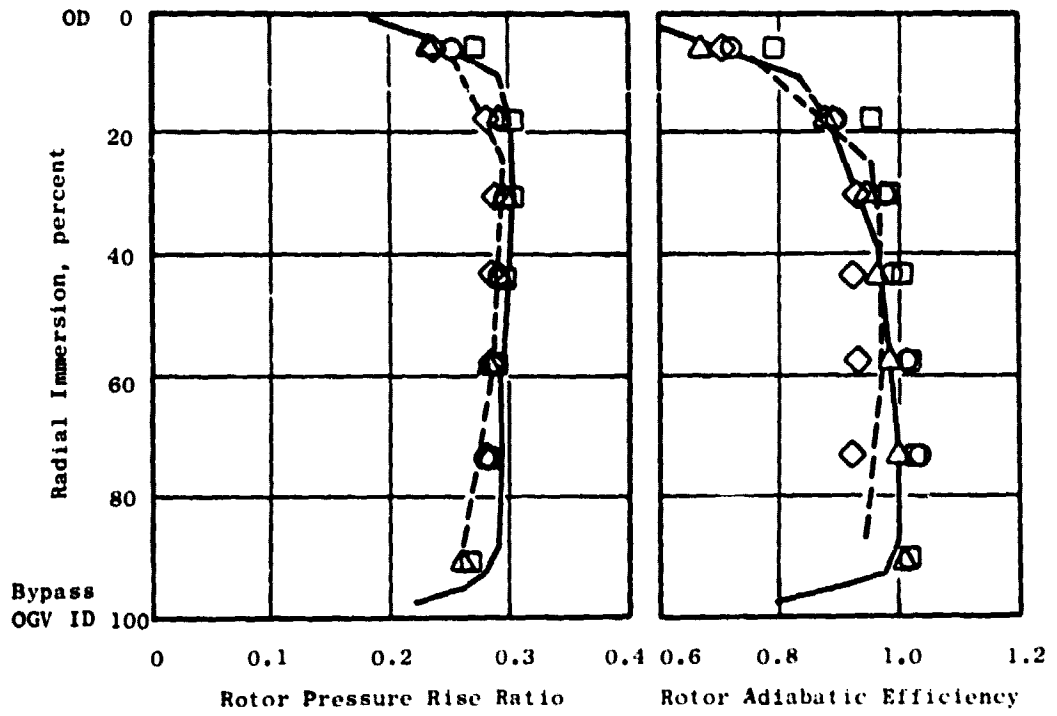

(b) Below Operating Line (DV = 7.64), $100\%N/\sqrt{\theta}$, W_F = 32.6 kg/sec (71.9 lbm/sec)

Figure 14. Rotor Bypass Pressure Rise Ratio and Efficiency Radial Profiles with Nominal (β_F = 0°) Blade Pitch at 100% Speed for Three Flows.

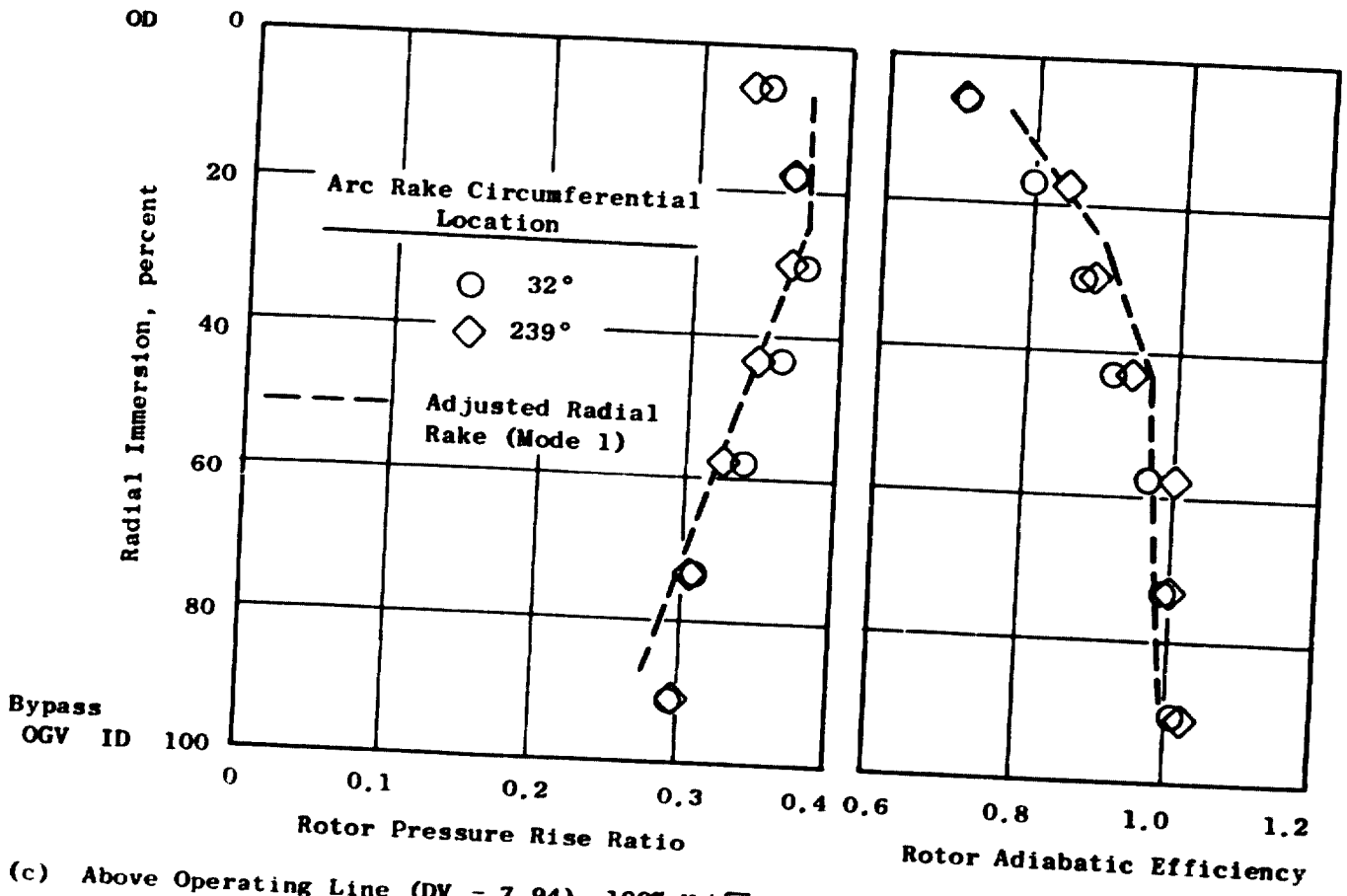

(c) Above Operating Line (DV = 7.94), 100% $N/\sqrt{\theta}$, W_F = 29.0 kg/sec (64.0 lbm/sec)

Figure 14. Rotor Bypass Pressure Rise Ratio and Efficiency Radial Profiles with Nominal (β_F = 0°) Blade Pitch at 100% Speed for Three Flows (Concluded).

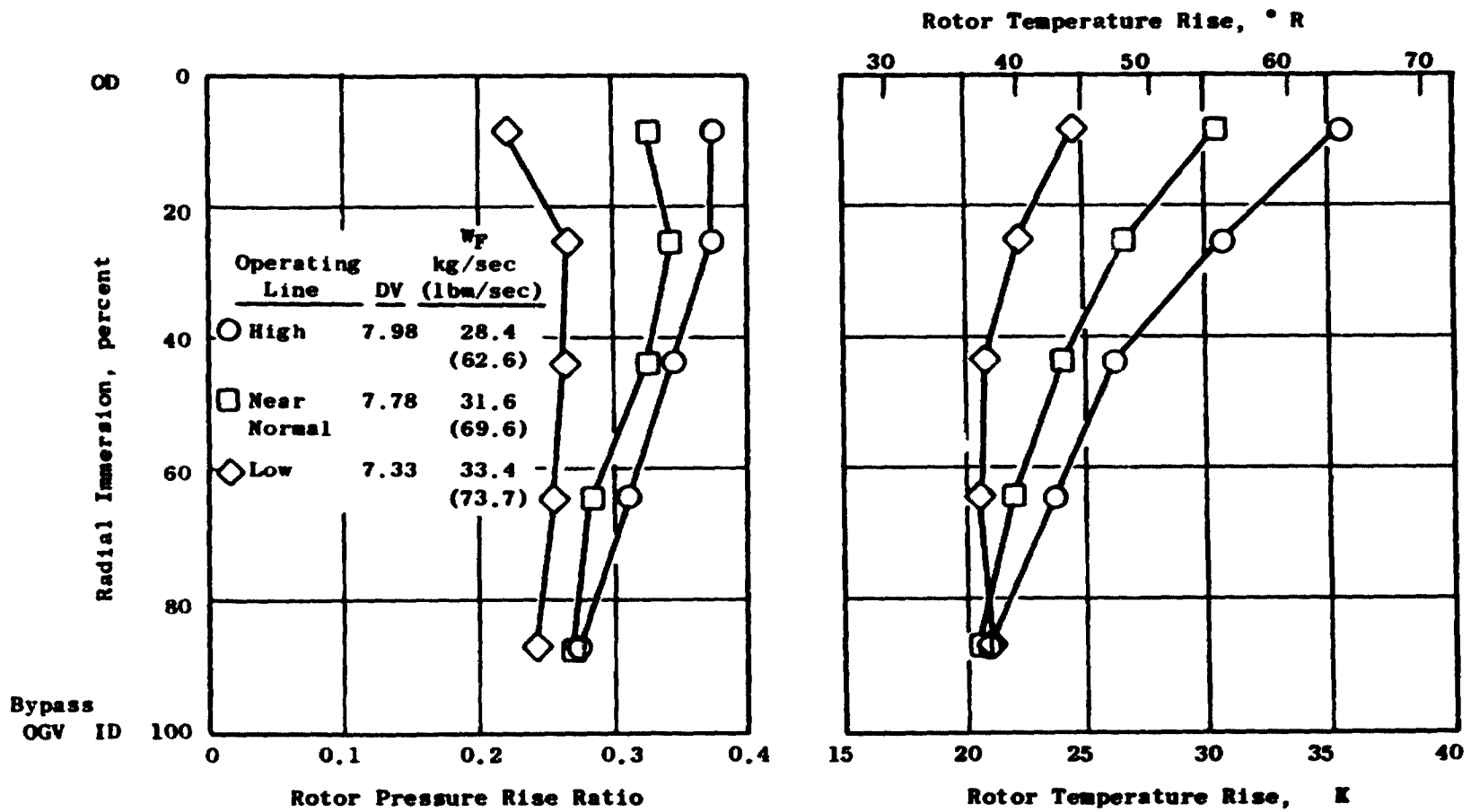

Figure 15. Effect of Throttling on Rotor Exit Pressure Rise Ratio and Temperature-Rise Radial Profiles for Nominal Pitch (β_P = 0°).

unreal hub efficiency level was in part due to the radial inlet temperature profile which was about 1° cooler (relative to the average inlet temperature) in the hub region and about 1° hotter in the tip region than fan face average. The net effect of the inlet temperature profile on a streamline basis would be to increase the calculated hub efficiencies about three points and decrease the calculated tip efficiencies about two points. The inlet temperature also varied circumferentially. (see Figure 53, Appendix B.)

- Efficiency profiles were free of the "holes" which are characteristic of trouble areas. The efficiency dropoff in the tip region is typical of most fans and the magnitude was not subject to large swings with changes in throttling.

- Fair agreement in rotor pressure rise was obtained from the three measurement sources. The cobra probe radial traverse data indicated a relatively higher pressure rise, probably because it was directly downstream of the rotor and was free of mixing and bypass OGV secondary flow effects.

Radial profiles for the +5° (closed) and -5° (open) rotor pitch setting, shown in Figures 16 and 17, respectively, display characteristics similar to those observed for the 0° rotor pitch.

5.4 SIMULATED CORE INLET RADIAL PROFILES

Ring average radial profiles of pressure rise, temperature rise, and efficiency, as measured by the rakes downstream of the transition duct at the simulated core inlet for 100% speed and nominal pitch (β_F = 0°) are plotted in Figure 18. One rake element at the outermost radial immersion was found to measure total pressure inaccurately, often reading as much as 10% higher or lower than the other rake elements at that radius. Its value was deleted from the ring or circumferential average. Radial profiles near the design point, at a discharge valve closure setting of 7.85, followed the same shape and nearly the same level as the assumed design profiles. As the fan was throttled along the design speed line, the radial profiles changed uniformly, showing no rapid breakdown of flow at the hub wall. Figure 19 shows the variation of the fan hub (simulated core inlet) efficiencies at three radial immersions over the range of discharge valve and blade pitch angle settings tested. In all cases the immersion efficiencies increased uniformly as the fan back pressure was increased showing very little deterioration in the radial profile. Furthermore, the reduction in overall core efficiency previously noted at the -5° (open) blade setting occurred more or less uniformly across the span.

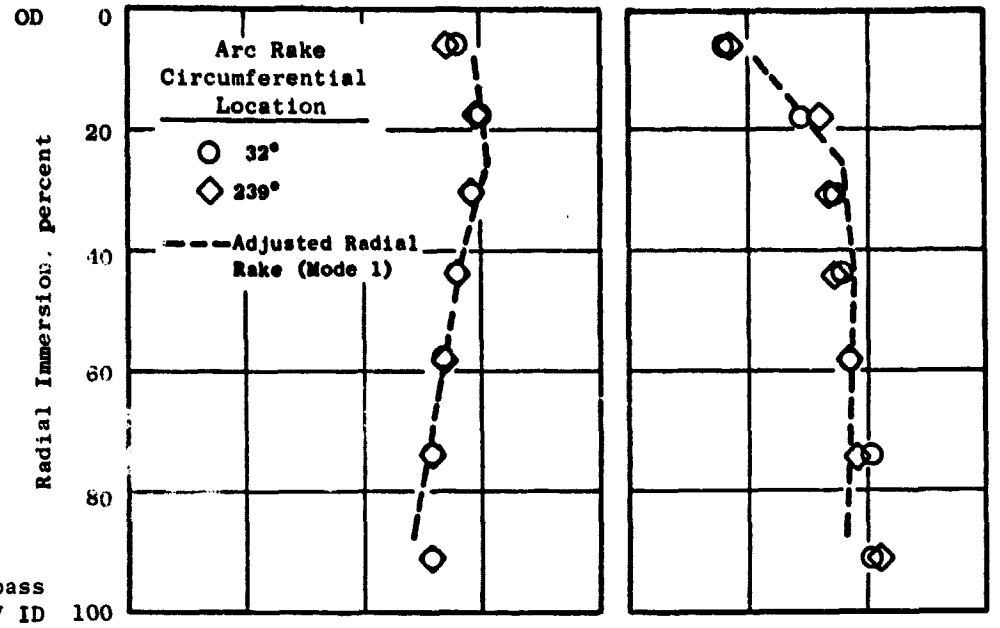

(a) Above Operating Line (DV = 7.90), 100% $N/\sqrt{\theta}$, W_F = 27.6 kg/sec (60.8 lbm/sec)

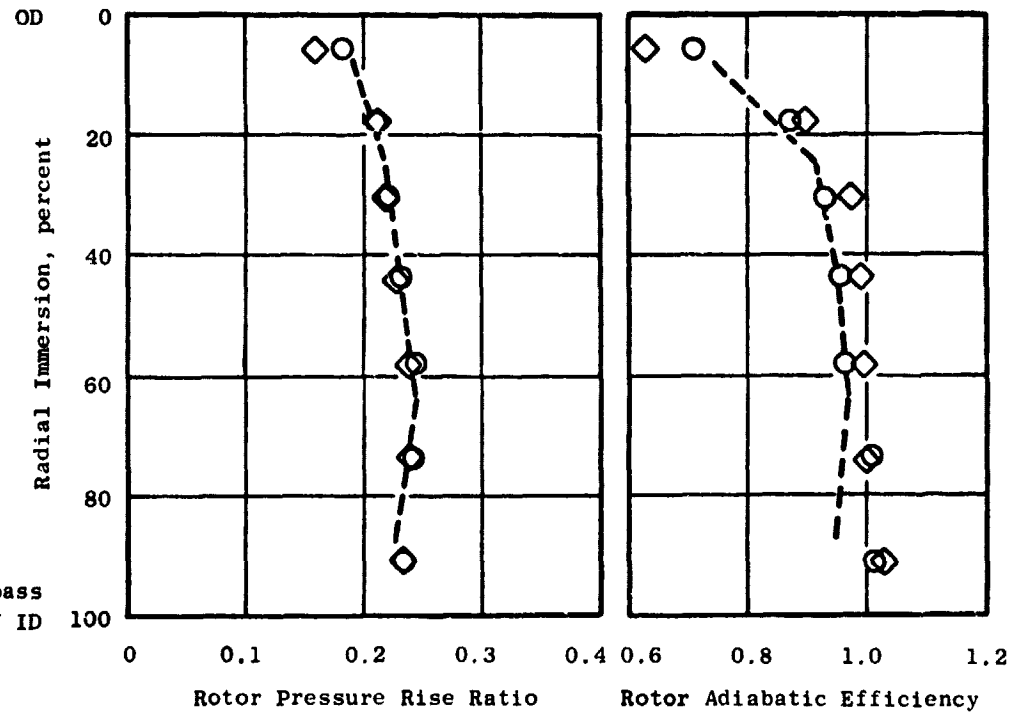

(b) Below Operating Line (DV = 7.60), 100% $N/\sqrt{\theta}$, W_F = 30.4 kg/sec (66.9 lbm/sec)

Figure 16. Rotor Bypass Pressure Rise Ratio and Efficiency Radial Profiles with +5° (Closed) Blade Pitch at 100% Speed for Two Flows.

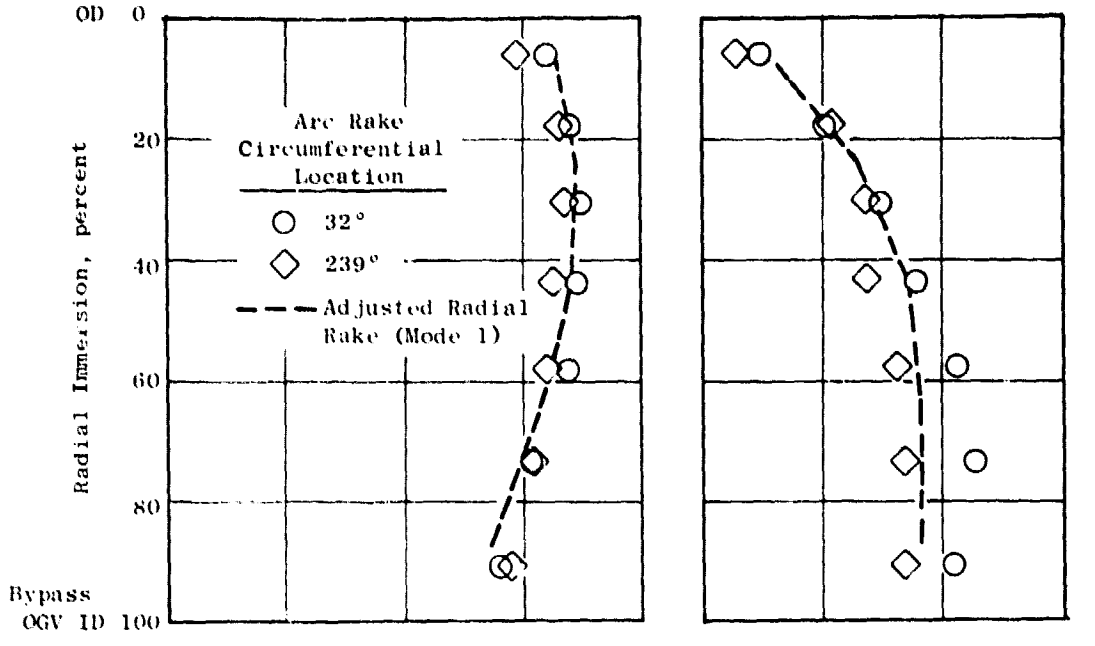

(a) Near Operating Line (DV = 7.79), 95% N, θ, W_p = 31.6 kg/sec (69.7 lbm/sec)

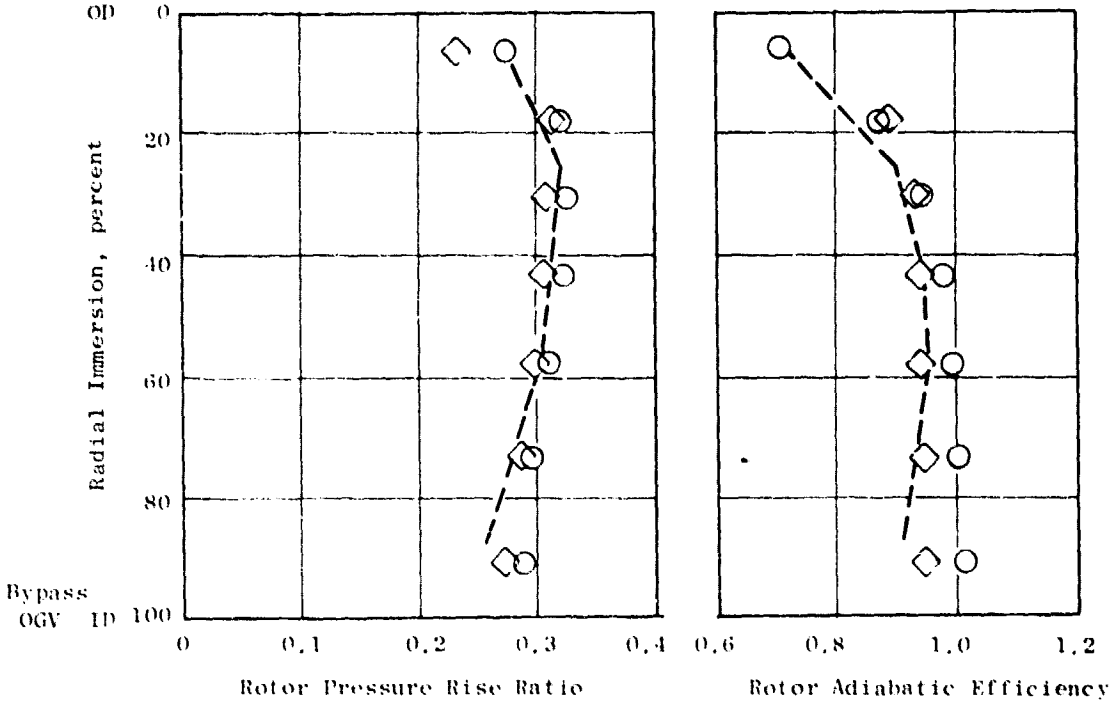

(b) Below Operating Line (DV = 7.58), 95% N, θ, W_p = 34.0 kg/sec (74.9 lbm/sec)

Figure 17. Rotor Bypass Pressure Rise Ratio and Efficiency Radial Profiles with -5° (Open) Blade Pitch at 95% Speed for Two Flows.

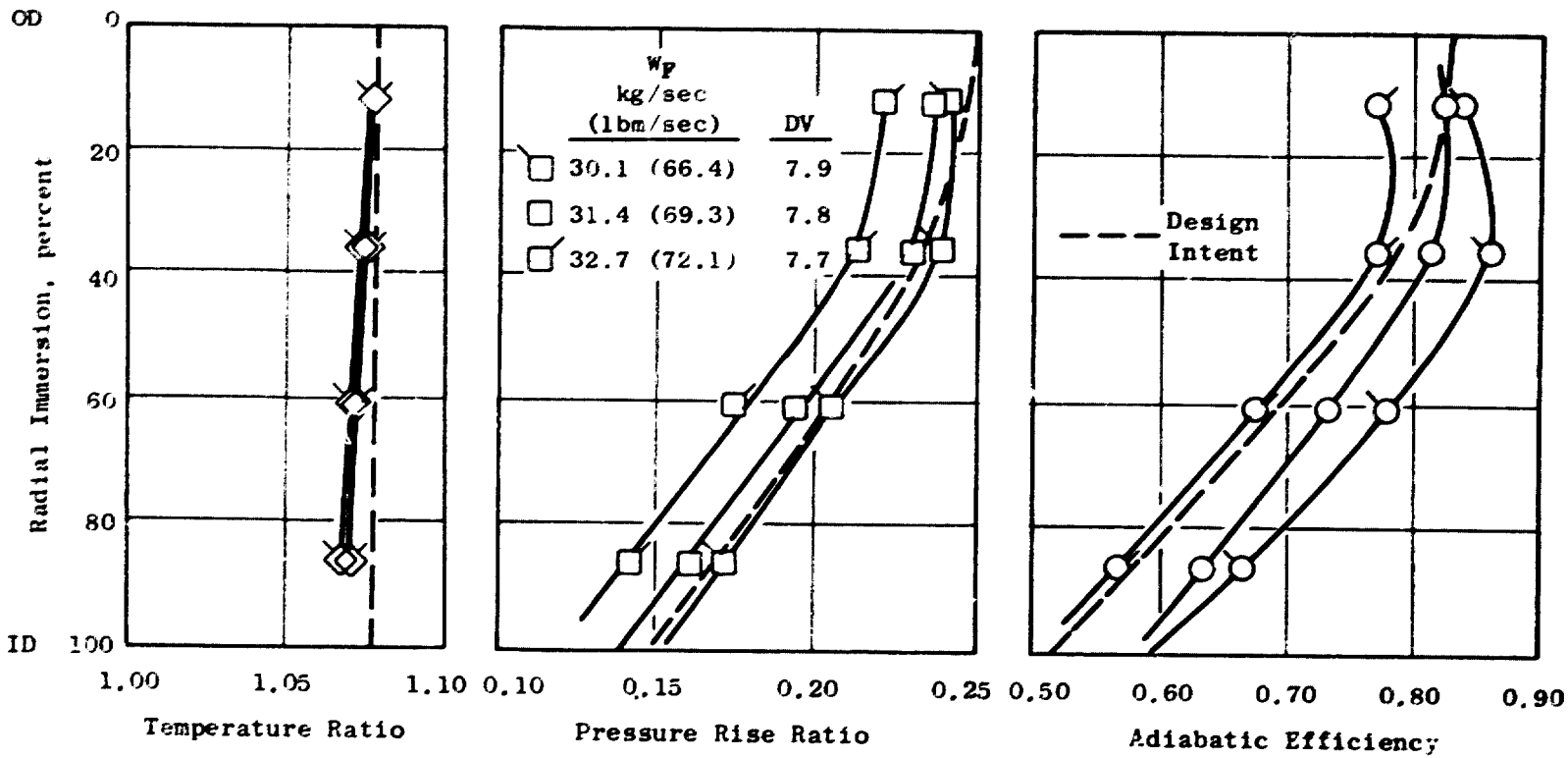

Figure 18. Fan Hub (Simulated Core Inlet) Radial Profiles with Nominal Blade Pitch (δ_P = 0°) at 100% Speed for Three Fan Flows.

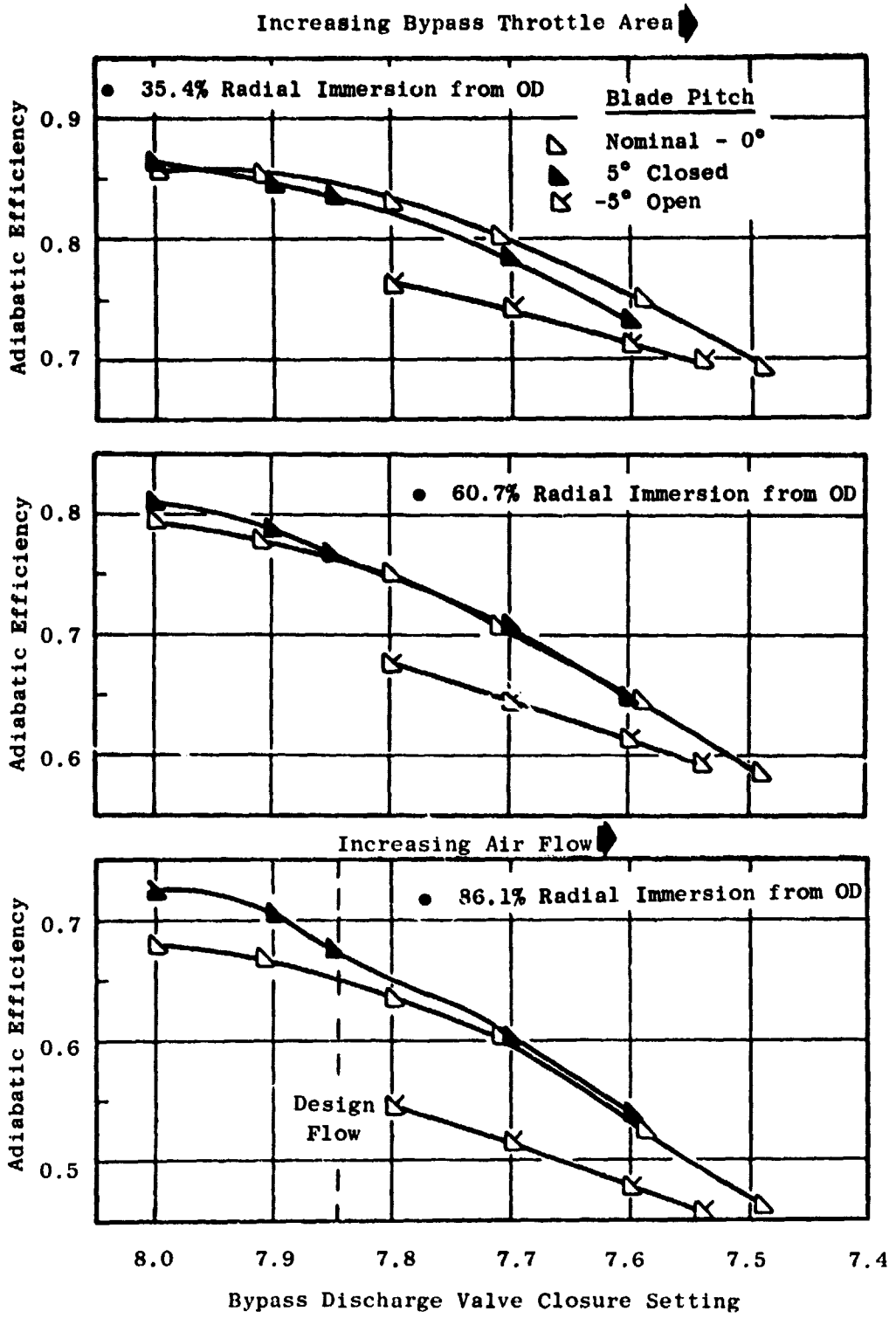

Figure 19. Fan Hub (Simulated Core Inlet) Efficiency Variations with Throttling at 100% Speed for 3 Radial Immersions with 3 Forward Blade Pitch Angles.

5.5 BYPASS OGV PERFORMANCE

Performance of the bypass OGV was assessed relative to both total pressure loss and induced circumferential flow distortion. The bypass OGV total pressure loss was determined from arc rake radial traverse data at each of seven immersions as follows:

$$\left(\frac{\Delta P_t}{P_t}\right)_{\substack{\text{Bypass}\\ \text{OGV}}} = \frac{(P_t)_{\text{Rotor Exit}} - (P_t)_{\text{Stage Exit}}}{(P_t)_{\text{Rotor Exit}}}$$

where

$(P_t)_{\text{Rotor Exit}}$ = average of three highest arc rake total pressures

$(P_t)_{\text{Stage Exit}}$ = average of arc rake total pressures which span an integral number of vane passages (see Table V of Appendix A)

Radial profiles of the bypass OGV total pressure loss are presented in Figure 20 for four different vane types. Arc rake measurements were made at four circumferential angle locations as illustrated in Figure 46 of Appendix A. Referring to Figure 46 of Appendix A, the different vane types are classified as open 2, open 1, nominal, closed 1, and closed 2 according to their respective design outlet flow angles of -10°, -5°, 0°, +5°, and +10°. Three of the circumferential locations, 32°, 239°, and 334° (standard angle convention is aft-looking-forward measured clockwise from top-dead-center), were located approximately in the midcircumferential position for a given vane type. The fourth location, 74°, was purposely located such that the elements on one side of the rake sensed the wake from an open 2-type vane, and the elements on the other side of the rake sensed the wake from an open 1-type vane. In general, measured loss levels were higher for the open 2 vanes and lower for the closed 2 vanes at the operating condition of Figure 20, a result consistent with the relatively higher loadings of the open vane sets. An examination of the vane passage circumferential pressure profiles in Figures 21 and 22 shows that:

- Open 2 vane (design outlet flow angle of -10°) wake is typically wider than the other vane wakes.
- Vane wakes at the 74° position, where an open 2 (design outlet flow angle of 10°) and open 1 (design outlet flow angle of -5°) vane form adjacent sides of the passage, are relatively shallow, possibly reflecting the relatively smaller effective area ratio of this passage.

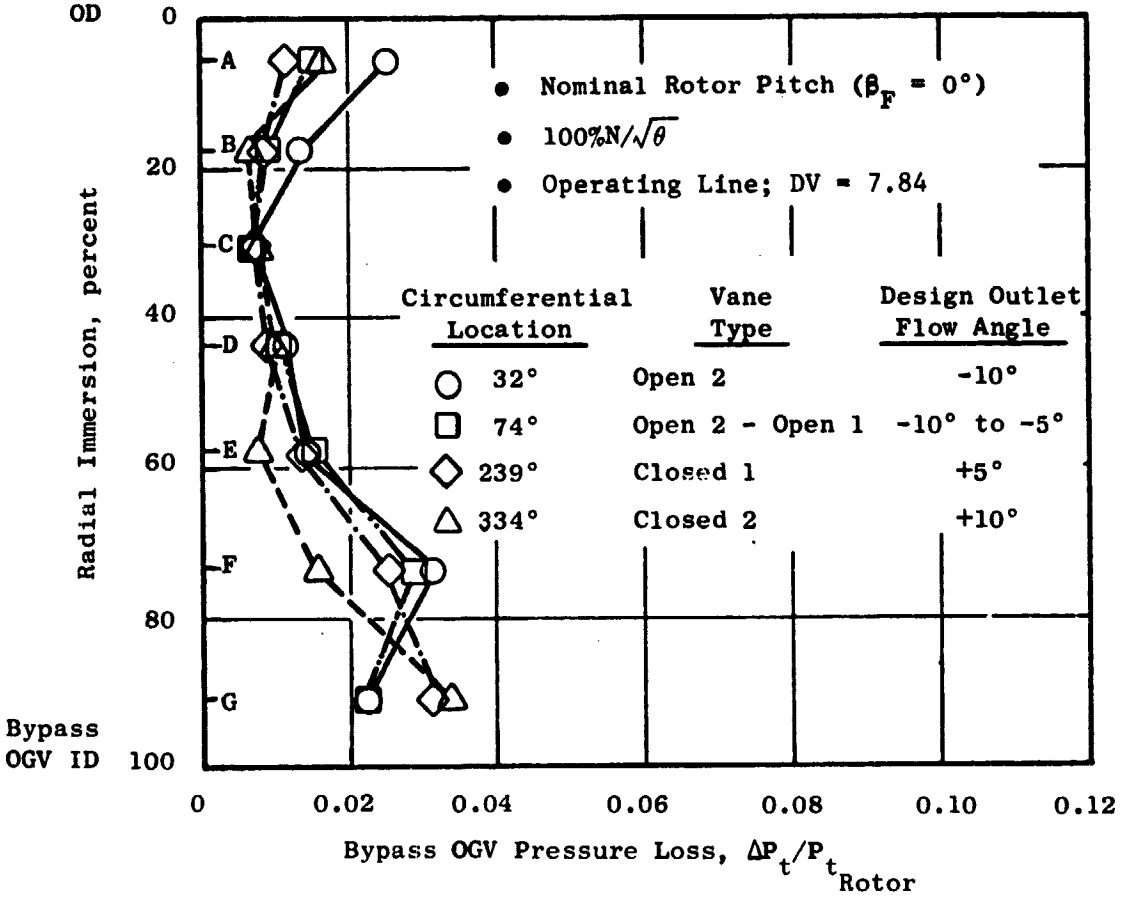

Figure 20. Bypass OGV Radial Loss Profiles at Various Circumferential Locations.

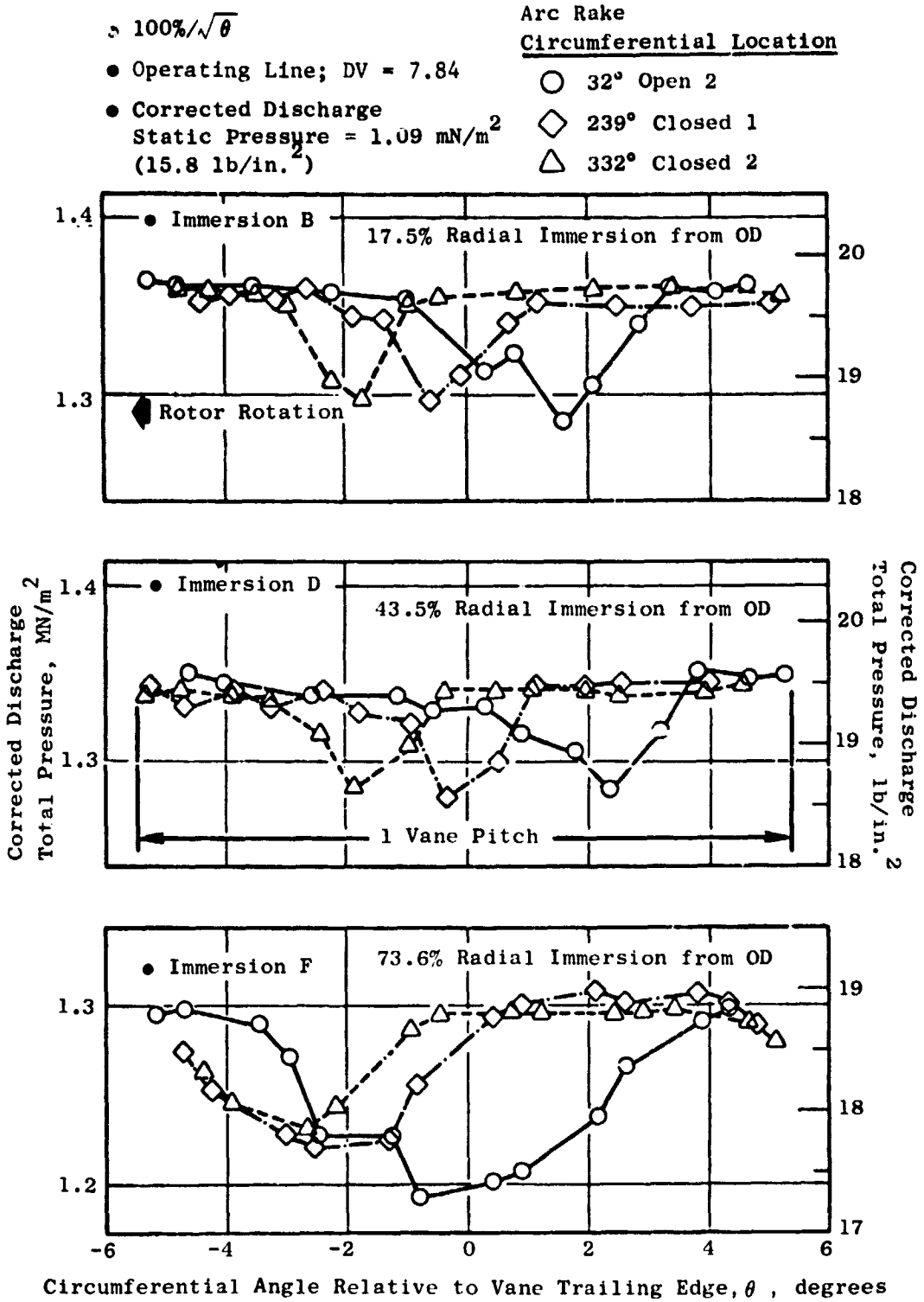

Figure 21. Circumferential Pressure Profiles for the Various Vane Types.

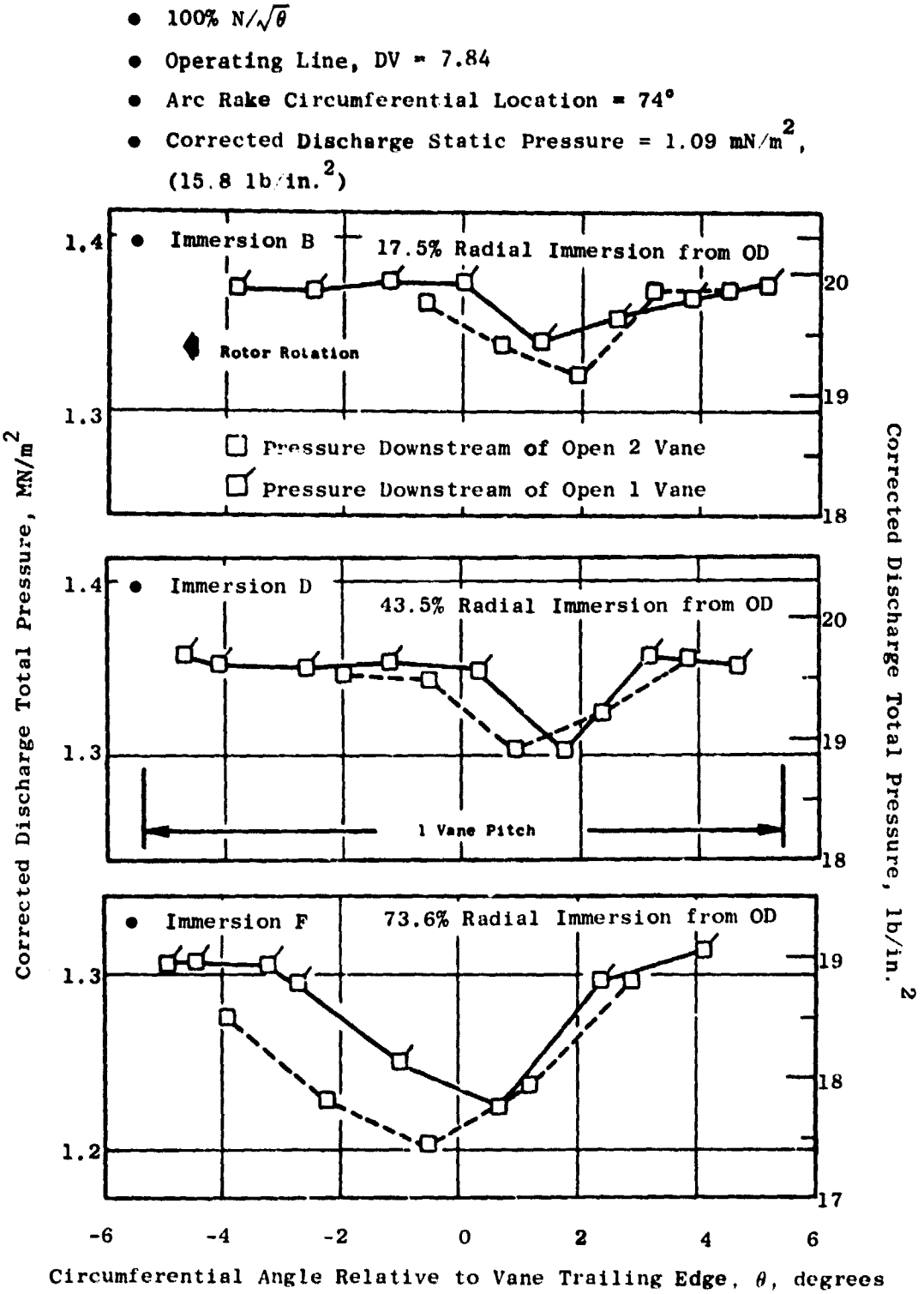

Figure 22. Circumferential Pressure Profile for Open 2–Open 1 Vane Passage.

- Location of the vane wake relative to the trailing edge differs between vane types, reflecting the differences in exit swirl angles.

- Vane wakes are typically wider and deeper in the hub region.

The most significant observation was the high loss level indicated for the inner two immersions at F and G. At nominal bypass ratio, a portion of the flow which passes under the island and through the core OGV spills over the splitter and into the bypass duct. This portion is 1.6% of total fan flow by design intent. Mixing was expected to wash out the swirl discontinuity and localize any negative incidence effects to the bypass OGV hub. However, the arc rake data indicated that the affected region was considerably larger than would be expected from consideration of the amount of flow involved. Figure 23 shows the effect of bypass ratio variation, which directly impacts the quantity of flow under the island that is spilled into the bypass stream on the loss profile. This figure indeed confirms that the loss level at the two hub immersions is influenced by the spilled flow in that reduction in the bypass ratio resulted in significantly lower losses in the Bypass OGV (vane frame) hub. This suggests that the high-loss mechanism is not inherent in the vane frame, but rather in the condition of the upstream flow. A list of possible mechanisms would include:

- An unfavorable boundary layer shape factor at the bypass OGV hub inlet due to mixing.

- Vortex formation in the shear region.

A comparison of the circumferential profiles in the hub region for the bypass ratio variations is presented in Figure 24 and dramatically illustrates the reduction in wake size at low bypass ratio.

The geometry of the OTW engine vane frame is common to that of the UTW engine. In the OTW engine fan configuration the splitter extends forward to the fan rotor. Accordingly, it is expected that the high vane frame hub loss will be diminished in the OTW configuration.

The effect of bypass throttling is shown in Figure 25. For the two more-throttled conditions which encompass the design and maximum cruise operating lines, the profiles and levels are similar. The unthrottled case, which is well below the takeoff operating line, showed significantly higher losses, particularly in the hub and tip regions of the open 2 vane set.

A comparison of the loss profiles for the three rotor pitch angles is shown in Figure 26. The profiles are similar, but opening the rotor blade increased the overall loss level. Because of the difference in airflow levels between blade pitch settings, an attempt was made to separate out this effect by defining an overall loss coefficient based on the downstream dynamic pressure. The results are summarized as follows:

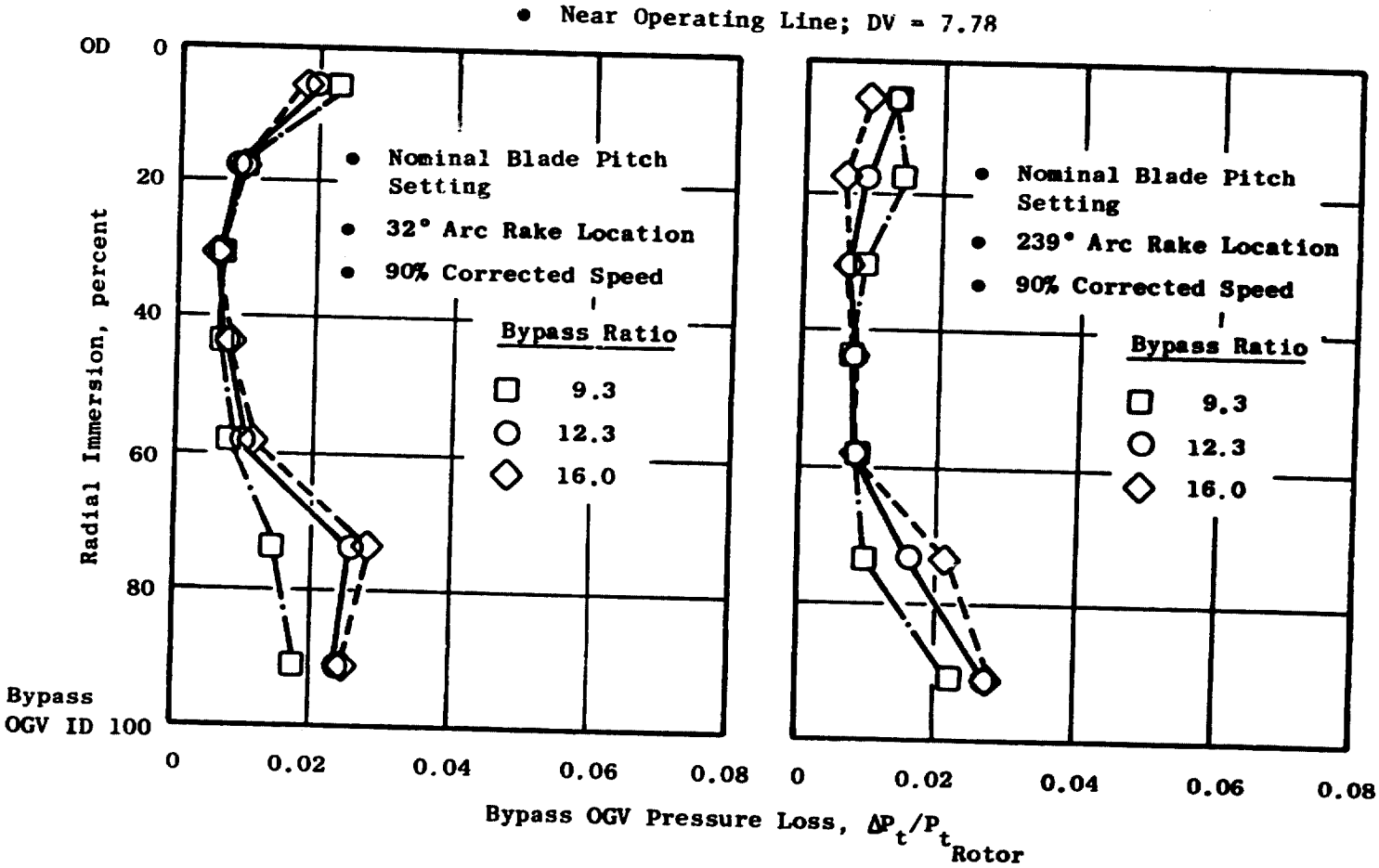

Figure 23. Effect of Bypass Ratio on Bypass OGV Pressure Loss.

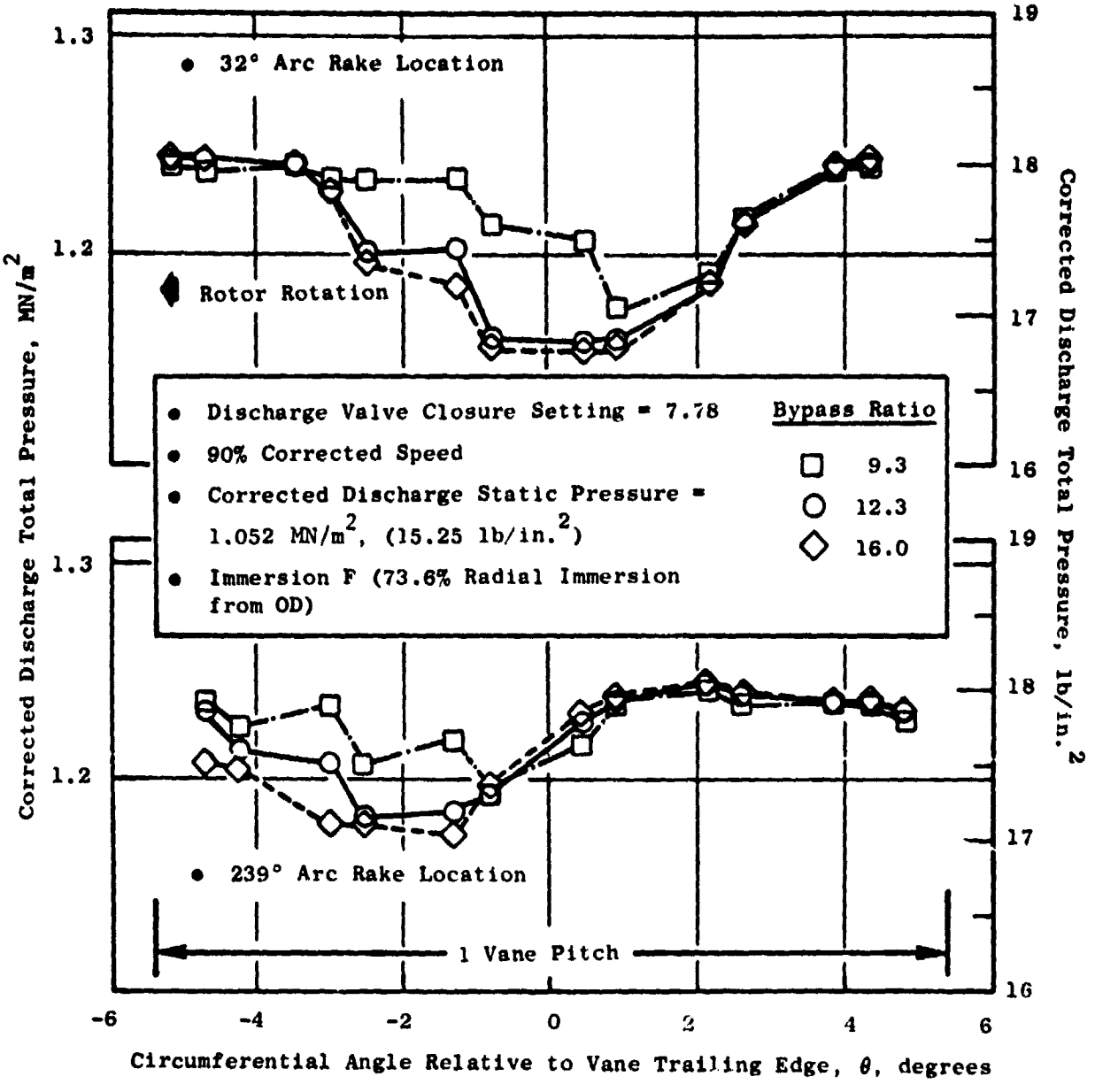

Figure 24. Effect of Bypass Pressure Ratio Variation on Bypass OGV Outlet Circumferential Pressure Profile.

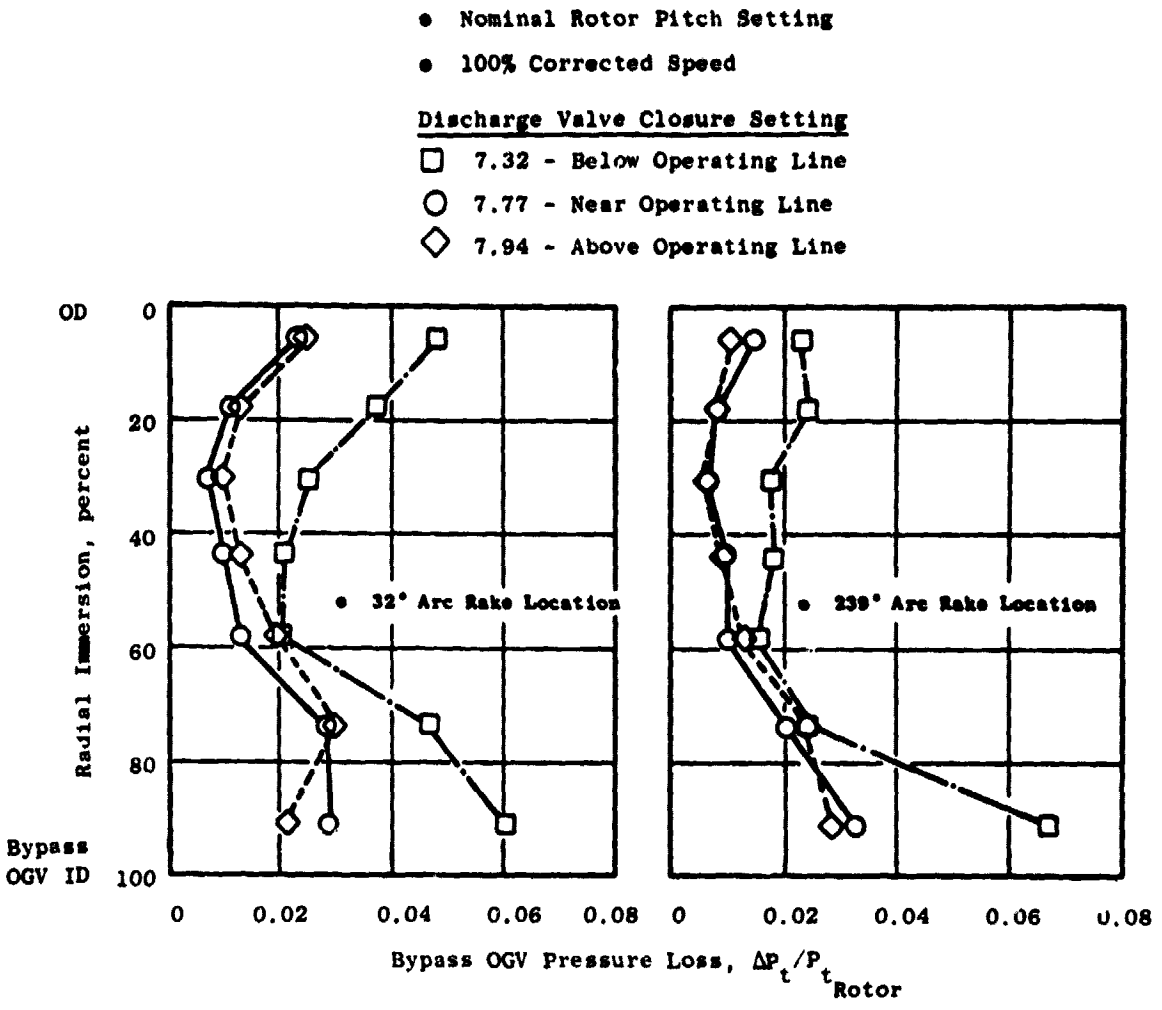

Figure 25. Effect of Throttling on Bypass OGV Pressure Loss.

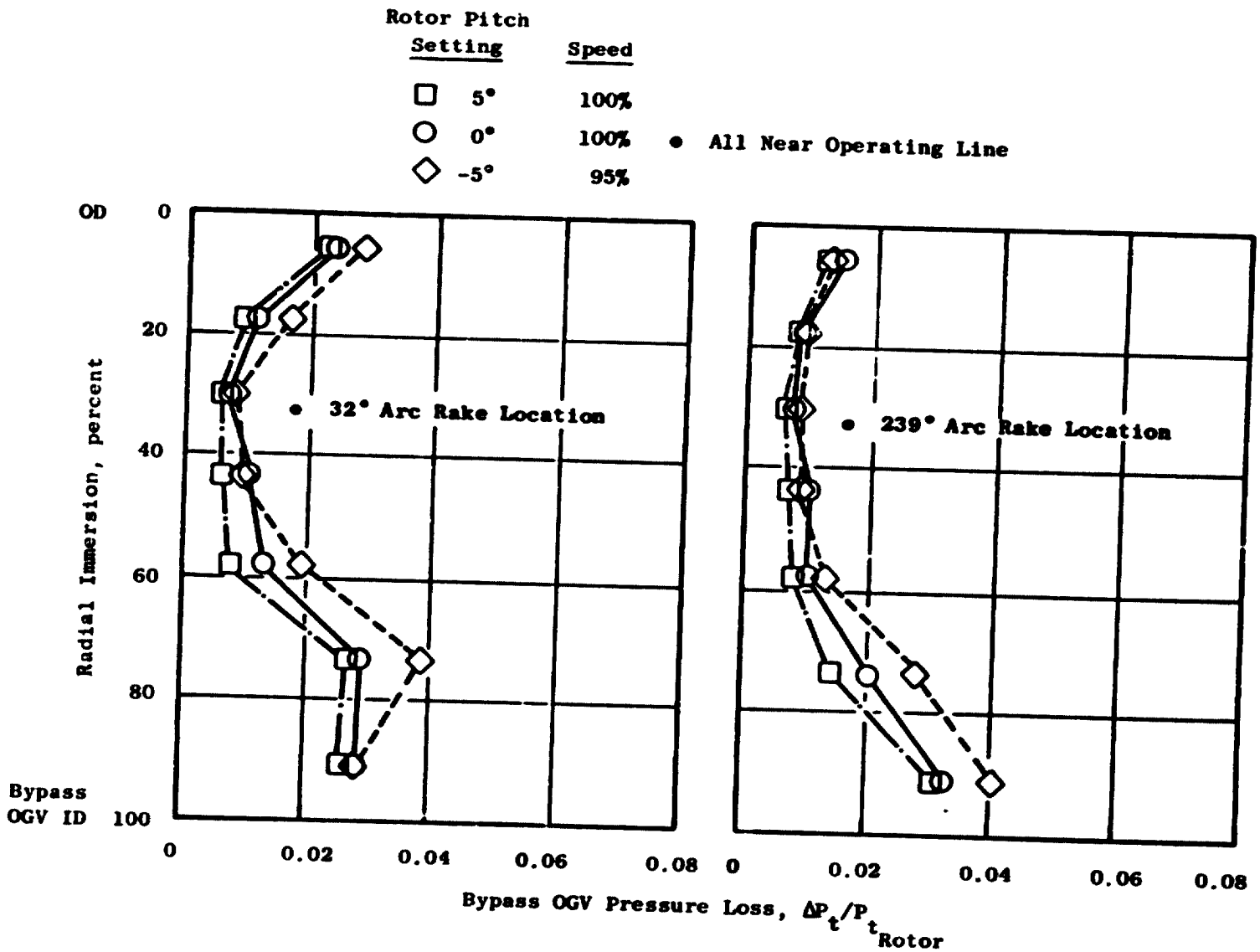

Figure 26. Effect of Rotor Pitch Angle Variations on Bypass OGV Outlet Radial Pressure Loss Profiles.

Pitch Angle	$\frac{(\Delta P_t)\ OGV}{P_{t_{14}} - P_{s_{14}}}$
-5°	0.099
0°	0.087
+5°	0.084

On this basis, it is apparent that part of the OGV loss increase at -5° pitch is attributable to incidence angle mismatch, the other part being attributed to the higher Mach number environment.

Representative bypass OGV outlet circumferential temperature profiles for selected immersions are shown in Figure 27. The primary observations for these data are:

- Significant temperature variation across vane passage (evidence of streamline warping/secondary flow).
- Variation in average level between arc rake locations.
- Relatively low temperature associated with wake region (determined by looking at wake location relative to trailing edge in Figure 21 and comparing with the temperature profiles in Figure 27).

5.6 INDUCED CIRCUMFERENTIAL FLOW DISTORTION AT BYPASS OGV INLET

A circumferential variation of flow forward of the bypass outlet guide vanes is inherent in the nonaxisymmetric design of the five distinct vane types. Analytical studies of this configuration predicted flow deficiencies in the vicinity of the vane passages formed between different vane types. The distortion of this analytical model diminished rapidly forward of the vane row such that no effect of any consequence was expected on the rotor blade. Furthermore, the operating range of the outlet guide vanes was estimated to be sufficient to accept the calculated distortion without significant performance penalty.

Static pressure taps, strategically located around the OD circumference at both the rotor discharge plane and the OGV inlet plane, were used to measure the magnitude and extent of the expected distortion. The results obtained at nominal pitch and design speed are expressed in terms of the average dynamic pressure, as shown in Figure 28. The measured dynamic pressure distortion of $\pm$10% at the OGV inlet and +5% to -2% at the rotor discharge compare favorably to the analytical predictions. The implication is that this induced circumferential distortion in the flow field should not have any significant detrimental effects on the operational characteristics of the fan. This result adds assurance that, when incorporated into the QTW engine configuration, there will be no effect of any consequence.

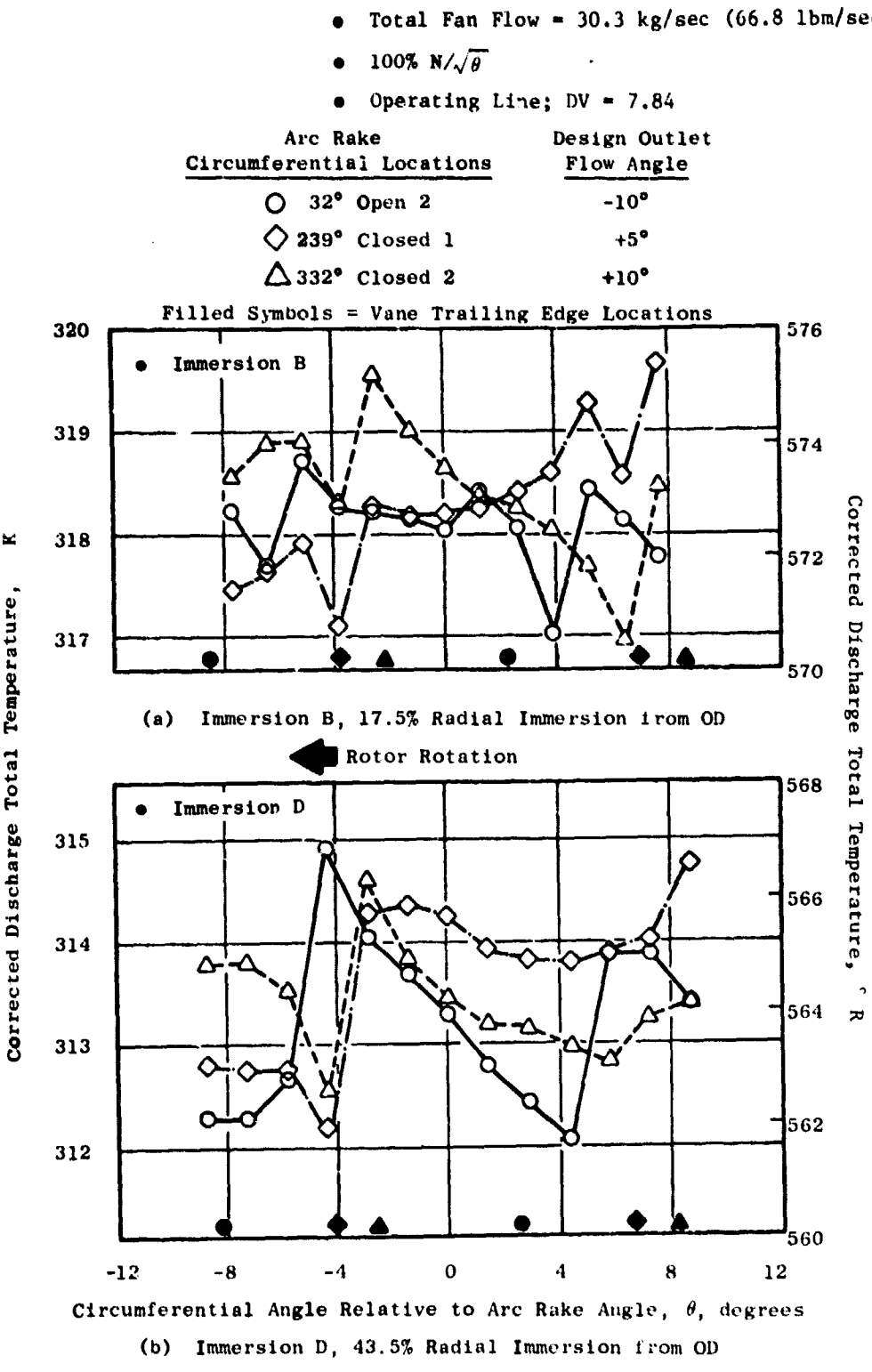

Figure 27. Bypass OGV Vane Passage Circumferential Temperature Profiles at Various Circumferential Locations.

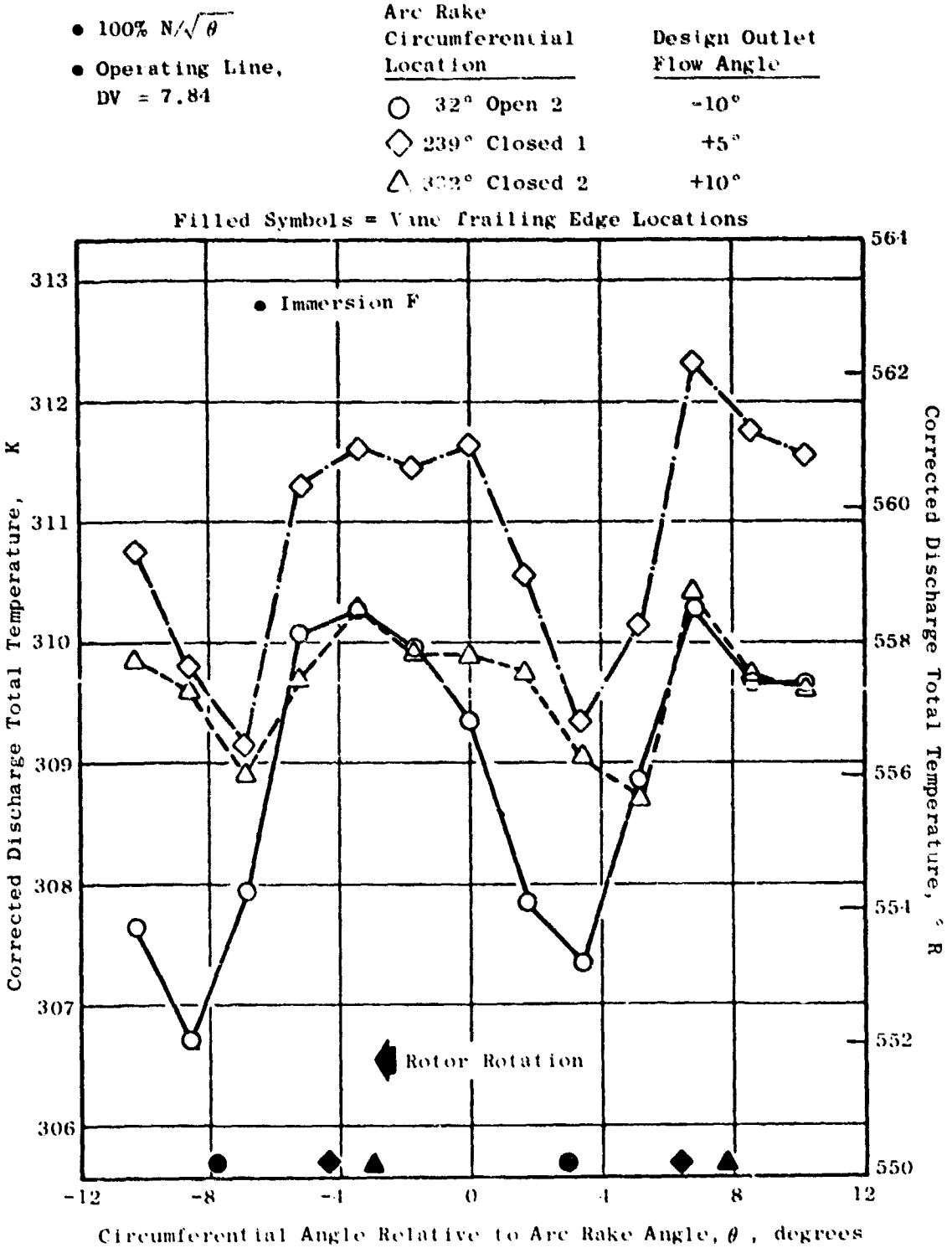

(c) Immersion F, 73.6% Radial Immersion from OD

Figure 27. Bypass OGV Vane Passage Circumferential Temperature Profiles at Various Circumferential Locations (Concluded).

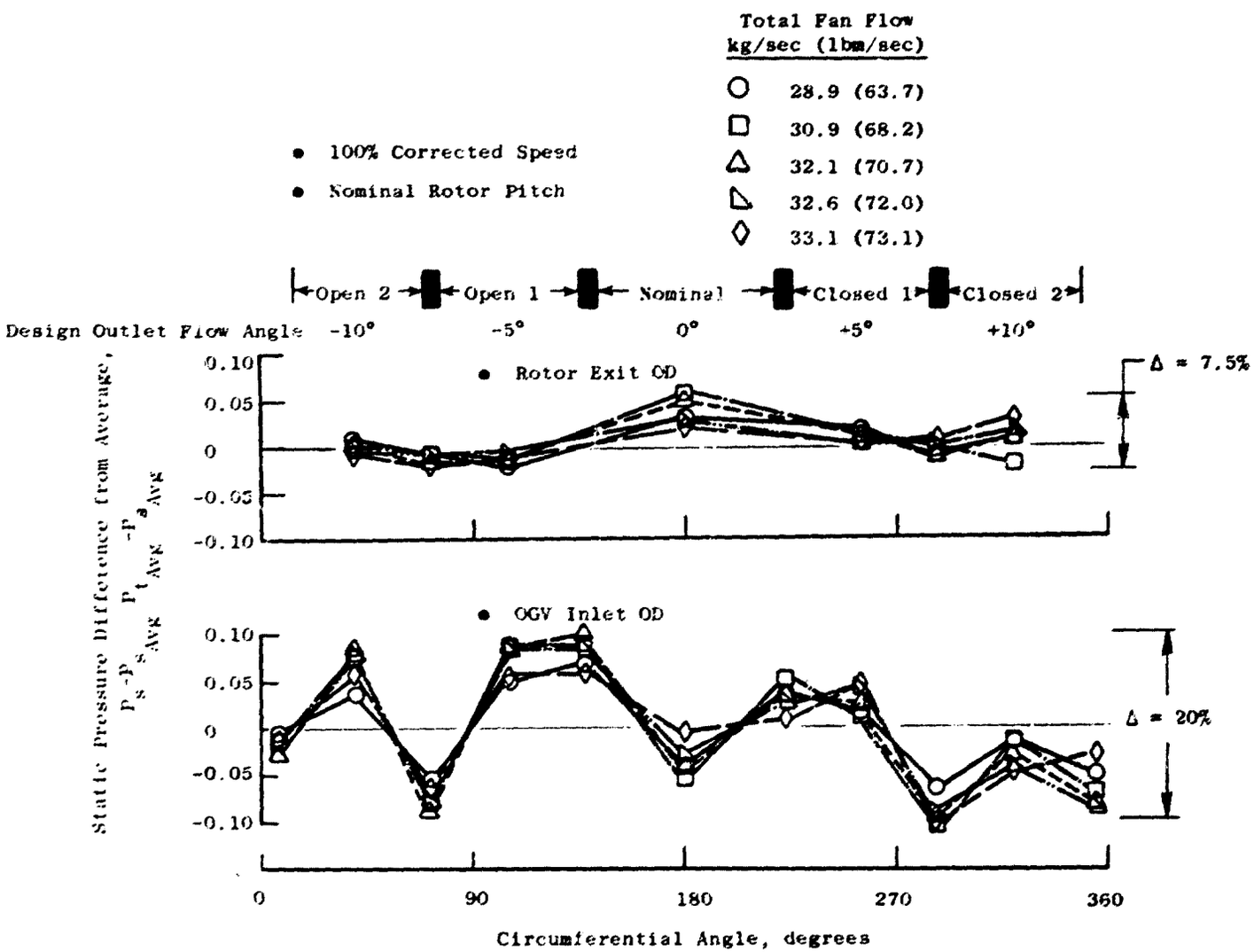

Figure 28. Effect of Throttling on Circumferential Static Pressure Distortion (OD) at Rotor Exit and OGV Inlet.

5.7 BYPASS RATIO EXCURSION

Tolerance of the splitter region and the core flow to off-design bypass ratio operation was investigated. A fan corrected speed of 90% was selected as representative of conditions where off-nominal bypass ratios might be encountered in actual engine operation. Data were taken at five core discharge valve settings while holding the bypass discharge valve constant.

Static pressure taps around the splitter nose and along the hub surface indicated that the system operated satisfactorily at the nominal bypass ratio, as shown in Figure 29. There was no excessive flow acceleration or diffusion along the walls until the bypass ratio reached extreme values. Over the splitter, at larger-than-nominal bypass ratios,the flow rapidly accelerated behind the nose due to the high effective angle of attack of the stagnation streamline and then diffused to the higher pressures at the vane frame inlet. Below the splitter, as the bypass ratio is decreased, the static pressure along both walls decreased as the flow accelerated into the transition duct.

Radial profiles at the exit from the transition duct are shown in Figure 30 for each of the five bypass ratio settings. Overall fan hub (simulated core inlet) efficiency and pressure rise attained maximum values at the nominal bypass ratio setting of 13.2. However, the pressure ratio and efficiency were relatively insensitive to bypass ratio between values of 9 and 16. As bypass ratio was reduced, a gradual deterioration in the radial profile at the hub was observed. The tip remained relatively healthy until the lowest bypass ratios were reached. Separation from the splitter lip due to off-incidence operation was probably responsible. The total temperature profile showed very little effect throughout the bypass ratio migration, either in level or in shape. This indicates that the bypass ratio migration had little, if any, impact on the operation of the rotor.

5.8 EFFECT OF HIGH MACH INLET ON FAN AERO FORWARD PERFORMANCE

Limited fan aerodynamic performance data were obtained in the forward thrust mode with the accelerating inlet configuration and are presented in Figure 10. These data were not adjusted by the methods in Appendix B, so a consistent comparison with bellmouth inlet data requires the latter to also be unadjusted. Figure 31 illustrates this by comparing corresponding bellmouth inlet unadjusted data points for the nominal ($\delta p = 0°$) rotor pitch angle with data on two speed lines with the accelerating inlet installed (from Figure 10.) It was observed that the overall rotor bypass performance was unchanged along the 90% speed line. At the higher flow rates of the 105% speed line data, the performance with the accelerating inlet was slightly down from that measured with the bellmouth by approximately 1 point in adiabatic efficiency. This may be due to the thickened rotor tip inlet boundary layer set up by the lower total pressure recovery of the accelerating inlet as fan flow increases. This efficiency penalty was not considered to be of sufficient magnitude to warrant a detailed investigation of the differences in rotor blade element performance. Based upon the comparisons in Figure 31, it was concluded that the accelerating inlet should not have severe detrimental effects on the performance characteristics of the fan as measured with the bellmouth inlet.

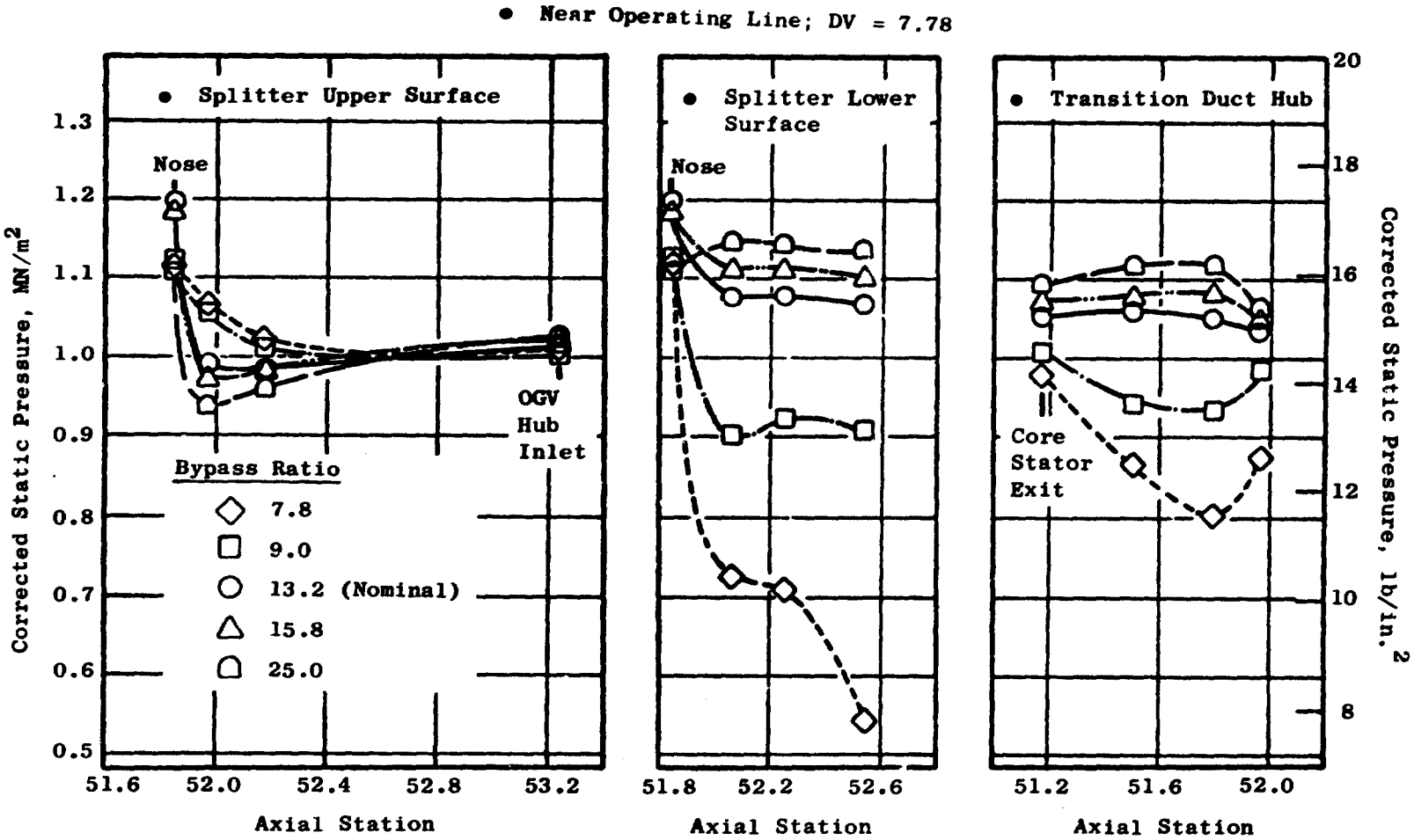

Figure 29. Effect of Bypass Ratio Variations on Splitter Leading Edge Region Static Pressures with Nominal Rotor Pitch (β_P = 0°) at 90% Speed.

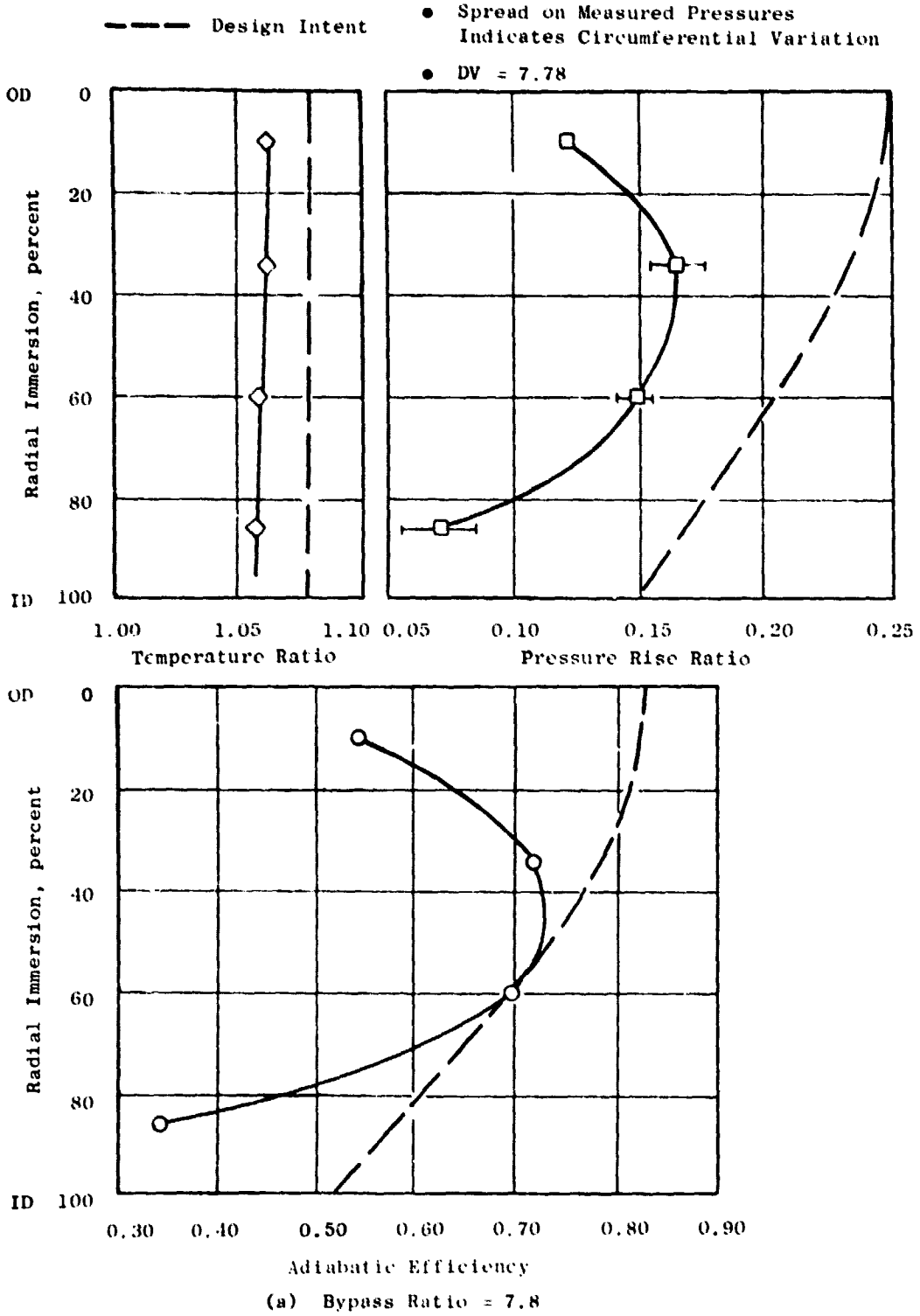

(a) Bypass Ratio = 7.8

Figure 30. Comparison of Radial Profiles of Temperature Ratio, Pressure Rise Ratio, and Adiabatic Efficiency at Transition Duct Discharge for Various Bypass Ratios at 90% Speed with Nominal Rotor Pitch ($\beta_F = 0°$).

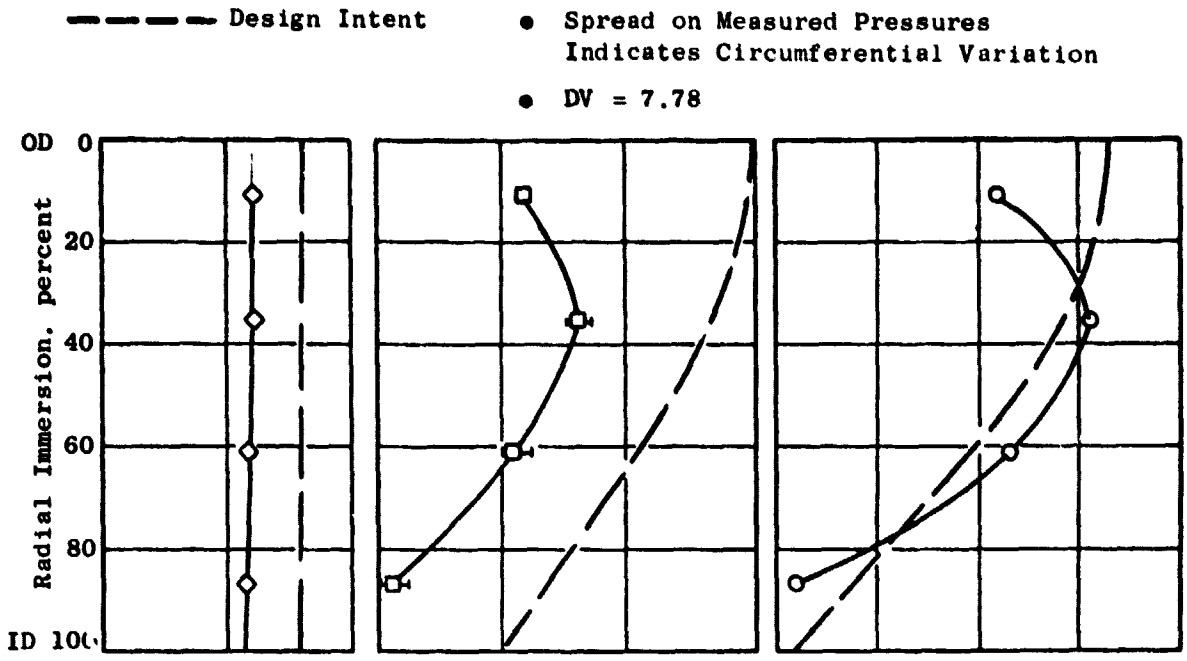

(b) Bypass Ratio = 9.0

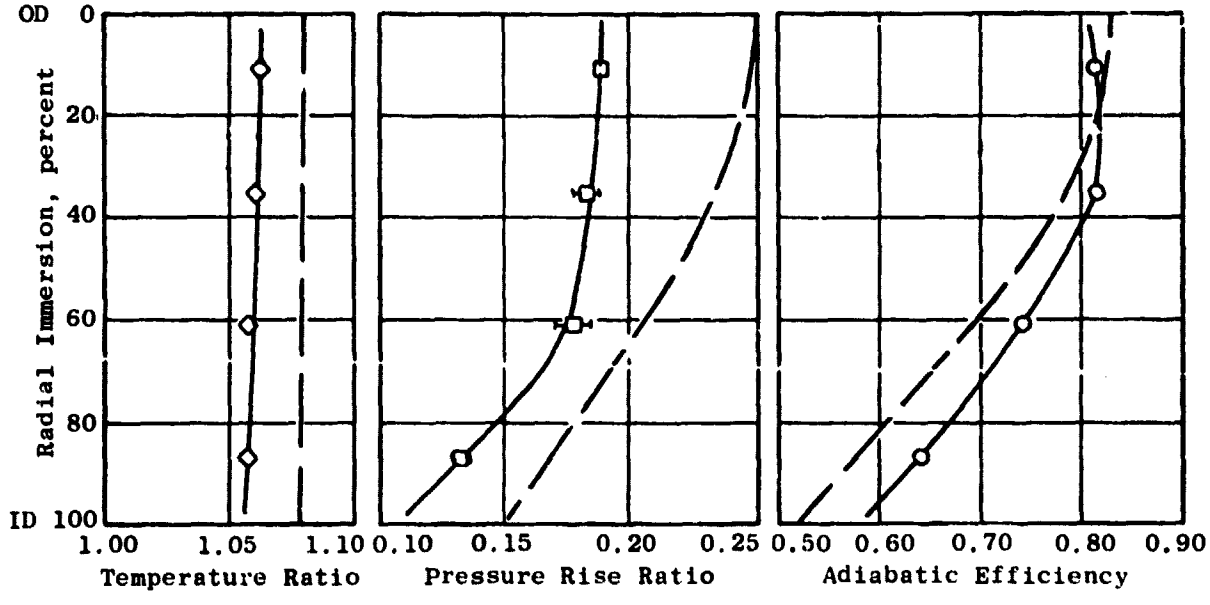

(c) Bypass Ratio = 13.2

Figure 30. Comparison of Radial Profiles of Temperature Ratio, Pressure Rise Ratio, and adiabatic Efficiency at Transition Duct Discharge for Various Bypass Ratios at 90% Speed with Nominal Rotor Pitch (β_F = 0°) (Continued).

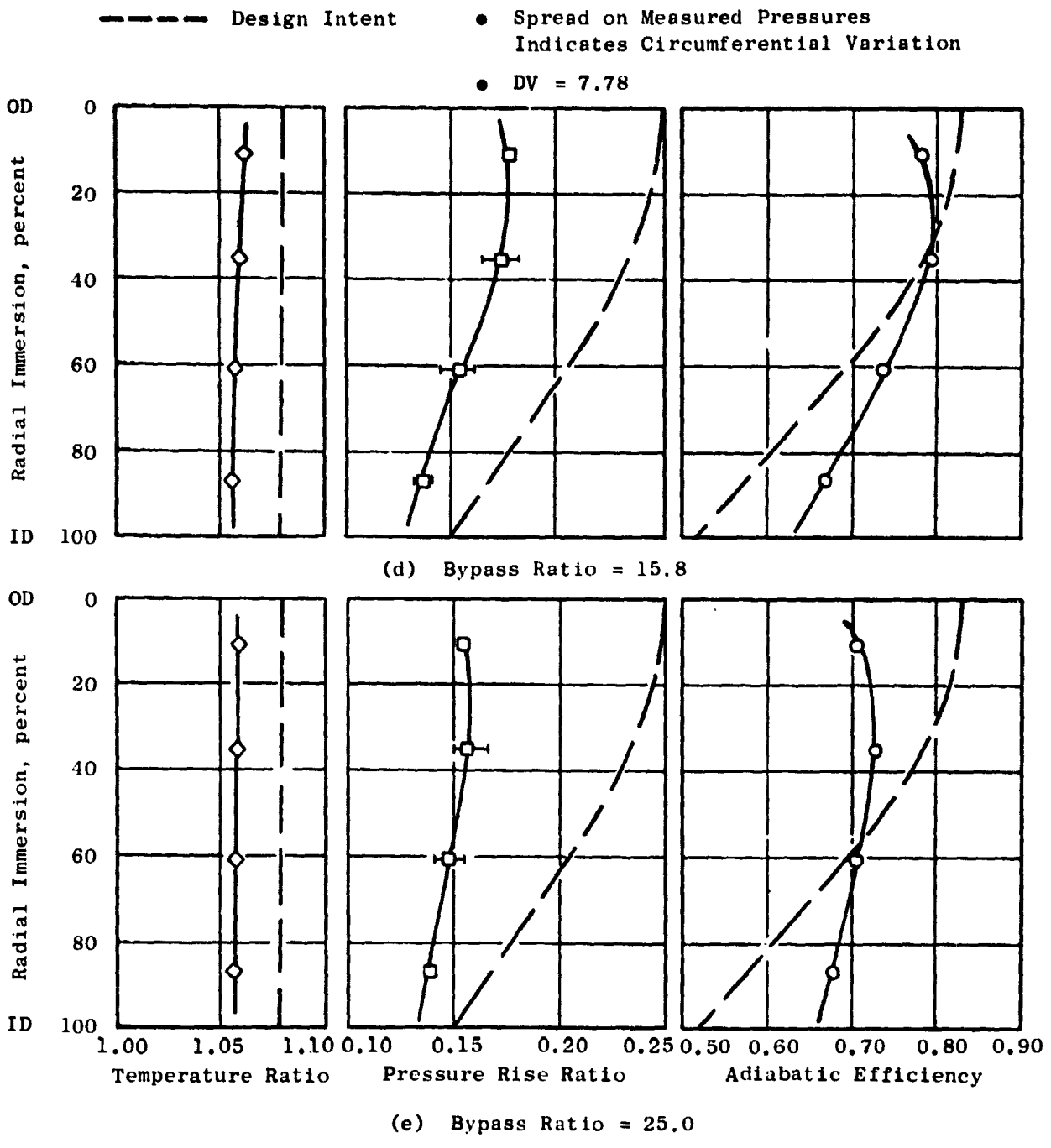

Figure 30. Comparison of Radial Profiles of Temperature Ratio, Pressure Rise Ratio, and adiabatic Efficiency at Transition Duct Discharge for Various Bypass Ratios at 90% Speed with Nominal Rotor Pitch (β_F = 0°) (Concluded).

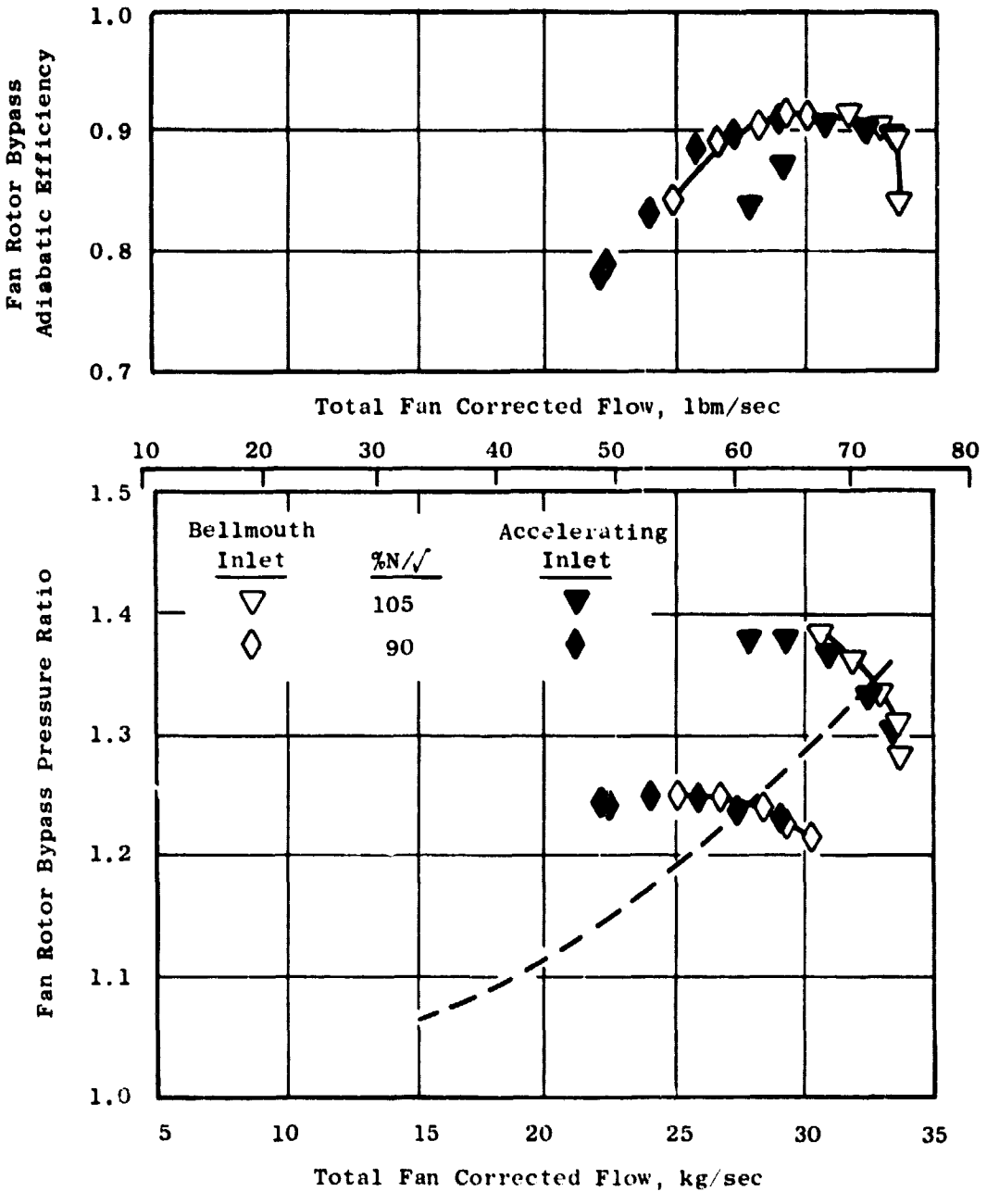

Figure 31. Comparison of Fan Rotor Bypass Performance with Bellmouth Inlet and Accelerating Inlet at Nominal Pitch Setting (θ_F = 0°).

Referring to Figure 10 and Section 5.1, it is shown that sufficient operating margin is available with the accelerating inlet, so that fan stall or blade aeromechanical instability should not present operational problems with this inlet installed.

SECTION 6.0

TIP RADIAL INLET FLOW DISTORTION IN FORWARD MODE

The nominal pitch forward mode configuration, using the scale model of the UTW engine bellmouth inlet, was tested with a tip radial inlet flow distortion. The distortion-generating screen covered the outer 40% of the inlet annulus area. A measured distortion of 16%, defined as the difference between maximum total pressure and minimum total pressure divided by the maximum, was produced at the design flow of 31.9 kg/sec (70.4 lbm/sec).

The fan-bypass-stream performance map with tip radial inlet flow distortion is shown in Figure 32. Operating limits, in the form of rotating stall or high rotor stress, were determined at all speeds, as discussed in Appendix C. Superimposed on the fan map for comparison is the stall line obtained with undistorted inlet flow. At corrected speeds up to 90%, the distorted inlet stall line was well above anticipated engine operating conditions. At corrected speeds above 90%, a significant loss in operating margin was observed, with the largest loss occurring at 95% corrected speed. At 100% corrected speed, the only speed at which rotating stall was encountered for both distorted and undistorted flows, the sensitivity of the fan to the tip radial distorted inlet flow is in line with the results observed from other fans.

Fan hub performance with tip radial distortion is compared to data from clean inlet tests in Figure 33. For the distortion data, the inlet pressure was taken as the local hub value from the inlet rakes, rather than the average inlet pressure for the whole fan. Total fan flow is corrected by the average inlet pressure in order to be consistent with the bypass stream performance map. It is clear that the tip radial distortion prevents the fan hub region from producing as much pressure rise as it is capable of producing with clean inlet flow. This could have an adverse effect upon the core engine's ability to produce power to drive the fan, although it is somewhat offset by the tendency for the fan hub region to exceed its hub supercharging objectives, as described in Section 5.3.

The mechanism which limits fan hub pressure rise is apparent from Figure 34, a representative 95% speed operating point. Despite the fact that rotor tip exit total pressure is lower than at the undistorted pitchline region, the tip total-pressure rise ratio based on the local inlet pressure is quite high. Thus, it is not possible for the rotor tip to produce an appreciably higher pressure rise. Pressure levels at the inner immersions of the fan, however, are related to those of the tip region through the radial equilibrium of static pressure: the inability of the tip to sustain higher loadings limits the absolute level of fan exit pressure at all immersions. An alternate way to visualize this is to observe that the tip sees high-incidence angles because of the low inlet flow in the distorted region, loading the

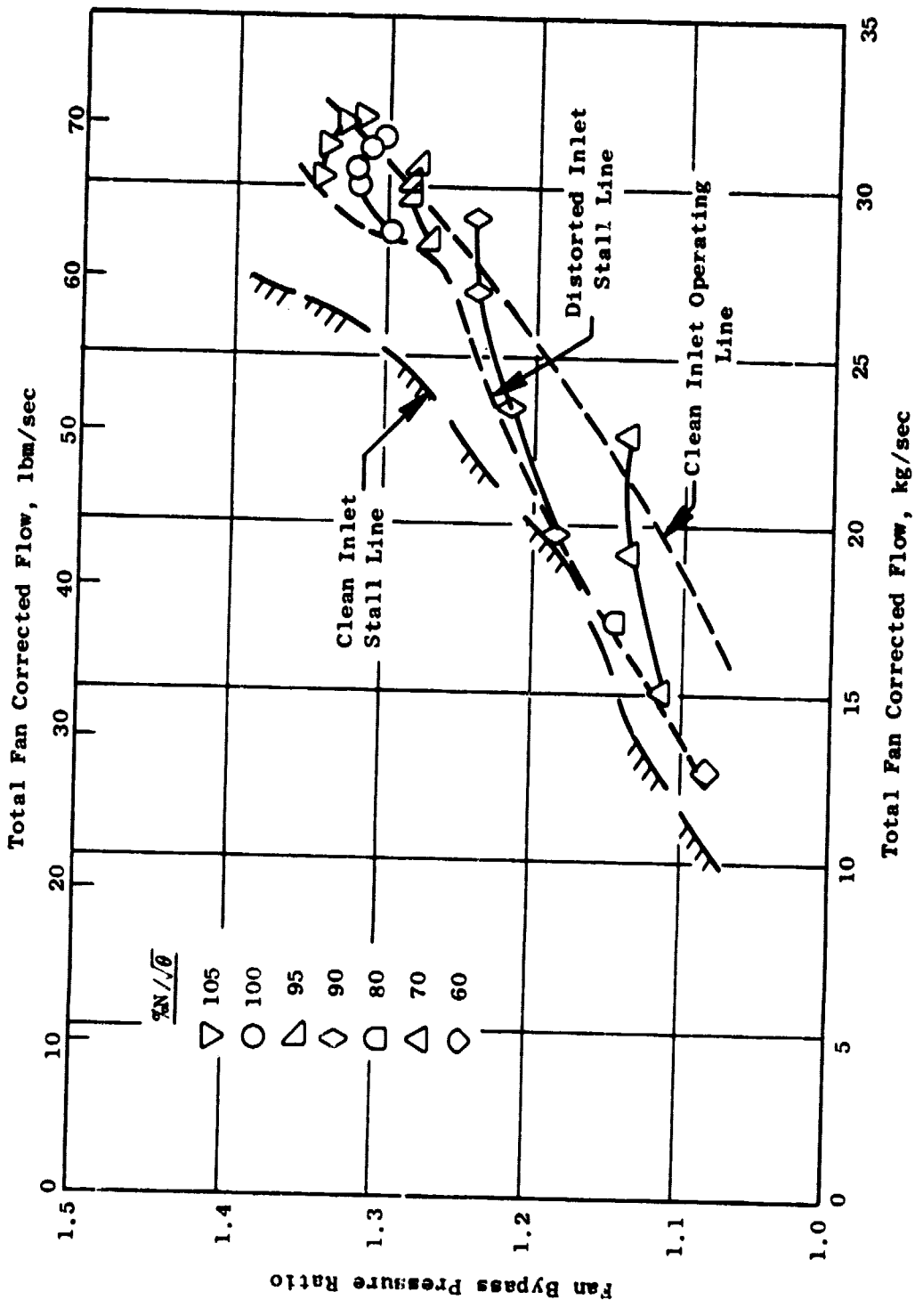

Figure 32. Fan Performance Map at Nominal Rotor Pitch, Forward Mode, (β_P = 0°) for Tip Radial Inlet Flow Distortion.

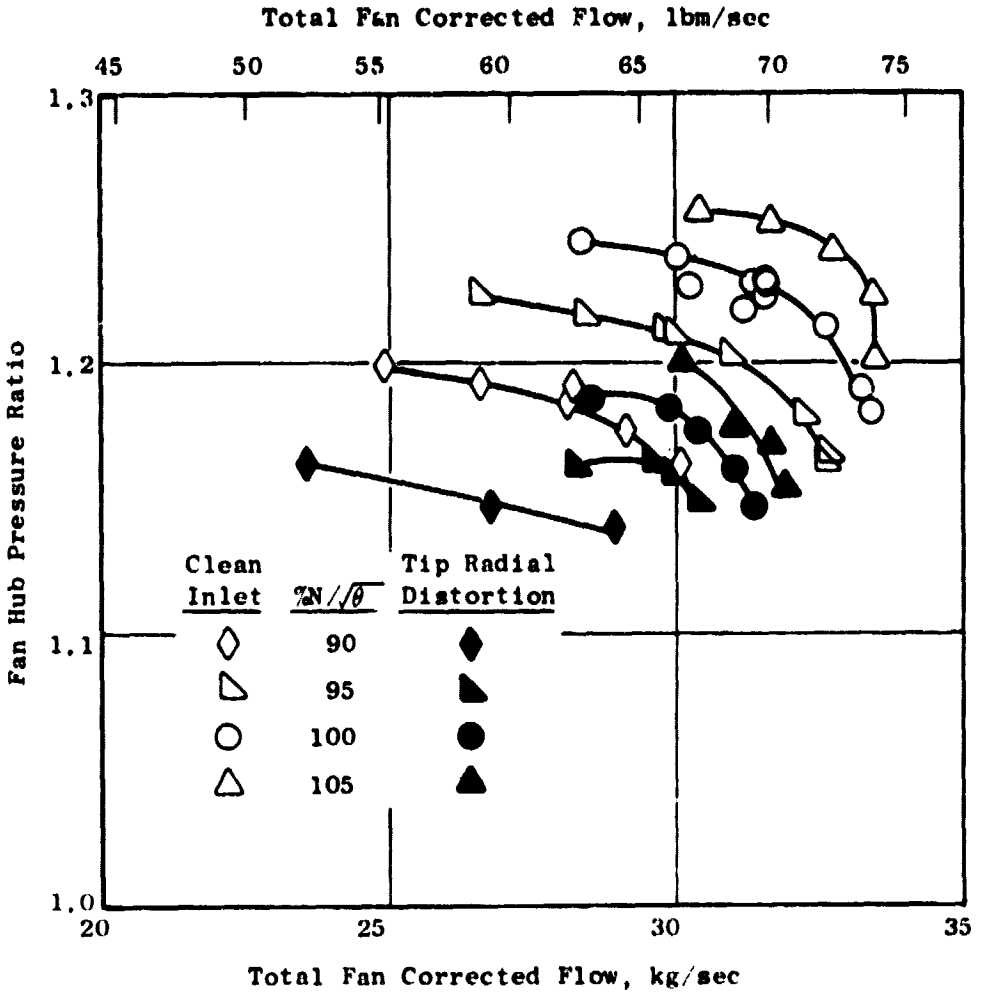

Figure 33. Comparison of Fan Hub Performance at Nominal Pitch Setting (β_F = 0°) with Tip Radial Inlet Flow Distortion and Clean Inlet Flow.

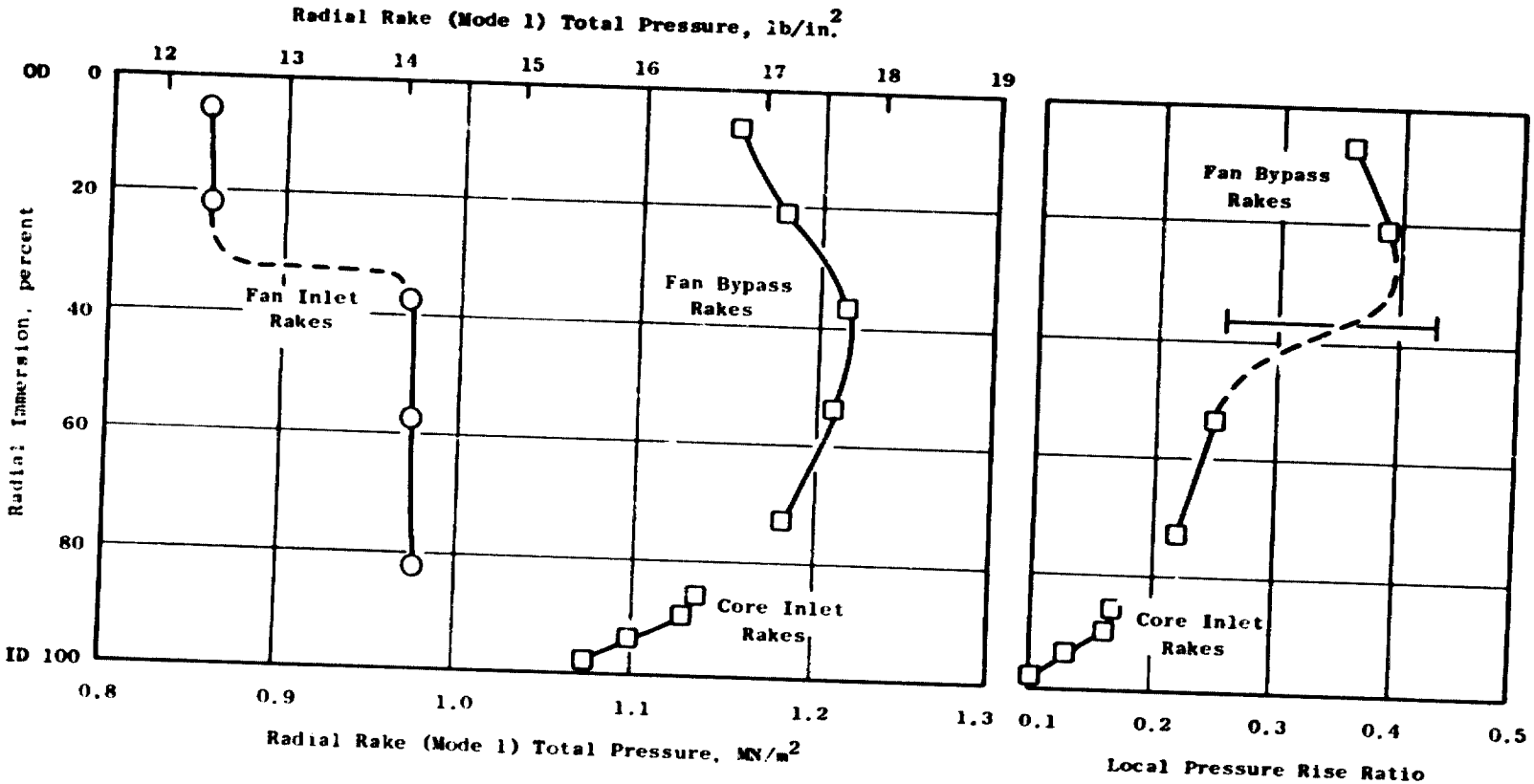

Figure 34. Radial Profiles of Inlet, Fan Bypass, and Core Inlet Pressure for Tip Radial Distortion at 95% Speed with Nominal Rotor Pitch (θ_F = 0°).

tip, while the hub incidence is reduced by the diversion of flow from the tip, thus unloading the inner region. These considerations dictate that hub region total pressures will be generally lower than those near the tip. The limitation on rotor tip exit pressures created by the tip radial distortion prevents the undistorted region from throttling.

A comparison of fan hub (core inlet) radial profiles with clean inlet and tip radial distortion shows the profiles exhibit the same shape, but differ mainly in the measured levels of pressure. So, when operating with a tip radial distortion into the fan, the overall core system pressure rise will be lower, but the core compressor inlet radial distortion should not be any worse than with clean fan inlet operation.

Fan hub efficiency for tip radial distortion is lower than for clean inlet operation; at comparable points where the hub is producing the same amount of work or temperature rise, the pressure rise is less.

SECTION 7.0

REVERSE MODE PERFORMANCE

Reverse mode performance was obtained with the configuration and instrumentation shown in Figure 45. Outside ambient air was drawn through the bypass outlet line and discharge valve (DV) and into the bypass OGVs. Simulated core flow was drawn through a separate valve and line.

An accelerating (high Mach) inlet was installed for all reverse mode testing since this represents the configuration of the UTW engine. The bypass discharge valve was set at 6.37 on its relative position indicator. This setting was determined as follows: Model tests of the UTW engine bypass exhaust nozzle, in the reverse-thrust configuration, yielded the radial-total-pressure profile at the OGV trailing edge plane for a simulated forward flight speed of 85 knots, shown in Figure 35. The discharge valve was slightly closed to achieve a radial-total-pressure profile which simulated the model result. The actual simulator-measured radial profile is also shown for the selected 6.37 discharge valve position and for a fully-open discharge valve setting at a representative test condition. The acoustic splitter was not included in the simulator test vehicle. Overall total pressure recovery at the bypass OGV trailing edge is shown in Figure 36, which provides a consistency check on the flow entrance system. Note that except for four selected conditions, the discharge valve setting was 6.37. The effect of closing the DV to 6.37 at high flow is to reduce the total pressure recovery from about 99.2% to 98.0%.

Testing in the reverse mode of operation was performed at pitch angle settings of (open) -95°, -100°, and -105° in the reverse-through-stall-pitch direction and at pitch angle settings of (closed) +73° and +78° in the reverse-through-flat-pitch direction. The reverse mode aerodynamic performance data is summarized in Table II.

7.1 FAN PERFORMANCE IN REVERSE MODE

Overall reverse mode performance of the fan is shown in Figure 37. These results represent measured test data that have been adjusted by the methods described in Appendix B. Except for the flagged symbols, for which the discharge valve was fully open, the vehicle geometry was fixed for a given pitch setting.

In the reverse-through-stall-pitch settings, the reduction in flow, at speed, with more-open pitch settings, is consistent with expectations. The rather dramatic change in operating line was not expected, however. The pressure ratio-flow operating line characteristic is an expression, via continuity, of the flow through an effective discharge area. Changes to the

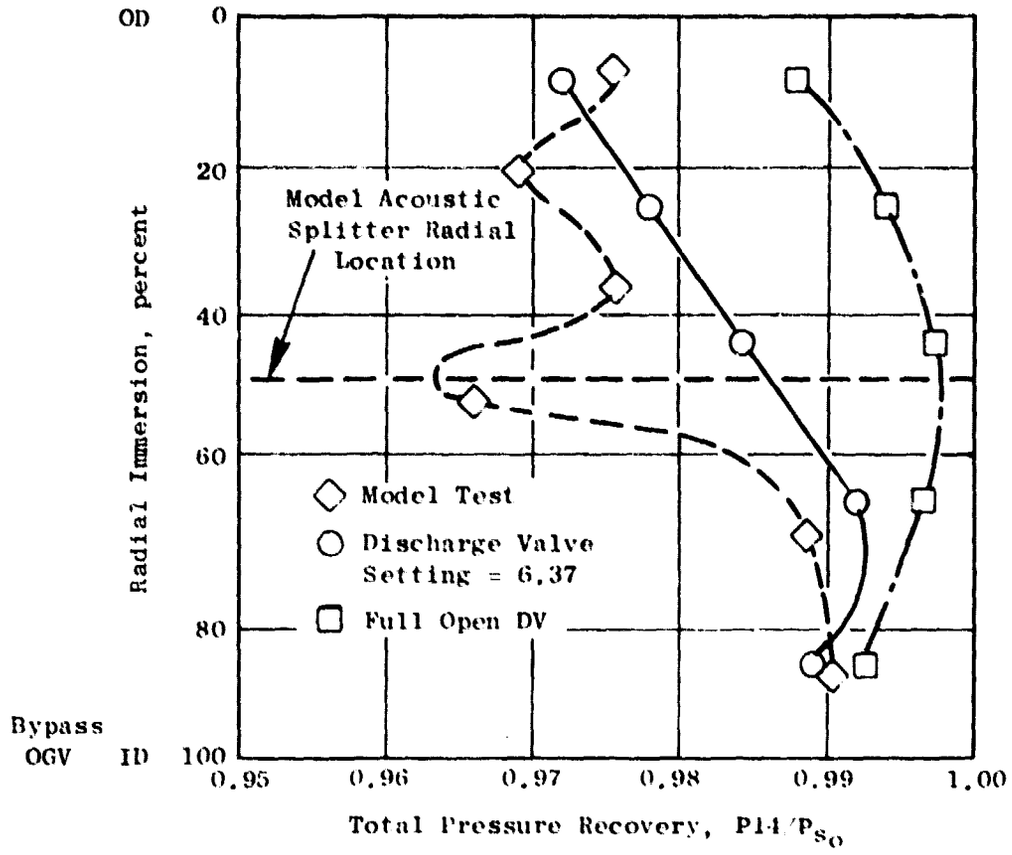

Figure 35. Radial Distribution of Total Pressure Recovery at Bypass OGV Trailing Edge with -100° (Open) Rotor Pitch at 90% Corrected Speed.

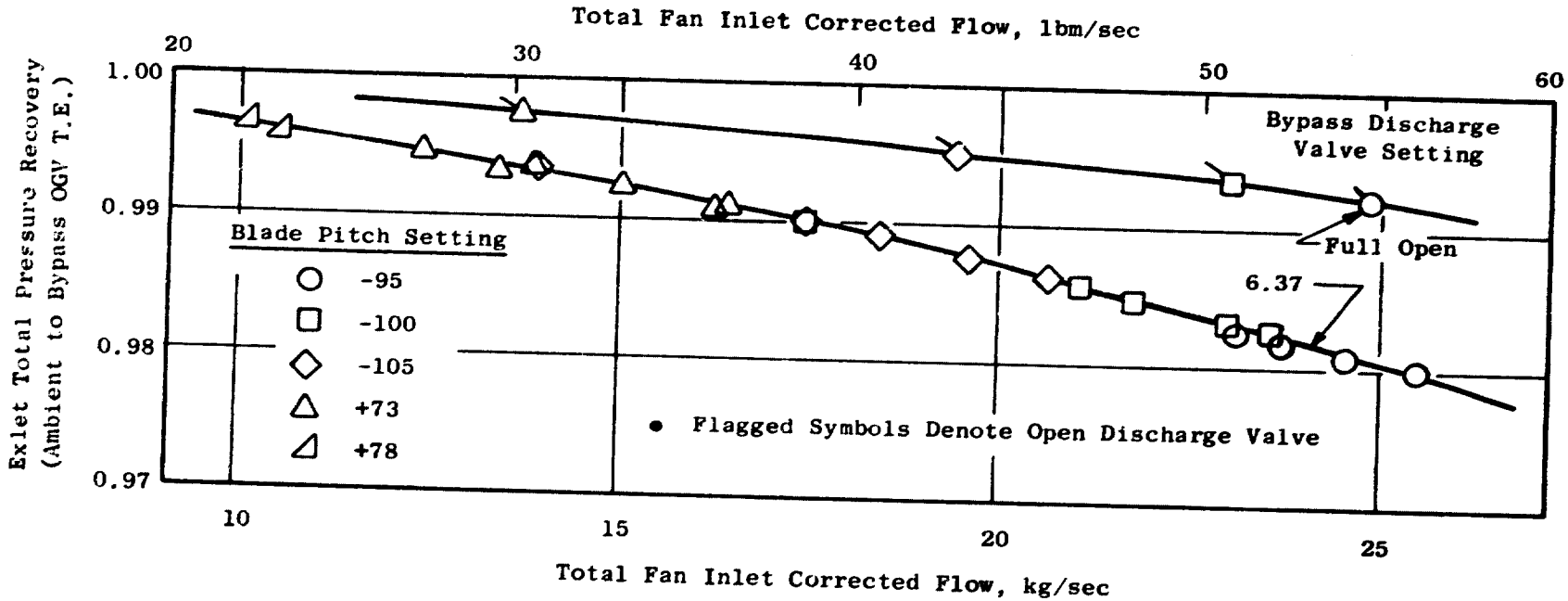

Figure 36. Effect of Blade Pitch Angle Variations on Bypass OGV Trailing Edge Recovery (Exlet Total Pressure Recovery) in Reverse.

Table II. UTW Simulator Data Tabulation, Reverse Mode, Accelerating Inlet.

β	Run	Rdg	$\%N/\sqrt{\theta}_{14}$	Rotor Flow, W_1, kg/sec	P_1/P_{14}	η_F	F_g/δ_o	T_1/T_{14}	Total Flow, W_{14}, kg/sec	P_{25}/P_{14}	Exit Swirl	P_{14}/P_{s_o}	D.V. Closure Setting
-95°	21	2	99.91	23.93	1.1919	0.410	763	1.1253	25.5	0.717	-19.65	0.9801	6.37
		3-10	90.03	22.93	1.1686	0.446	680	1.1020	24.6	0.742		0.9809	6.37
		11	89.95	23.22	1.1687	0.446	726	1.1022	24.9	0.728		0.9925	Open
		12	80.00	22.06	1.1484	0.496	609	1.0813	23.8	0.762		0.9819	6.37
		13	80.06	22.24	1.1531	0.521	626	1.0798	23.1	0.809		0.9827	6.37
		14	79.94	22.18	1.1499	0.505	616	1.0806	23.6	0.766		0.9821	6.37
-100°	22	1	100.07	21.87	1.1808	0.479	705	1.1015	23.6	0.775	-11.73	0.9829	6.37
		2-9	90.01	21.27	1.1562	0.518	631	1.0817	23.0	0.793		0.9833	6.37
		10	90.13	21.31	1.1594	0.532	671	1.0812	23.0	0.786		0.9938	Open
		11	80.07	20.04	1.1253	0.557	530	1.0616	21.8	0.818		0.9848	6.37
		12	79.95	20.05	1.1247	0.574	531	1.0595	21.1	0.846		0.9858	6.37
		13	60.07	15.74	1.0705	0.607	312	1.0324	17.5	0.898		0.9903	6.37
-105°	23	1	100.06	19.06	1.1474	0.518	565	1.0773	20.7	0.847	-6.69	0.9863	6.37
		2-13	90.02	18.18	1.1186	0.552	481	1.0589	19.6	0.865		0.9877	6.37
		14	89.97	18.03	1.1150	0.546	491	1.0579	19.4	0.860		0.9953	Open
		15	79.97	16.96	1.0908	0.577	390	1.0436	18.5	0.884		0.9891	6.37
		16	79.99	16.81	1.0888	0.587	384	1.0419	17.5	0.914		0.9902	6.37
		17	60.08	13.07	1.0496	0.585	224	1.0238	14.0	0.937		0.9939	6.37
+78°	24	1	64.92	9.82	1.0389	0.333	146	1.0330	10.6	0.959	-18	0.9960	6.37
		2	60.08	9.33	1.0333	0.330	128	1.0285	10.2	0.963	(Est.)	0.9968	6.37
+73°	25	1	110.0	15.09	1.1099	0.373	383	1.0810	16.4	0.911	-16.08	0.9912	6.37
		2	100.07	12.83	1.0728	0.324	266	1.0527	13.9	0.939		0.9938	6.37
		3	100.21	12.68	1.0745	0.330	275	1.0629	13.7	0.936		0.9977	Open
		4	90.09	11.53	1.0602	0.329	217	1.0512	12.4	0.950		0.9948	6.37
		6	90.02	11.50	1.0598	0.318	213	1.0527	13.4	0.918		0.9935	6.37
		7-14	110.0	14.98	1.1092	0.371	379	1.0810	16.3	0.912		0.9911	6.37
		15	105.0	13.90	1.0939	0.355	327	1.0731	15.1	0.927		0.9926	6.37

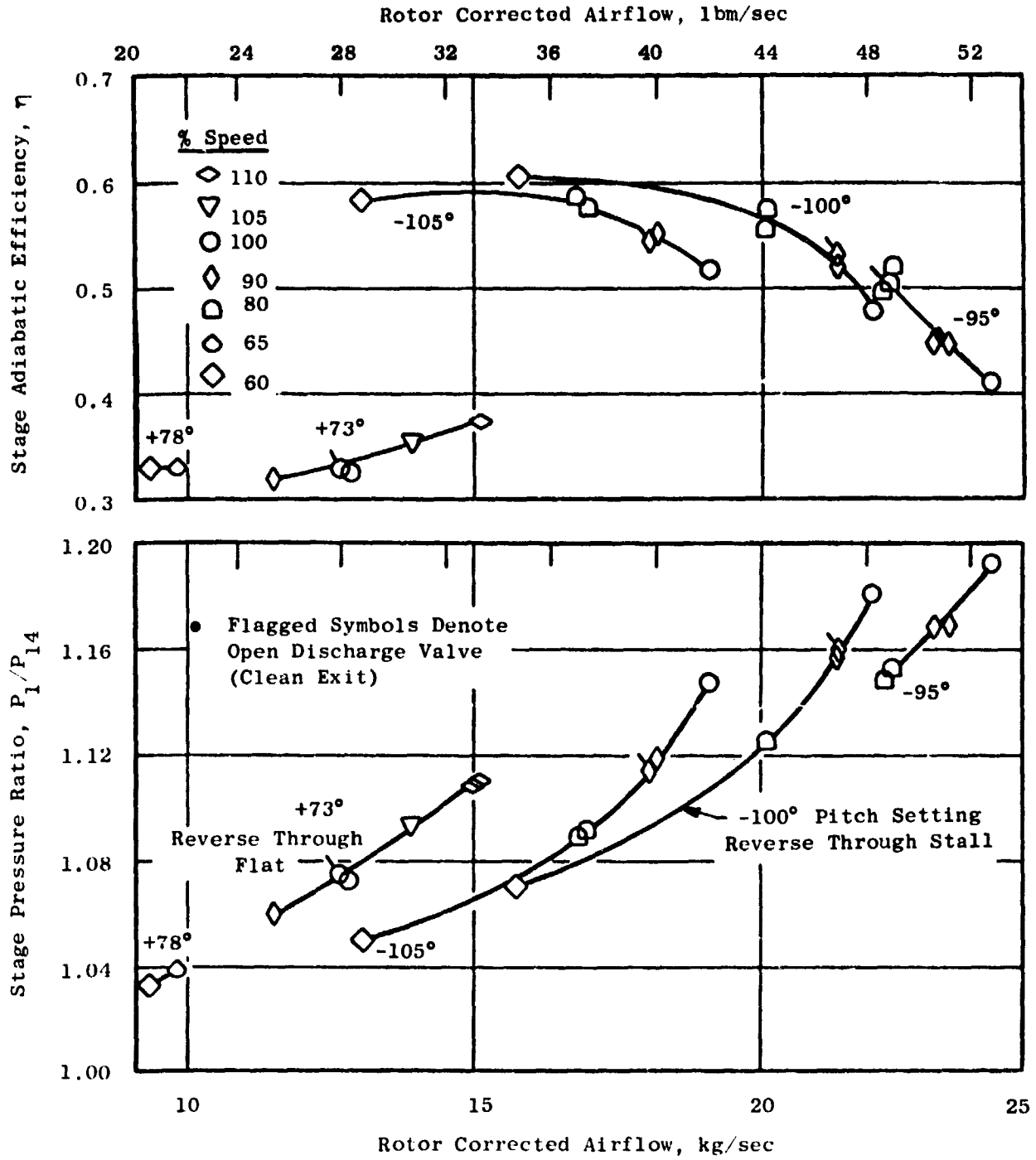

Figure 37. Reverse Mode Fan Performance at Various Blade Pitch Angles.

effective discharge area would be expected at different blade pitch settings due to changes in radial distributions and changes in effective fan flowpath. It is suspected that there is an interrelationship between these expected changes and the geometry of the inlet such that a different inlet geometry would result in a different operating line at otherwise the same fan geometry. This suspicion was implied by observations of data taken during acoustic testing with the low Mach inlet, described in Reference 4. The primary trend noted in adiabatic efficiency is a falloff with increasing flow. A smaller but noticeable effect of pitch angle is observed, with the highest efficiencies at the most negative (-105°) blade pitch angle. Above a nominal airflow of 15 kg/sec and 80% speed, efficiency decreases with increasing speed.

In the reverse-through-flat-pitch settings, the vehicle was restricted to a maximum speed of 65% at a pitch setting of +78° by high rotor stress. Flow and pressure ratio, and therefore reverse thrust, at the +73° setting are markedly reduced from the values obtained in the reverse-through-stall-pitch direction. Angle settings less than +73° were expected to result in even lower values. Since the +73° setting resulted in reverse thrust levels less than objective, further testing in the reverse-through-flat-pitch direction was terminated. A marked change in operating line from the reverse-through-stall-pitch setting is observed. At least a portion of this shift would be expected because of the marked difference in the rotor geometry between the two directions of reversal. The influence of pitch setting on the operating line in the reverse-through-flat-pitch direction is difficult to determine due to the limited data. Adiabatic efficiency is much lower than in the reverse-through-stall-pitch direction, probably because the blade camber is in the wrong direction.

The reverse mode flow-speed relationship is shown in Figure 38. The reverse-through-stall rate of flow increase with speed significantly diminishes at speeds above 80%. Although the 100% corrected speed tip speed is only 306 m/sec (1005 ft/sec), the counterswirl imparted by the bypass OGVs results in tip relative Mach numbers of 1.38 and 1.23 for -95° and -105° pitch settings, respectively, for an assumed counterswirl of 30°. Leading edge suction surface incidence angles and boundary layer shock interactions have significant potential effects on flow capacity at these Mach number levels. The reverse-through-flat-pitch rate of flow increase with speed, as shown in Figure 38, significantly increases at speeds above 100%. A contributing factor to this phenomenon may be the relative Mach number entering the rotor becoming supersonic; the resulting supersonic expansion around the leading edge tends to reduce the suction-surface separation which would occur during subsonic operation. This would result in a reduction in the effective suction-surface angle which, in turn, would increase the flow capacity of the cascade passage. This effect should be more pronounced on reverse-through-flat-pitch operation than reverse-through-stall-pitch because the blade camber (see Figure 2) is oriented more favorably for the latter with respect to subsonic cascade performance. Note also the increase in efficiency with speed at the +73° blade angle setting.

Data obtained from the traverse probes described in Appendix A were numerically integrated to determine the total tangential momentum of the flow. Using an assumed effective area, a swirl angle was calculated which

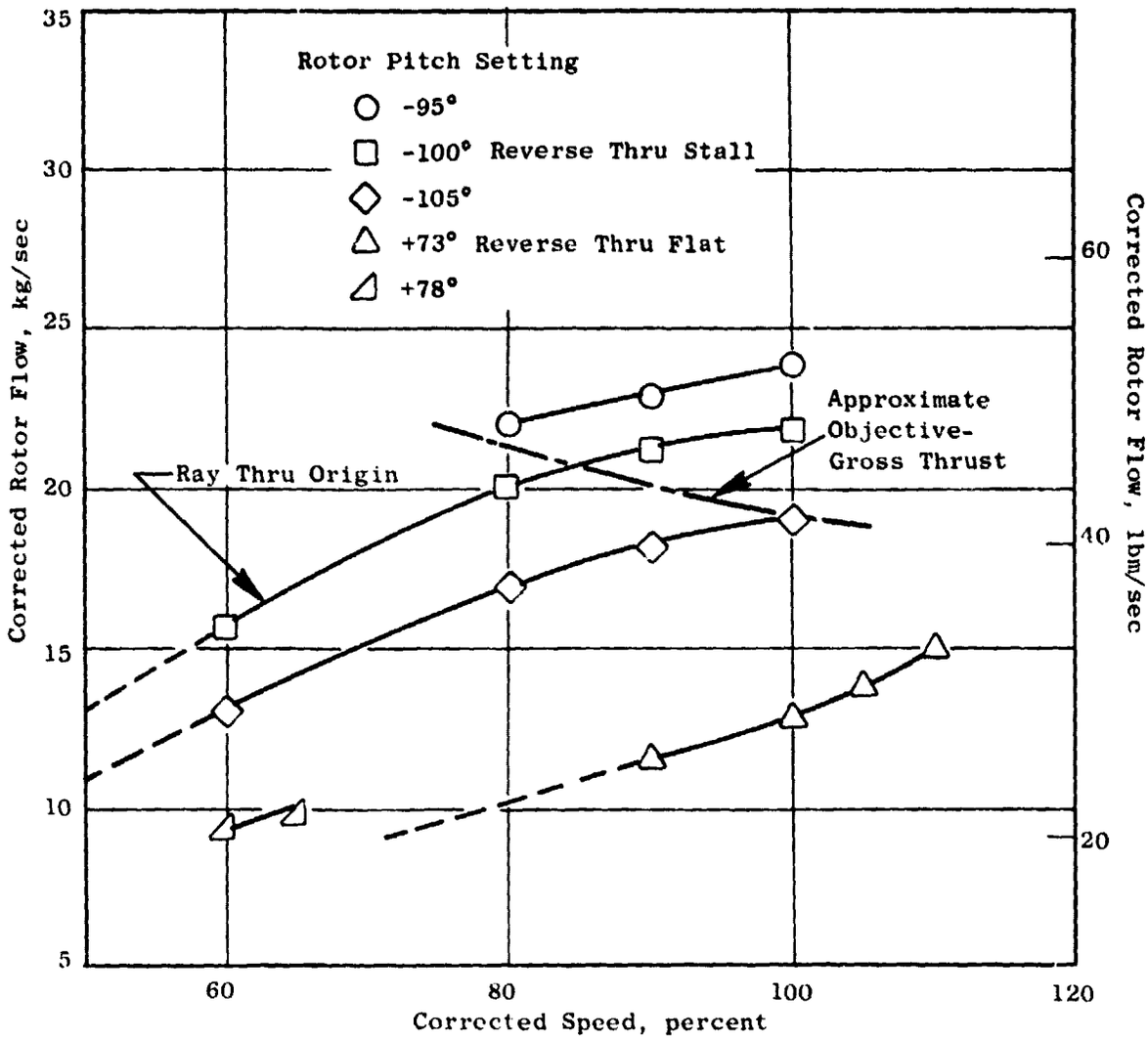

Figure 38. Comparison of Corrected Rotor Air Flow, as a Function of Speed, at Various Rotor Pitch Angle Settings in Reverse Mode.

would yield, on a one-dimensional basis, this tangential momentum while also satisfying continuity. These "average" exit swirl angles, assumed constant over the speed range for each rotor pitch setting, are tabulated in Table II and listed again below:

Rotor Pitch Setting	Average Swirl Angle
-95° through stall	-19.7
-100°	-11.7
-105°	-6.7
+73° through flat pitch	-18.0
+78°	-16.1

The exit swirl angle from the fan has significance since only the axial component of the discharge velocity produces useful thrust. The sign on the swirl angle is such that the absolute velocity vector is turned through the axial direction.

Fan gross reverse thrust, consistent with the overall performance maps and calculated by the method described in Appendix B, is presented in Figure 39. The approximate scaled engine fan gross-thrust objective is also shown. In the reverse-through-stall-pitch direction, the objective reverse thrust can be achieved for each of the three pitch settings tested with the appropriate fan speed. A line of constant gross thrust, equal to the approximate objective, is shown on Figure 38. As the pitch setting is changed from (open) -95° to -105° it is noted that speed increases but flow decreases. The implications of these trends on fan efficiency, core engine total pressure recovery (discussed in the next section), overall engine operation, and on the engine acoustic characteristics must all be examined before the "optimum" pitch setting can be determined.

In the reverse-through-flat-pitch direction, the "measured" reverse thrust is significantly below objective at the +73° pitch setting. Some additional reverse thrust is believed available at a more positive pitch angle setting; however, high blade stresses precluded confirmation at a +78° pitch setting. The mechanical construction of the engine fan rotor is entirely different from that employed in the simulator and, therefore, the mechanical high-stress response of the engine fan rotor will probably be different from that observed in the simulator. This difference may allow higher reverse thrust levels to be achieved during engine tests with the blades turned through flat pitch

7.2 SIMULATED CORE INLET PERFORMANCE IN REVERSE MODE

Measured flow conditions at the transition duct discharge plane are representative of core compressor inlet conditions during UTW engine operation. Total pressure recovery of this flow is of concern since it directly affects the power available to drive the fan. Overall recovery level, P_{25}/P_0, is shown in Figure 40 which shows the measured core total pressure recovery versus total fan inlet flow, the sum of fan rotor flow and core flow, over the range of reverse-thrust blade pitch settings and speeds tested. This recovery could also be displayed against core flow as the independent variable. However, such a display exhibits a great deal more

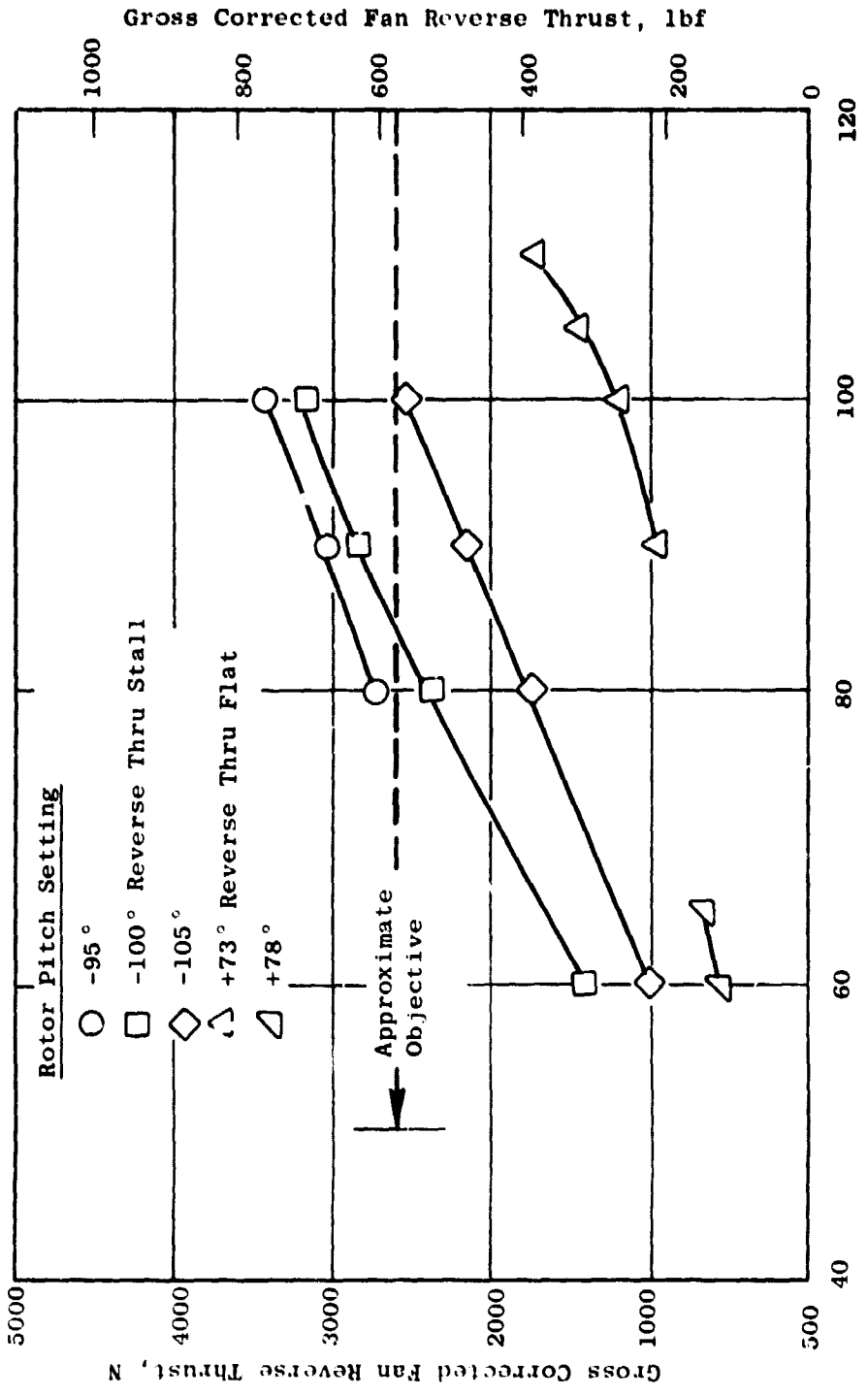

Figure 39. Comparison of Gross Corrected Fan Reverse Thrust, as a Function of Speed, at Various Rotor Pitch Angles in Reverse Mode.

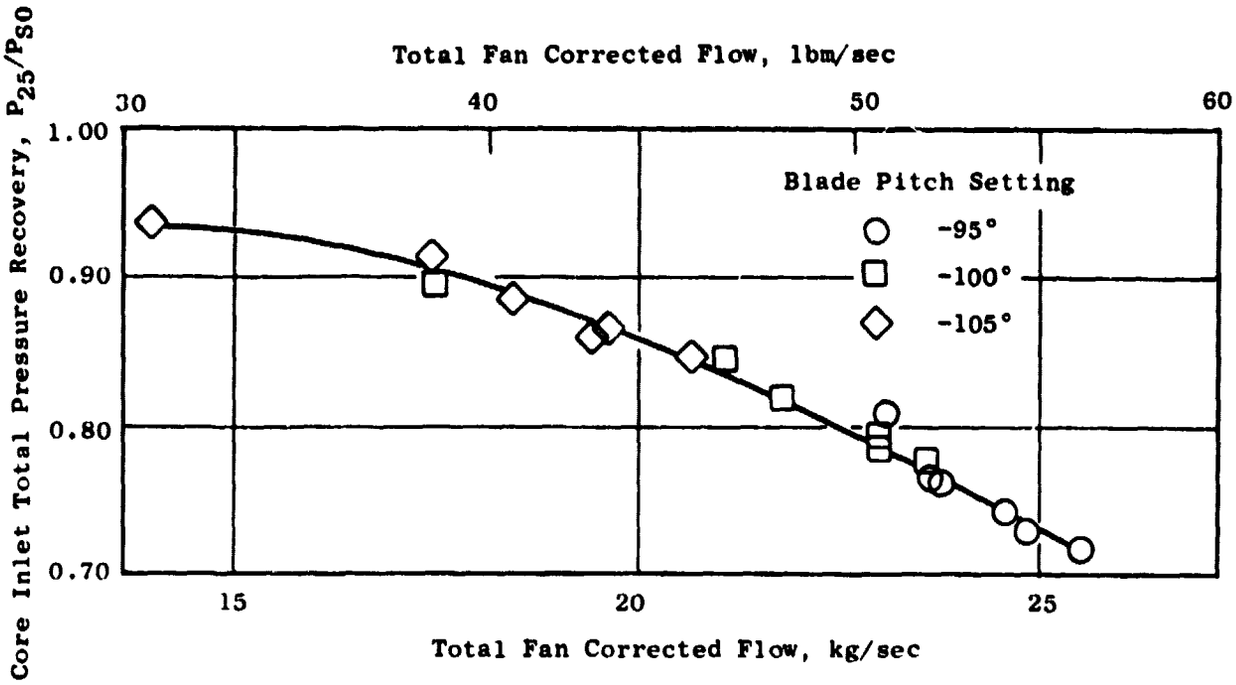

Figure 40. Core Inlet Total Pressure Recovery as a Function of Total Fan Corrected Flow at Various Rotor Pitch Angles in Reverse Mode.

data scatter than is evident in the figure. These observations indicate that the major loss is directly associated with the external momentum of the flow entering the bypass OGVs.

Figure 41 shows some of the more significant pressures which affect the level of core inlet recovery expressed as a pressure difference relative to the dynamic pressure (defined as total minus static pressure) at the bypass OGV ID (vane frame) trailing edge. Thus, unity on the vertical scale is the dynamic pressure of the inlet ID flow in the reverse flow mode of operation. There are three sets of symbols on the figure. The open symbols, in the lower portion of the figure, represent the dynamic pressure of the free-stream flow at the leading edge ID of the vane frame, based on P_sG. This dynamic pressure is higher than that of the inlet ID flow by about 40% due to the counterswirl imparted by the vane frame and radial equilibrium effects. The solid symbols, in the middle portion of the figure, represent the loss in total pressure from vane frame trailing edge to core compressor inlet, $P_{14} - P_{25}$. This total pressure loss is seen to be equivalent to about 1.75 vane frame trailing edge dynamic pressures. Expressed in terms of the vane frame leading edge ID dynamic pressure, the loss in total pressure is 1.75/1.4 or about 1.25 dynamic pressures. The flagged symbols, in the upper portion of the figure, represent the core compressor inlet static pressure, P_{S25}. The difference between the flagged symbols and the solid symbols expresses the dynamic pressure at the simulated compressor inlet, which is seen to increase as total flow increases. Since the intent was to maintain a nearly constant bypass ratio for each reading, it is expected that, as total fan flow increases, the core-flow dynamic pressure should also increase. There does appear to be a trend toward lower core-flow dynamic pressure at total fan flows above 22 kg/sec, but this is considered data scatter, a result of not being able to accurately set the desired bypass ratio.

Obvious methods to improve the reverse-thrust mode core duct recovery are to reduce the dynamic pressure at the leading edge ID of the vane frame or to improve the geometry of the "slot entrance". The constraint on any such change is that the performance of the configuration in the forward mode of operation cannot be significantly penalized. Since no simple change to the geometry could be conceived within these constraints, and since cycle calculations indicate that the engine system can produce the objective 35% reverse thrust even with the low core inlet recovery, it was elected to retain the geometry as designed.

Radial distribution of total pressure measured at plane 25 is shown in Figure 42. Also shown is the circumferential, or ring, average radial profile. The outer two immersions show a region of low total pressure which probably results from the expected flow-separation off the splitter lip. As an indicator of the consistency of the data, the radial distortion of the ring average profile (average pressure minus minimum pressure divided by average pressure) is shown in Figure 43. It is interesting to note that distortion correlates best with core flow but that the recovery correlates best with total flow. In addition to the tip radial distortion pattern, a circumferential distortion in total pressure is also sensed with the transition duct discharge rakes. Rakes 1 and 2 measure equivalent levels of

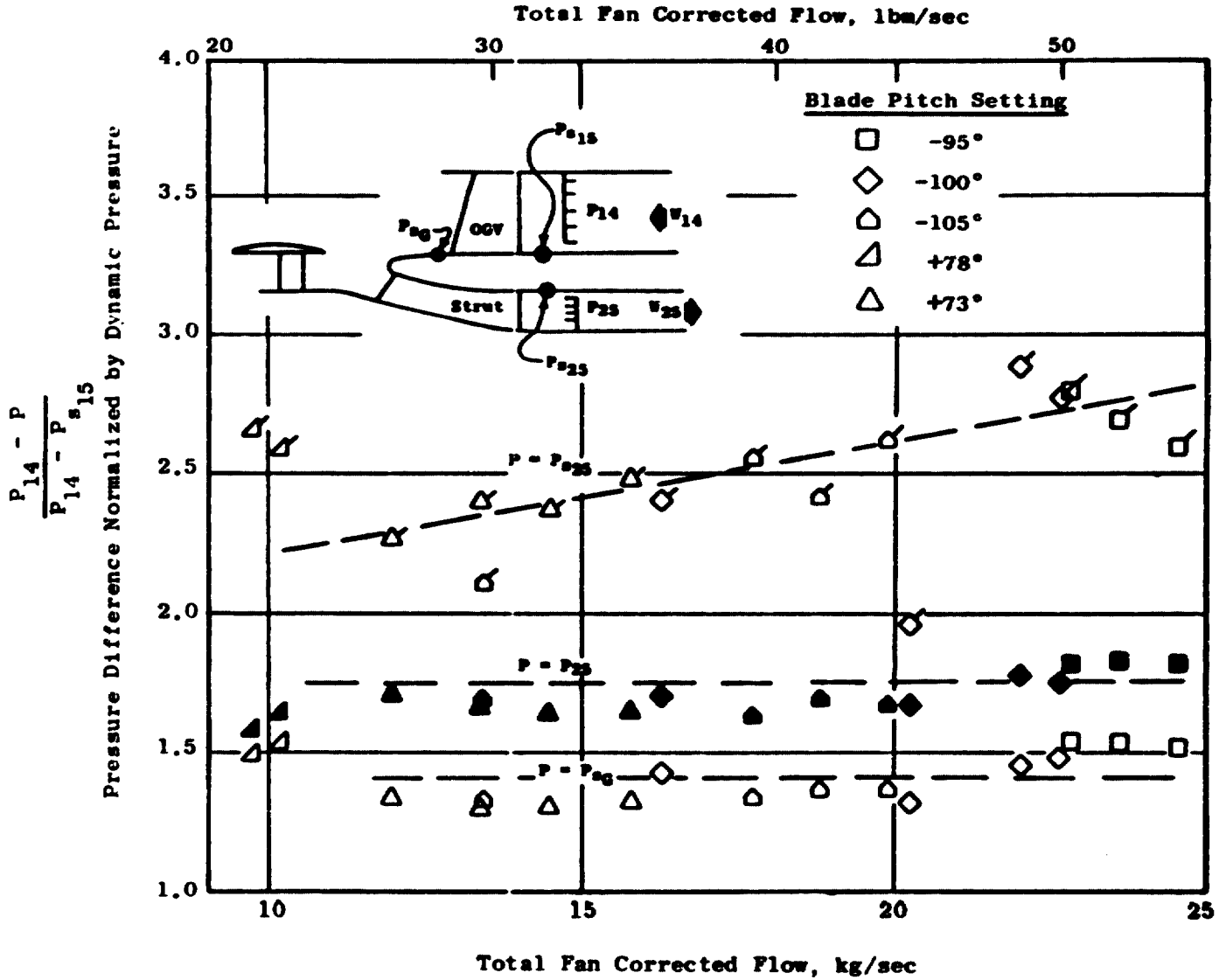

Figure 41. Effect of Blade Pitch Angle Variations on Normalized Pressure Differences at Various Locations in Reverse Mode.

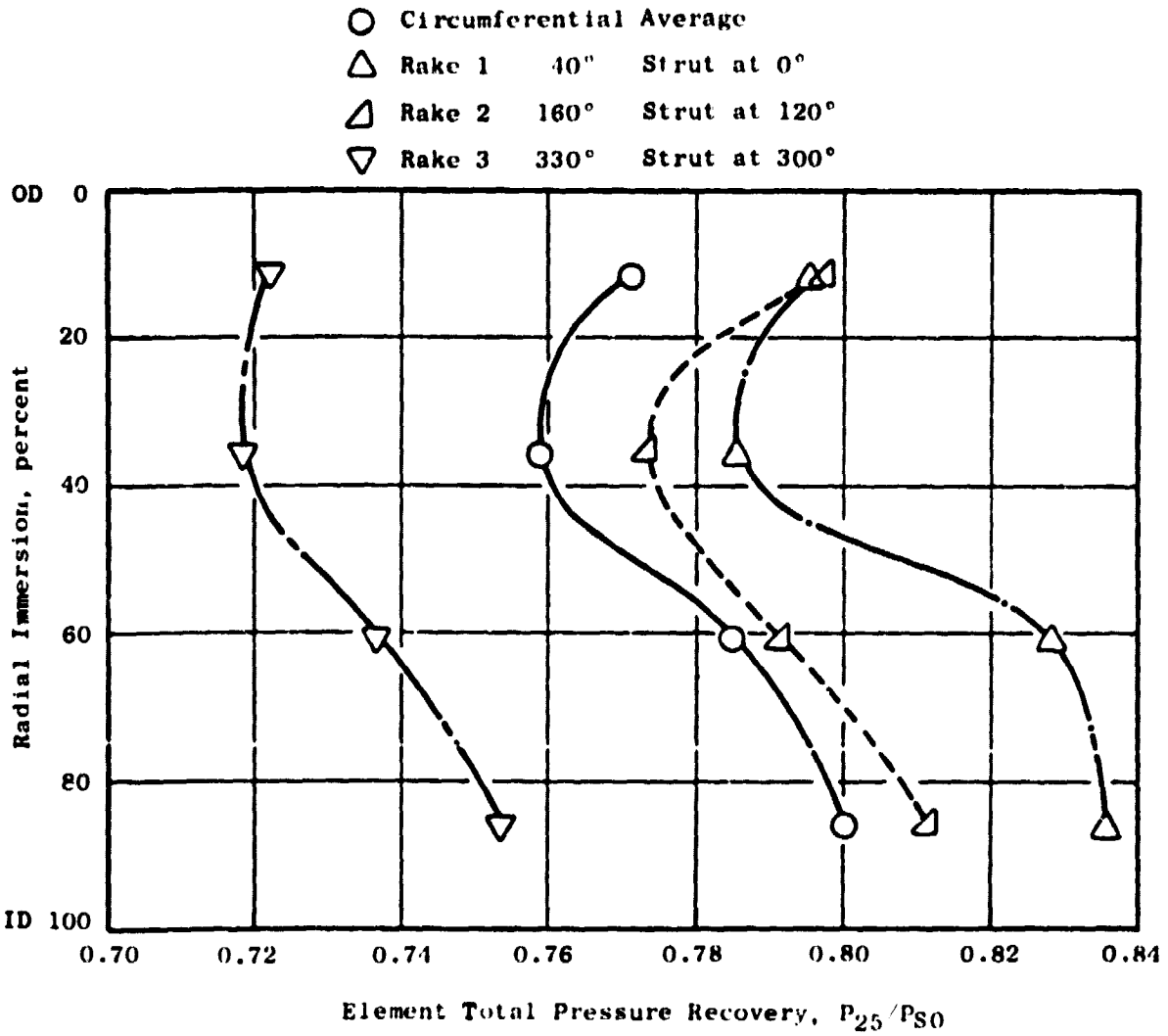

Figure 42. Comparisons of Radial Distributions of Core Inlet Rake Element Total-Pressure Recovery at Various Circumferential Locations with -100° Blade Pitch (Reverse Mode) at 90% Corrected Speed.

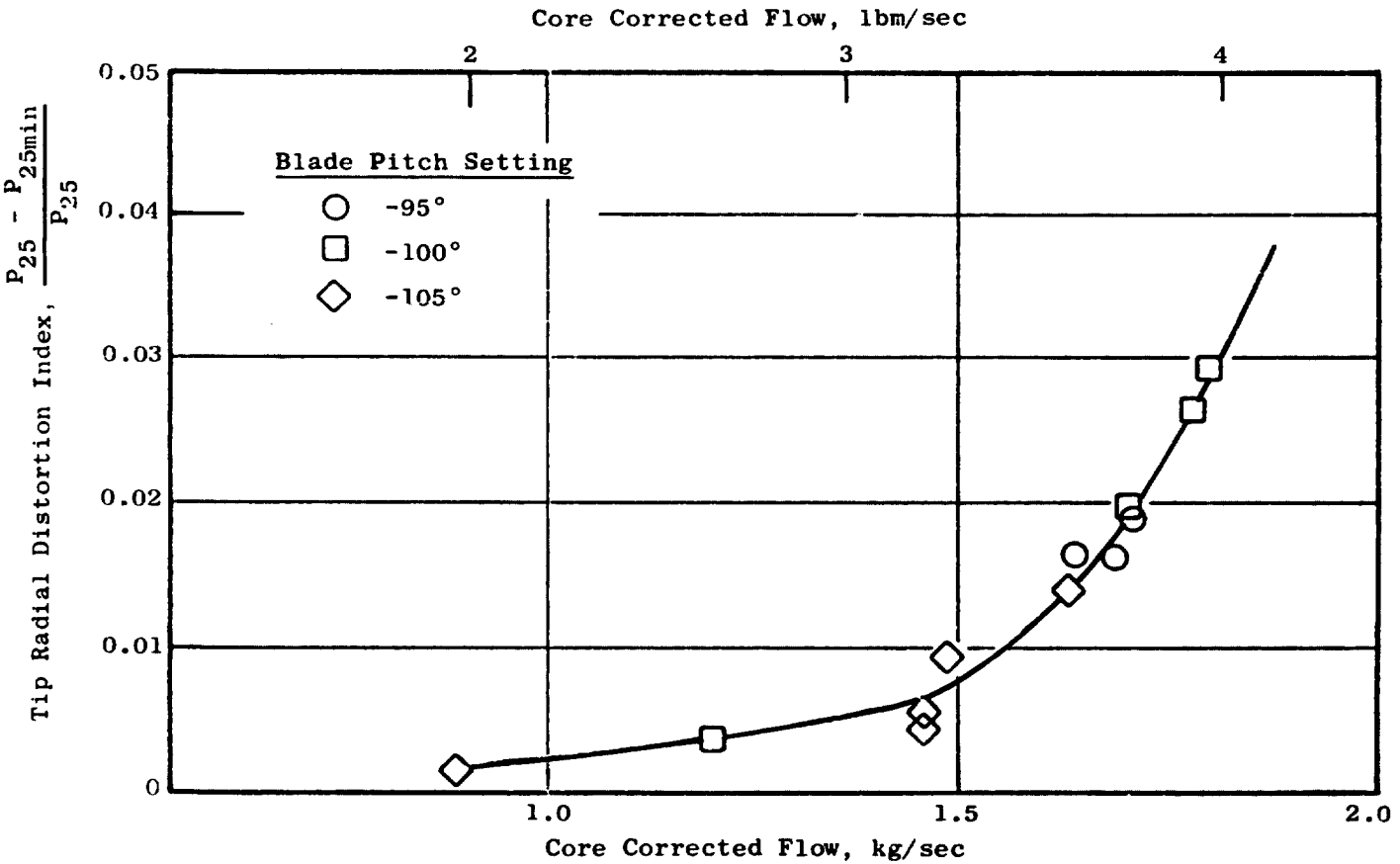

Figure 43. Tip Radial Distortion Index as a Function of Core Corrected Flow at Various Blade Pitch Angles in Reverse Mode.

pressure, but rake 3 reads consistently lower. The transition duct discharge rakes were circumferentially positioned such that rake 3 is midway between struts, while rakes 1 and 2 are one-third of the strut spacing from a strut in a counterclockwise direction aft looking forward. Due to the swirl imparted by the bypass OGVs, the core struts operate at a large negative incidence angle. Since rake 3 is circumferentially closer to this separated surface, it is likely that the separation region has a greater influence on its readings than on the readings of rakes 1 and 2. Flow calculations at the transition duct discharge plane, when compared to the core duct orifice measured flow, indicate an effective flow area 20% smaller than the physical area. This result tends to confirm the hypothesis of large circumferential separation regions.

7.3 REVERSE THRUST MODE STARTING PHENOMENON

The UTW 50.8 cm (20 in.) Simulator Fan employed adjustable pitch blades that were mechanically resetable at zero fan speed. During the reverse thrust mode of testing, two distinctly different flow regimes were observed: (1) a fully-stalled regime that was generally, but not always, present with initiation of rotor rotation, and (2) the "normal" type of flow pattern associated with operation at useful reverse fan thrust. In all cases where the fully-stalled regime was present with initiation of rotor rotation, an abrupt transition to the "normal" type of flow pattern was observed at a fan speed that appeared to depend upon the vehicle configuration and the other test variables. Once the "normal" type of flow pattern was established, there were no observed transitions back to the fully-stalled engine regime - even during shutdown.

Operating characteristics of the fan in the fully-stalled regime are of little interest since the reverse thrust produced by the fan is very small. This is so because the flow exited from the inlet more or less radially outward and, in addition, the net flow through the fan was very small. Furthermore, except for the -95° (open) blade angle, the fully-stalled regime was observed only at low fan speed. The presence of the fully-stalled regime at initiation of rotor rotation and the abrupt transition to the "normal" type of flow pattern is intriguing. However, since an engine will go into the reverse thrust mode by varying pitch angle at approximately constant speed as contrasted to the fixed-pitch, variable-speed operation of the simulator fan, a detailed study of the abrupt transition phenomenon observed on the simulator could not be justified. Several observations were piggybacked and will be noted for completeness.

Physical indicators of the two flow regimes were obtained from a very crude tuft arrangement at the fan inlet (where the flow discharges from the fan when in the "normal" reverse flow pattern) and, at higher speeds, from the rotor stress-signal characteristics. The fully-stalled regime was characterized by backflow into the inlet through a large central portion, perhaps 75% of the inlet area, and out of the inlet along the walls. The annular ring of flow out of the inlet remained attached to the inlet lip until it

approximately reached the inlet highlight where it separated and went more or less radially outward. For the "normal" type of reverse flow pattern there was no evidence of ambient air backflowing into the fan inlet. Flow out of the inlet separated from the walls in the near-vicinity of the throat and the discharge from the inlet was primarily axial in direction with very little radial component of velocity.

Initiation of rotor flow during acceleration was observed on approximately 30 occasions. The vehicle configuration and the fan speed at which the abrupt transition from the fully-stalled regime to the "normal" reverse flow regime occurred are given in Table III. For a given vehicle configuration, the two test variables, other than speed, were bypass discharge valve setting and core flow. The bypass discharge valve is not believed to have a significant impact on the abrupt transition since the flow through the valve, for the fully-stalled regime, was small and recovery across the valve should therefore be near unity for the settings employed. The core flow does have an impact on the abrupt transition as evidenced most notably by observations 11 and 24 through 27, versus observations 1 through 10. The settings employed on the core flow were purely conjectured. Ideally, they should have been set to simulate the engine core flow at the abrupt-transition fan speed. However, since the abrupt-transition fan speed was not known, and no cycle information was available to estimate the engine characteristics with the fan in the fully stalled regime, no other recourse was available.

Further observations of this starting phenomenon, discussed from an aeromechanical point of view, and an illustration of the stall transition regime (Figure 60) are presented in Appendix C.

Table III. Transition from Fully Stalled Regime to Normal Flow Regime During Initial Acceration with Reverse Blade Angles.

Observation[1]	Blade Pitch Setting	Discharge Valve Set.	Core Flow	Fan Speed at Abrupt Transition, rpm	Comments
	Rev. Thru Feather				
1	(Open)	Open	No	3600	Flow visualization checkout
2	-95°	Open	No	4300	Flow visualization checkout
3	-95°	Open	No	0	Flow visualization checkout
4	-95°	Open	No	?	Flow visualization checkout
5	-95°	Open	No	3600	Flow visualization checkout
6	-95°	Open	No	4300	Flow visualization checkout
7	-95°	Open	Yes	>5000	Flow visualization checkout
8	-95°	Open	No	5870	Flow visualization checkout
9	-95°	Open[2]	No	7600	
10	-95°	6.37	No	5600	
11	-95°	6.37	1.74	9200	
12	-100°	6.37	Yes	5000	
13	-105°	6.37	Yes	0	
14	-105°	6.37	Yes	3700	
	Rev. Thru Flat Pitch				
15	(Closed) +78°	6.37	Yes	2300	High Mach Inlet
16	+73°	6.37	Yes	2090	
17	+73°	6.37	Yes	1980	
	Rev. Thru Feather				
18	(Open)-100°	6.37	1.5	2600	
19	-100°	6.37	1.5	2500	
20	-100°	6.37	1.5	2400	
21	-100°	6.37	1.5	2100	
22	-100°	6.37	2.1	3280	
23	-100°	6.37	1.5	2650	
24	-95°	6.37	2.3[3]	9000	
25	-95°	6.37	2.3[3]	9000	
26	-95°	6.37	2.3[3]	9000	
27	-95°	6.37	2.2	7300	
28	-105°	6.37	3.6	2870	
29	-105°	6.37	3.6	3175	
30	-100°	6.37	3.6	0	
31	-100°	6.37	3.6	2500	Low Mach Inlet - Acoustic Tests Only
32	(Open)-100°	6.37	3.7	<1000	

Aero Design Fan Speed = 11,500 rpm

(1) Observations 1 through 29 Incorporated High Mach Inlet
Observations 30 through 32 Incorporated Low Mach Inlet (Acoustic Tests Only)

(2) Set at 6.0 initially, opened fully at 6000 rpm

(3) Core flow initially set at 3.5, at 9000 rpm core flow reduced till transition occurred

SECTION 8.0

CONCLUSIONS

From the aerodynamic test results of the 50.8 cm (20 inch) scale model of the QCSEE UTW fan and inlet reported herein, several conclusions relating to the operation of the QCSEE UTW engine may be drawn.

In the forward thrust mode, the design intent flow and pressure ratio were not achieved at nominal ($\beta_P = 0°$) rotor pitch, but the variability of the rotor blades and bypass stream exhaust nozzle in the engine allows for specific objectives of flow and pressure ratio to be attained. Therefore, a redesign of the fan rotor to achieve design intent at nominal blade angle cannot be justified. From the standpoint of best aerodynamic performance, it is desirable to operate the fan at combinations of high speed and closed blade pitch settings; however, mechanical limitations and acoustic requirements may limit the extent to which this is done.

Although the bellmouth inlet was used for most of the forward performance testing, sufficient data were taken with the accelerating inlet to determine that it has no severe detrimental effects on the operating characteristics of the fan. The operating limits of the fan near stall met or exceeded the objectives, indicating sufficient stall margin for all engine operating conditions. Testing with an imposed tip radial distortion showed fan sensitivity consistent with the results observed on other fans. The circumferential flow distortions produced by the nonaxisymmetric vane frame were small enough in magnitude so as to have no significant impact upon the fan rotor characteristics.

Although the aerodynamics of the engine fan were accurately modeled with the 50.8 cm (20 inch) scale model, there are several aeromechanical and geometric differences between the two that should be noted. The scale model rotor blades, made of titanium, are individually adjustable at rest, while the engine blades, made of a composite material, are intended to be all simultaneously fully reversible at speed. This characteristic may result in differences in the transition phenomenon of the reverse mode operation between scale model and engine. The fan discharge duct geometry in both the core and bypass regions differs slightly due to limitations imposed by the scale model test facility. However, these flowpath differences should not influence the forward thrust operation of the fan rotor or outlet guide vane rows. Fan hub (core) flow is determined by the system cycle balance during engine operation, but had to be independently controlled for the scale model. The cycle analysis predictions of engine bypass ratio were simulated; and to the extent that these predictions are accurate, the hub performance reported for the scale model may be judged representative of the full-size fan.

In the reverse thrust mode of operation, the scale model demonstrated that thrust objectives can be achieved with the rotor blades reversed through stall pitch, but probably not when reversed through flat pitch. However, due to the different mechanical construction of the engine fan rotor, different stress-response characteristics may permit engine operation to higher thrust levels when reversed through flat pitch. Core duct recovery, though slightly lower than predicted, will not prevent the fan from producing the objective reverse thrust. Any improvements made to the geometry of the "slot entrance" for better core duct recovery would probably penalize the performance of the configuration in the forward mode. Therefore, a redesign was not considered justified.

APPENDIX A

UTW 50.8 cm (20 inch) SIMULATOR FAN AERO TEST INSTRUMENTATION AND DATA REDUCTION

INTRODUCTION

A portion of the planned test program for the QCSEE UTW Simulator at CR&DC was allotted to fan aerodynamic performance tests. Basic aerodynamic test objectives were:

- To verify the aerodynamic performance adequacy of the fan design prior to incorporation into the UTW engine configuration.
- To isolate problem areas, if they exist, and provide adequate test information for their resolution.
- To provide data for updating the fan performance representation in the cycle deck prior to UTW engine operation.

Specific tasks accomplished in support of these objectives were:

- Obtained base operating maps of the bypass and core portions of the fan at several conventional forward rotor pitch settings.
- Determined the effect of off-design bypass ratio on performance.
- Determined degree of circumferential flow distortion induced by nonaxisymmetric bypass OGV and pylon configuration.
- Obtained fan performance in a high Mach inlet environment.
- Determined reverse thrust performance through feather (stall) and flat pitch blade setting angles.
- Obtained core duct total pressure recovery and radial distortion characteristics during reverse pitch operation.

Instrumentatior and data reduction were coordinated to stay within the following constraints:

- Scannivalve limitations (96 ports - 8 allotted to facility and reference pressures leaving a total of 88 for fan aero).
- Fan aero temperatures limited to 44.
- Storage/computational limits for the Hewlett Packard data acquisition and reduction system.

INSTRUMENTATION

The fan aero forward-mode instrumentation is shown in Figure 44. Axial and circumferential locations of the bypass OGV outlet rake instrumentation are shown in Figure 46, an unwrapped section of the bypass OGVs and pylon.

Fan aero reverse-mode instrumentation is shown in Figure 45 with the reverse configuration.

Specific instrumentation is described below.

Radial Rakes

Three fixed radial rakes with 5 combination total-pressure, total-temperature elements each were provided for use with both the inlet bellmouth and high Mach inlets. For reverse pitch testing, these rakes were reversed and moved to the inlet throat.

Three fixed radial rakes with 5 combination total-pressure, total-temperature elements each were located in the bypass duct just downstream of the bypass OGV trailing edge, as shown in Figure 46. Circumferentially, these rakes were positioned behind the open 2 vane set, the nominal set, and the closed 2 set. Provisions were made for alternate locations behind the open 1 vane set, the open 1-nominal vane passage, the nominal-closed 1 vane passage, and the closed 1-closed 2 vane passage. In all cases, these rakes were positioned at vane midpassages to attempt to avoid vane wakes. These rakes were reversed for reverse pitch testing and measured the inlet flow field at the bypass OGV trailing edge.

The core duct contained three radial rakes of 4 total pressure and temperature elements each. All radial rakes had Keil-type elements designed to accept flow angularity well beyond that expected for test conditions. Table IV lists element immersions for the different radial rakes.

Traverse Arc Rakes

Two radially-traversing arc rakes with 13 combination total-pressure, total-temperature elements each were available for traversing the bypass duct approximately 3/4 chord downstream of the bypass OGV trailing edge, as shown in Figure 46. The prime circumferential locations were behind the open 2 vane set and the closed 1 vane set. Alternate locations were provided behind the open 2 - open 1 vane passage and behind the closed 2 vane set. Traverse of the nominal vane set was precluded due to vehicle-floor clearance considerations. Arc rake immersions are listed in Table V for the forward mode only.

FULLOUT FRAME 1

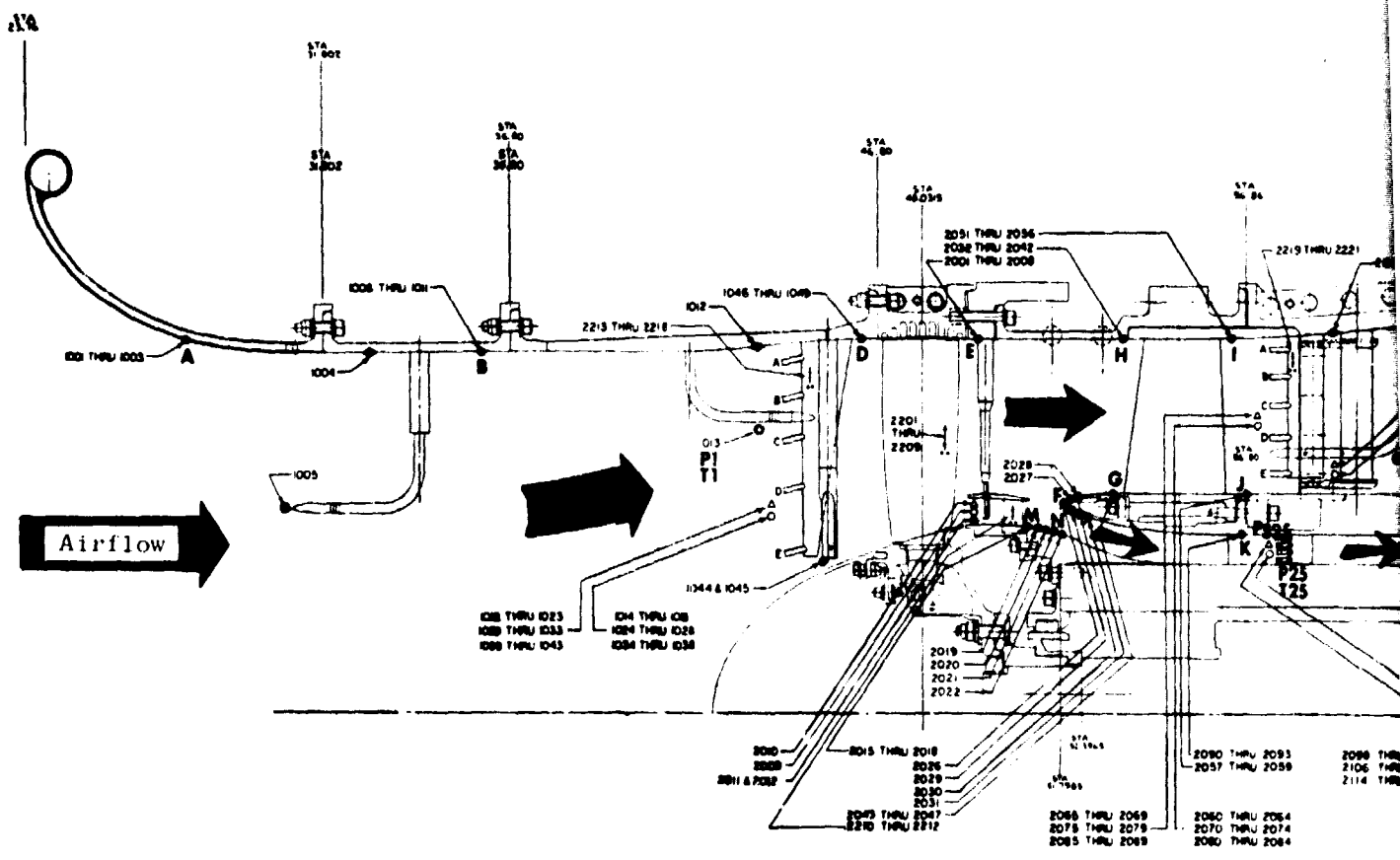

Figure 44. Forward Mode Test

FOLDOUT FRAME 2

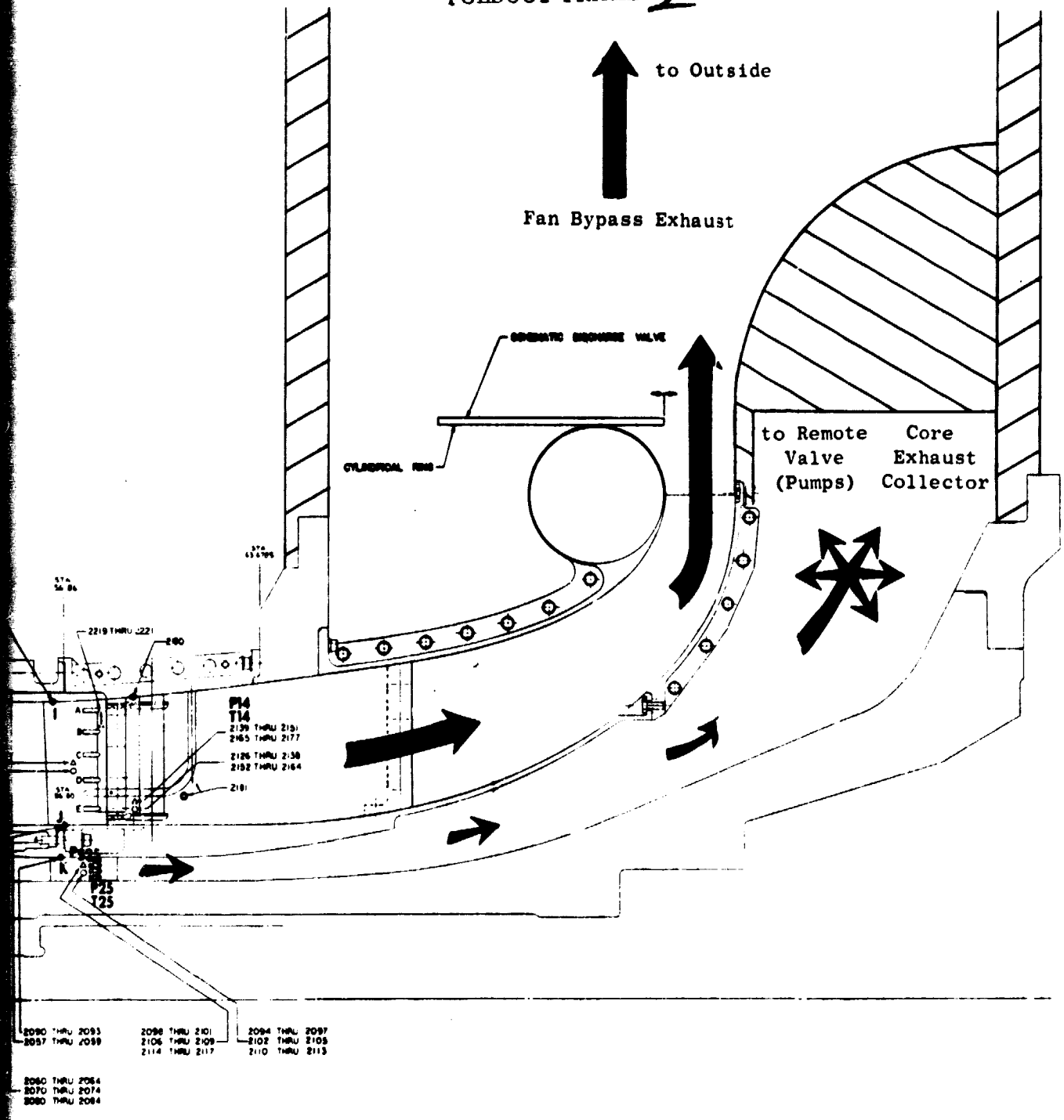

rward Mode Test Configuration.

FOLDOUT FRAME 3

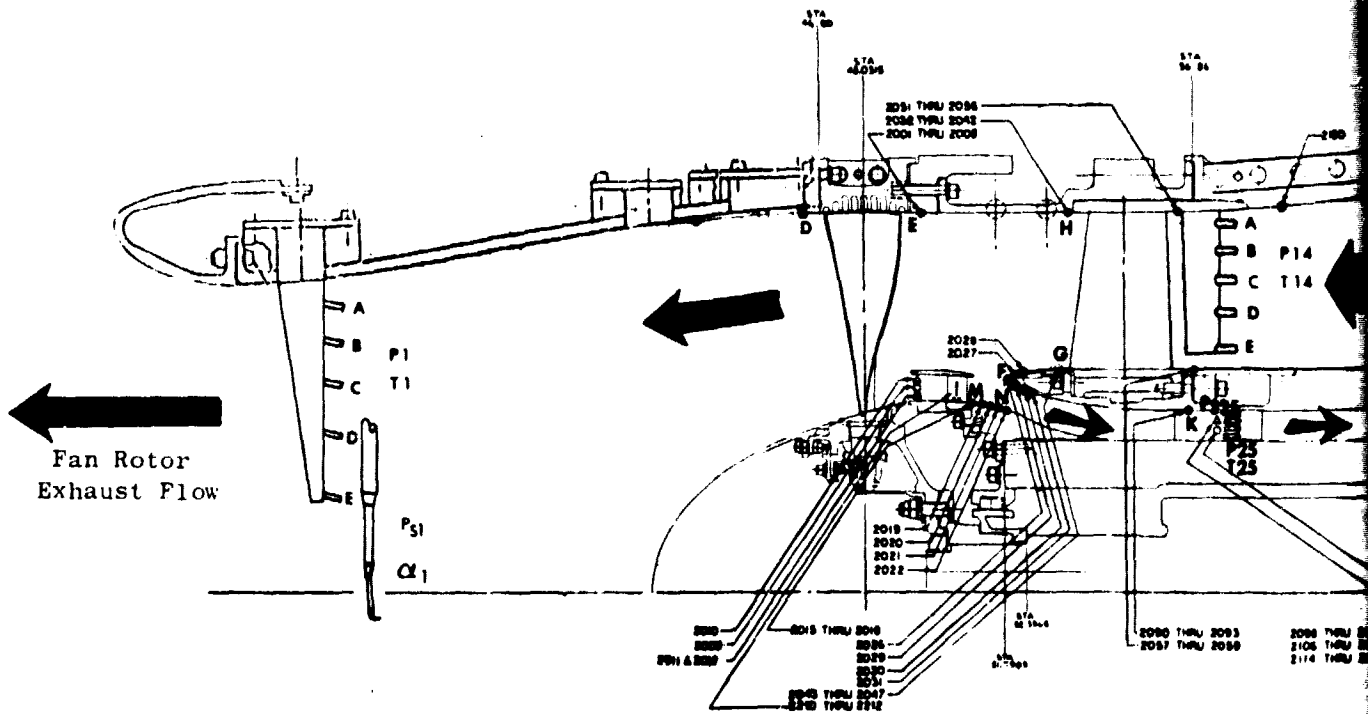

Figure 45. Reverse Mode Test Co

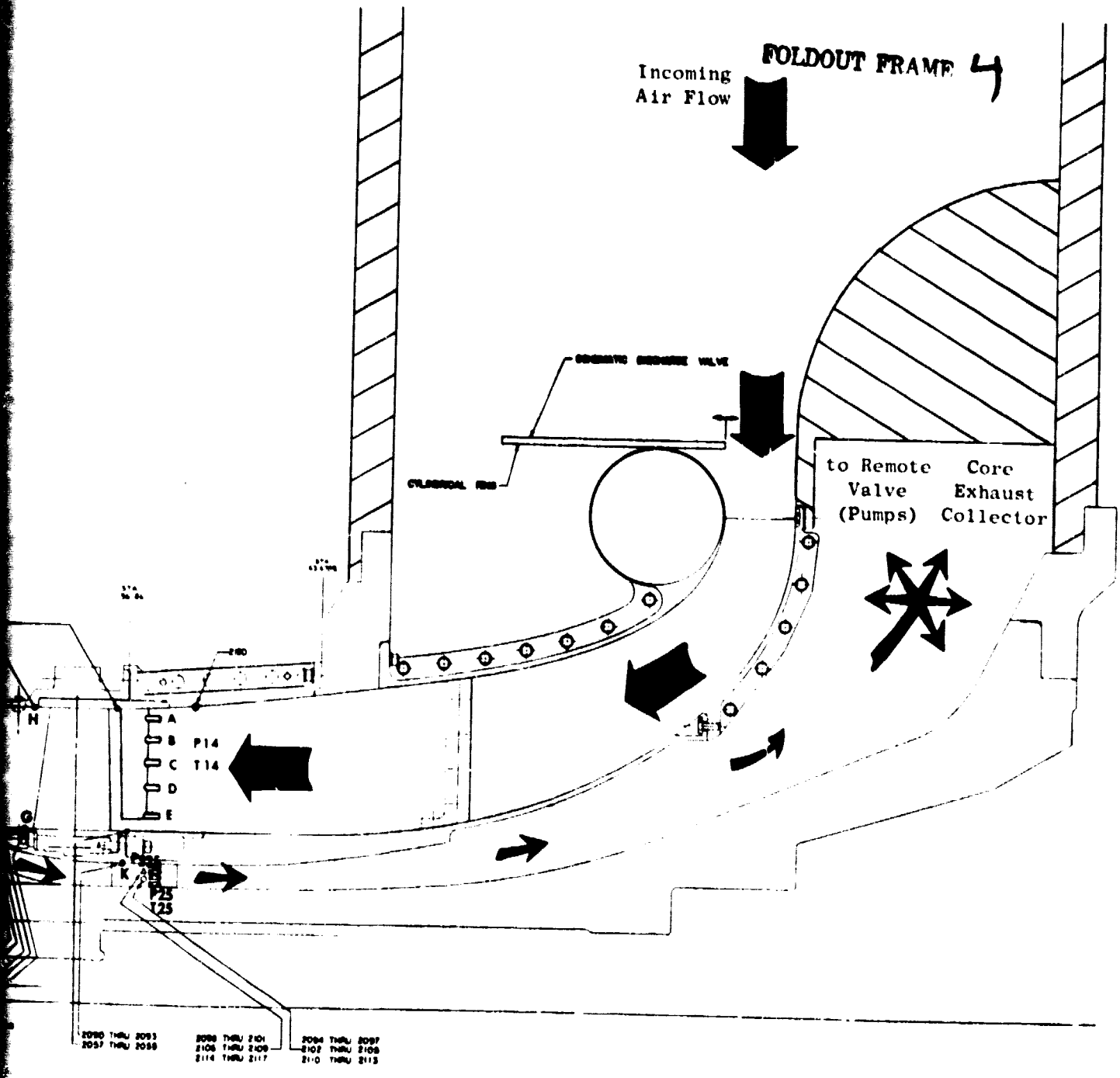

Reverse Mode Test Configuration.

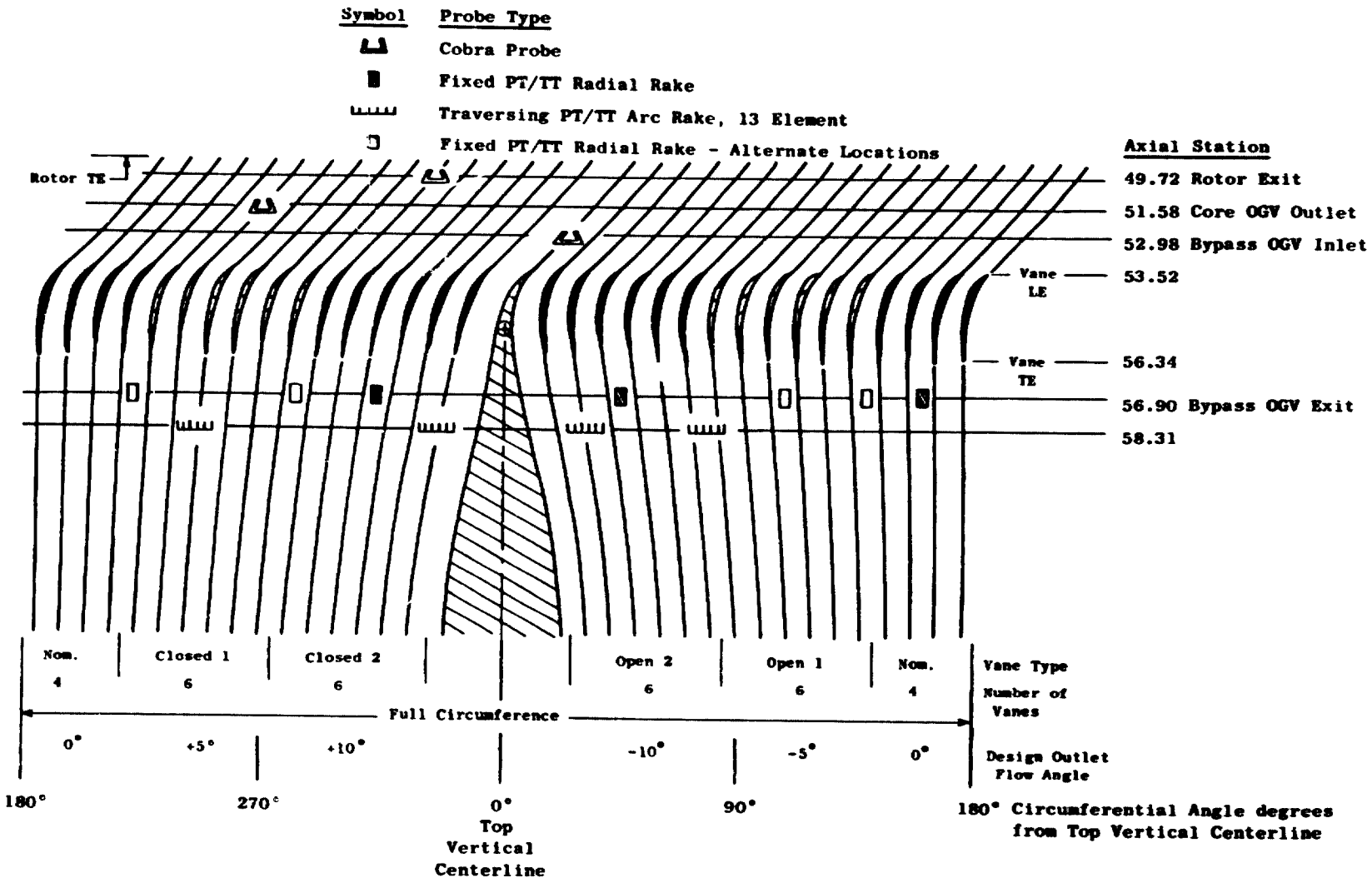

Figure 46. Vane Frame Instrumentation Locations, Unwrapped Section of Fan Bypass OGVs at Inner Wall.

Table IV. Radial Rake Immersions.

Inlet Rakes								
	Forward Pitch				Reverse Pitch			
	R		Immersion		R		Immersion	
Element	cm	in.	cm	in.	cm	in.	cm	in.
A	23.90	9.41	1.14	0.45	20.55	8.09	0.48	0.19
B	21.39	8.42	3.66	1.44	18.06	7.11	2.97	1.17
C	18.57	7.31	6.48	2.55	15.24	6.00	5.79	2.28
D	15.21	5.99	9.83	3.87	11.89	4.68	9.14	3.60
E	10.90	4.29	14.15	5.57	7.57	2.98	13.46	5.30

Bypass Duct Rakes					
	R			Immersion	
Element	cm	in.	% Immersion	cm	in.
A	24.69	9.72	0.081	0.86	0.34
B	22.89	9.01	0.251	2.67	1.05
C	20.93	8.24	0.435	4.62	1.82
D	18.75	7.38	0.641	6.81	2.68
E	16.31	6.42	0.870	9.25	3.64

Core Duct Rakes				
	R		Immersion	
Element	cm	in.	cm	in.
A	11.94	4.70	0.22	0.09
B	11.46	4.51	0.71	0.28
C	10.95	4.31	1.22	0.48
D	10.44	4.11	1.73	0.68

Table V. Arc Rake and Cobra/Wedge Probe Immersions.

Arc Rake Immersions																	
	R		Immersion		Elements Not Included in Rake Average												
Position	cm	in.	cm	in.	A	B	C	D	E	F	G	H	I	J	K	L	M
A	25.031	9.855	0.610	0.240	X	X										X	X
B	23.759	9.354	1.882	0.741	X	X										X	X
C	22.410	8.823	3.230	1.272	X	X	X									X	X
D	20.978	8.259	4.663	1.836	X	X	X									X	X
E	19.434	7.651	6.208	2.444													
F	17.760	6.992	7.882	3.103	X												
G	15.913	6.265	9.728	3.830	X												X
R = Radius of arc rake element G Immersion is immersion of element G (from outer wall)																	

Cobra and Wedge Probe Immersions at Inlet Throat for Reverse Mode				
	R		Immersion	
Position	cm	in.	cm	in.
A	20.577	8.101	0.533	0.210
B	19.461	7.662	1.648	0.649
C	18.283	7.198	2.827	1.113
D	17.021	6.701	4.089	1.610
E	15.657	6.164	5.453	2.147
F	14.161	5.575	6.949	2.736
G	12.489	4.917	8.621	3.394
H	7.140	2.811	13.970	5.500

C-2

Traverse Probes

Provisions for cobra-probe radial traverses were incorporated in the vehicle at three axial positions downstream of the rotor as shown in Figure 46: (1) immediately downstream (temporary hole in the island to allow traverse of rotor hub discharge), (2) downstream of the core OGV for investigation of the island trailing edge vortex and stator discharge conditions, and (3) at the inlet of the bypass OGV.

In reverse pitch operation, a cobra and a wedge probe simultaneously traversed the throat region of the accelerating inlet to provide data for reverse thrust and exhaust swirl determination. Immersions for reverse pitch testing are listed in Table V.

Static Pressures

Static pressure instrumentation was provided for four purposes: determine airflow, assess circumferential flow distortion, determine axial and circumferential static pressure profiles, and monitor vehicle operation during acoustic testing with rakes removed.

Static taps were located in the inlet, bypass duct exit, and core duct for airflow determination.

Information on the circumferential flow distortion induced by the non-axisymmetric bypass OGV was provided by rings of static taps upstream and downstream of the bypass OGV. The statics were placed circumferentially to indicate vane-set-to-vane-set variation and distortion between adjacent vane sets. Forward propagation of the effects of a nonsymmetric flow field can be detected by the static tap rings forward and aft of the rotor. A ring of static taps was also located on the ID surface downstream of the core OGV.

Static taps were located to measure axial profiles on the splitter nose and along the hub of the transition duct.

DATA REDUCTION

Data reduction procedures were specified for seven separate data modes described below:

Mode 1	-	Forward pitch test mode with all fixed radial rakes installed.
Mode 1 (Mod)	-	Forward pitch radial traverse mode for cobra and/or wedge probes.
Mode 2	-	Forward pitch test mode for radially traversing bypass OGV with both arc rakes simultaneously.

Mode 4 - Reverse pitch test mode with all fixed radial rakes installed.

Mode 5 - Reverse pitch test mode for simultaneous cobra and wedge probe radial traverse of inlet throat.

Mode 6 - Forward pitch test mode for operating-line monitoring for acoustic testing with fixed rakes removed.

Mode 7 - Reverse pitch test mode for monitoring vehicle acoustic testing.

In addition, a time-share program was specified for summary calculations of the traverse immersion data of Mode 2.

Equations in the data reduction programs conformed to perfect gas relationships. Real gas effects were accounted for through:

- Gamma (γ) variation with temperature and humidity
- Gas constant (R) variation with humidity
- Cp variation with temperature and humidity

These variations were defined for consistency with in-house programs that utilize enthalpy tables.

FORWARD DATA MODES 1 AND 2

In general, flow rate is calculated from the following equation:

$$W = \frac{PA}{\sqrt{T}} \sqrt{\frac{g\gamma_m}{R_m}} \left\{ \left[\left(\frac{P_s}{P} \right)^{\frac{1-\gamma_m}{\gamma_m}} - 1 \right] \left[\frac{2}{\gamma_m - 1} \right] \right\}^{1/2} \left(\frac{P_s}{P} \right)^{\frac{\gamma_m + 1}{2\gamma_m}} \quad (1)$$

Fan inlet flow is determined from the average pressure (P1 in Figure 44) and temperature (T1) measured by the three fixed radial rakes, the average static pressure measured at the bellmouth wall (P_sB), and an adjustment made to the static-to-total pressure ratio to account for an effective inlet area coefficient:

$$\frac{P_s}{P} = (1-K) \frac{P_sB}{P1} + K \quad (2)$$

It was assumed that K = 0.024, which is equivalent to an effective area coefficient of 0.99 at design flow conditions.

Core duct physical flow rate is accurately measured with an orifice located in the core suction system. Core duct flow is also determined from the average pressure (P25) and temperature (T25) measured by the three fixed radial rakes at each immersion, and is compared to the orifice flow for consistency. Similarly, the bypass duct flow is calculated from average immersion pressures (P14) and temperatures (T14) measured by the three 5-element radial rakes, and is compared to the difference between fan inlet flow and inlet-corrected core orifice flow. Static pressures used in both the core duct flow and bypass duct flow computations are averages of the wall statics (P_SK and P_SI) and assume these values to be constant across the ducts.

Fan rotor adiabatic efficiencies for both bypass and fan hub (core) are computed from mass-averaged enthalpies (actual and ideal) determined from radial rake measurements. An independent check on the rotor bypass efficiency was taken using the three highest-reading elements on each traversing arc rake. Overall bypass stream stage efficiency is determined from mass-averaged enthalpies of certain specified elements (see Table V) on the traversing arc rakes.

REVERSE DATA MODES 4 AND 5

Flow entering the vehicle is determined at the bypass OGV trailing edge plane from the average pressure (P14 in Figure 45) and temperature (T14) measured by the three fixed radial rakes, the average static pressure measured at the inner wall (P_SJ), and an adjustment made to the static-to-total pressure ratio to account for an effective inlet area coefficient:

$$\frac{P_s}{P} = (1-K)\frac{P_sJ}{P14} + K \qquad (3)$$

It was assumed that K = 0.073, which is equivalent to a 0.97 effective area coefficient at a Mach number of 0.5. Both flow and fan speed are corrected by δ_{14} and θ_{14}. Core duct flow is determined exactly as in the forward mode.

Measurements of pressure (P1) and temperature (T1) in the fan inlet throat and the downstream test cell pressure, PSO, are used to calculate efficiency, flow rate, and thrust at each immersion. Overall stage values of pressure, temperature, and efficiency are determined by mass-averaging the immersion enthalpies. Traverse measurements of total pressure, static pressure, and flow angle are used to accurately determine the axial velocity profile at the fan inlet throat, from which the axial component of thrust is calculated. From static pressure measurements along the inlet lip, the pressure forces acting on the lip area are accounted for in the overall thrust calculation. Having both fixed-rake data and traverse-probe data at the same plane provided an opportunity to check the consistency of the data and the

validity of assumptions concerning the discharge flow pattern. Test data in the reverse thrust mode were ultimately expressed in terms of a universal stage characteristic, discussed in detail in Reference 2.

APPENDIX B

AERO PERFORMANCE MAP DEFINITION FOR UTW ENGINE

FORWARD PITCH-BYPASS FLOW AERO MAP

The procedure adopted for aero map definition for UTW engine cycle analysis was to assume radial rake (Mode 1) data for rotor performance, to which bypass OGV losses were added to deduce stage performance. This was done because fixed radial rake (Mode 1) data were available over the entire range of simulator aero test conditions. Three steps were required to prepare the simulator test data for final map specification:

- Adjustment of radial rake (Mode 1) data for known defects.
- Perturbation of radial rake (Mode 1) data to include arc-rake measured bypass OGV losses.
- Reconciliation of temperature measurement differences.

The radial rake (Mode 1) data were believed to be in error from two sources; a low-reading bypass rake pressure element (third rake, inner immersion), and an inlet rake wake shadow impingement on the third bypass rake. Both of these problems are illustrated in Figure 47, which shows rotor pressure rise measured by rake 3 ratioed to the average of the pressure rise measured by rakes 1 and 2 versus discharge valve closure setting for the blade pitch angles tested. The top half of Figure 47 shows the ratio for the outer four immersions to illustrate the effect of removing the inlet rake, and the bottom half shows the ratio for the inner immersion to indicate the low reading element (note the scale difference). Since the inlet rake wake shadow was a mass transport phenomenon, its effect on the fixed location downstream pressure measurement was expected to be related to rotor exit swirl. This was observed in Figure 47, which showed the third rake pressure deficiency to increase with increasing rotor exit swirl through opening the discharge valve or opening the rotor blade. At the + 5° rotor pitch, inlet rake 3 was removed, and the pressure level measured by the third bypass rake increased to a level comparable to that measured by the other two bypass rakes.

The low-reading inner element of bypass rake 3 is more difficult to explain. Bypass rakes 2 and 3 were interchanged with the results illustrated in Figure 48. For the inner immersion, rake 3 sensed a pressure level comparable to rake 2 in the 166° location, and rake 2 sensed a pressure level considerably higher than that measured by rake 3 in the 314° location. In other words, the only combination of rake and location which resulted in the low pressure measurement was rake 3 in location 3. Arc rake results show a very narrow circumferential free-stream at the inner immersions. It is suspected that rake 3 installed in location 3 deviated from radial such that

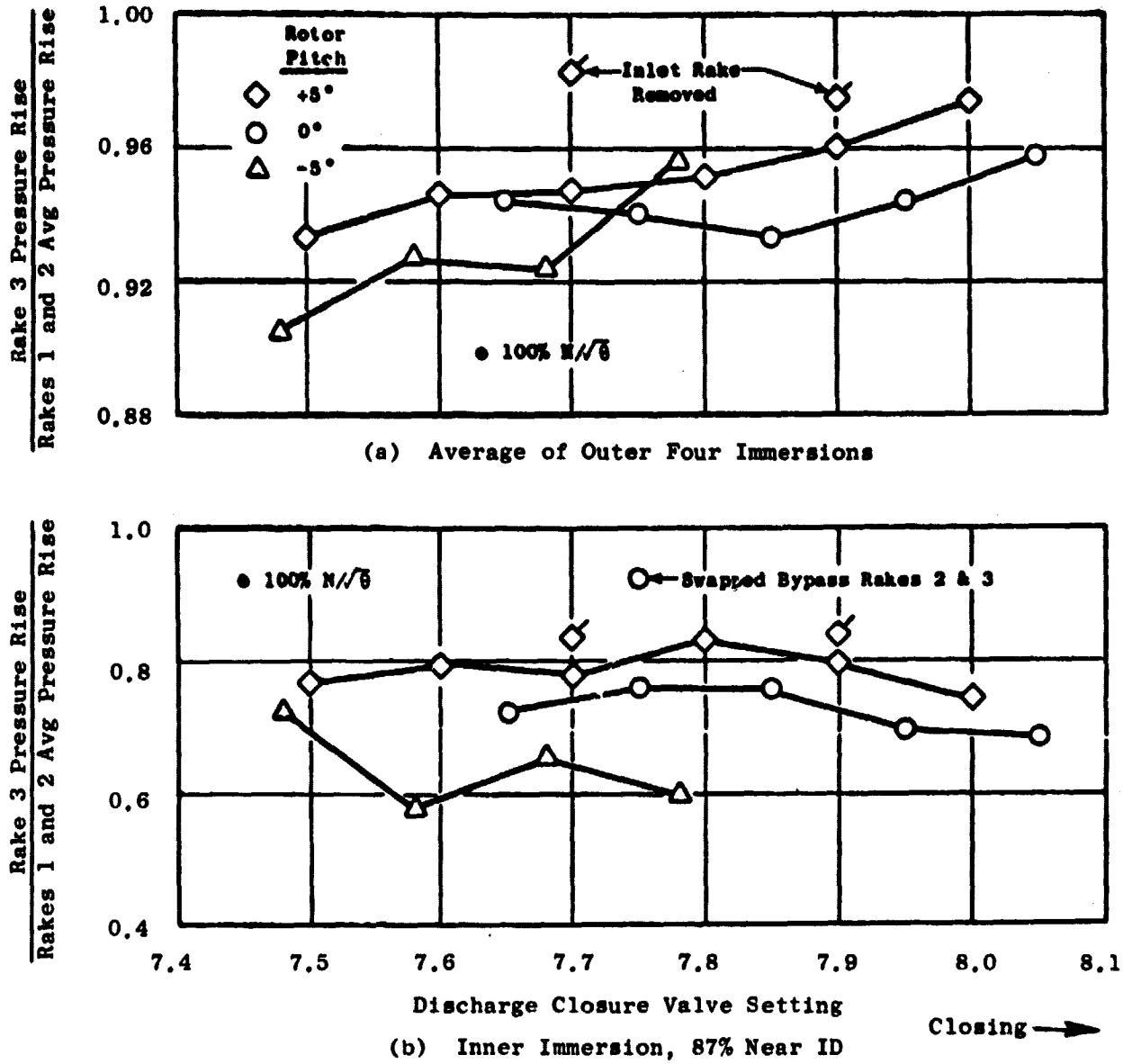

Figure 47. Pressure Measurement Discrepancies of Bypass OGV Rake 3 Relative to Rake 1 and 2 Averaged.

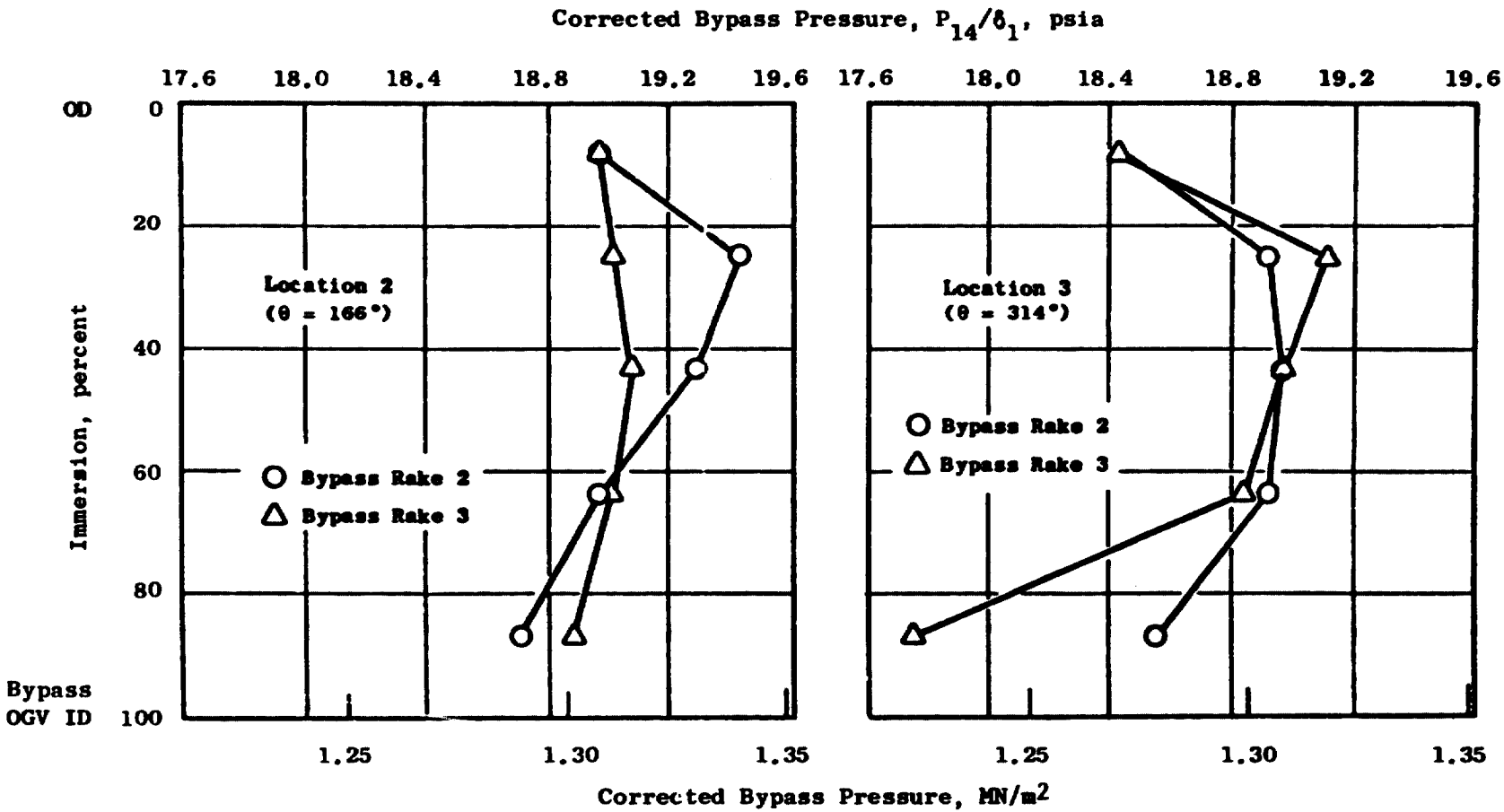

Figure 48. Effect of Interchanging Bypass OGV Rakes 2 and 3 on Pressure Measurement.

the inner element sensed the bypass vane wake rather than the free stream. Use of radial rake (Mode 1) data for rotor performance required the factoring out of any sensed vane wakes.

Adjustment to the fixed radial rake (Mode 1) data to account for the bypass rake 3 discrepancies was to set the overall rotor pressure rise at a level of 0.99 times the average of the pressure rise measured by rakes 1 and 2. In effect, this assigned to the third rake a level of 0.97 times the average of the pressure rise measured by rakes 1 and 2. The value of 0.97 was based on the measured level with the inlet rake removed (Figure 47). The effect of the adjustment was to increase the rotor pressure rise, the largest increase being for the -5° (open) blade angle and the smallest for the +5° (closed) blade angle. Adjusted rotor pressure rise versus DV characteristics are shown in Figure 49. Included for comparison is the rotor exit pressure rise deduced from the arc rake traverse data, shown with symbols. These results agreed well with the adjusted radial rake (Mode 1) data, shown as a solid line in Figure 49.

The next step was to adjust the radial rake (Mode 1) data for the bypass OGV total pressure loss to obtain overall stage performance over the range of test conditions. Figure 50 shows the bypass OGV loss versus discharge valve characteristics based on the arc rake traverse data. Some circumferential variation in loss was noted, with lower losses measured for the closed vane sets. This observation is consistent with the lower loadings for these vane sets. To obtain an overall bypass OGV loss, an average of the open 2 (design outlet flow angle of -10°) and closed 1 (design outlet flow angle of +5°) vane losses was used, since only those two traverse locations were common to the three rotor pitch angles tested.

Traverse data for each rotor pitch setting were usually limited to one speed, so a means of applying the OGV loss to the radial rake (Mode 1) data at all speeds was derived as follows: the overall OGV loss was nondimensionalized by the adjusted rotor total-pressure rise from radial rake data (Mode 1) at the same discharge valve closure setting and speed, and the resulting ratio of OGV loss/rotor total-pressure rise versus discharge valve closure setting curves, shown in Figure 51, were assumed to be applicable over the range of test conditions. As a check on this assumption, 90% and 105% corrected speed traverse points were compared to the curve derived from 100% corrected speed traverse data at the nominal rotor pitch setting. The comparison, shown in Figure 51, indicated satisfactory agreement.

A comparison of the stage total-pressure rise derived from the radial rake (Mode 1) data with the traverse stage data is shown in Figure 52. Agreement was good, as would be expected from the corresponding good agreement of the rotor exit results (Figure 49).

Final step in the map definition was to arrive at a best estimate of the stage efficiency, a task complicated by the following factors:

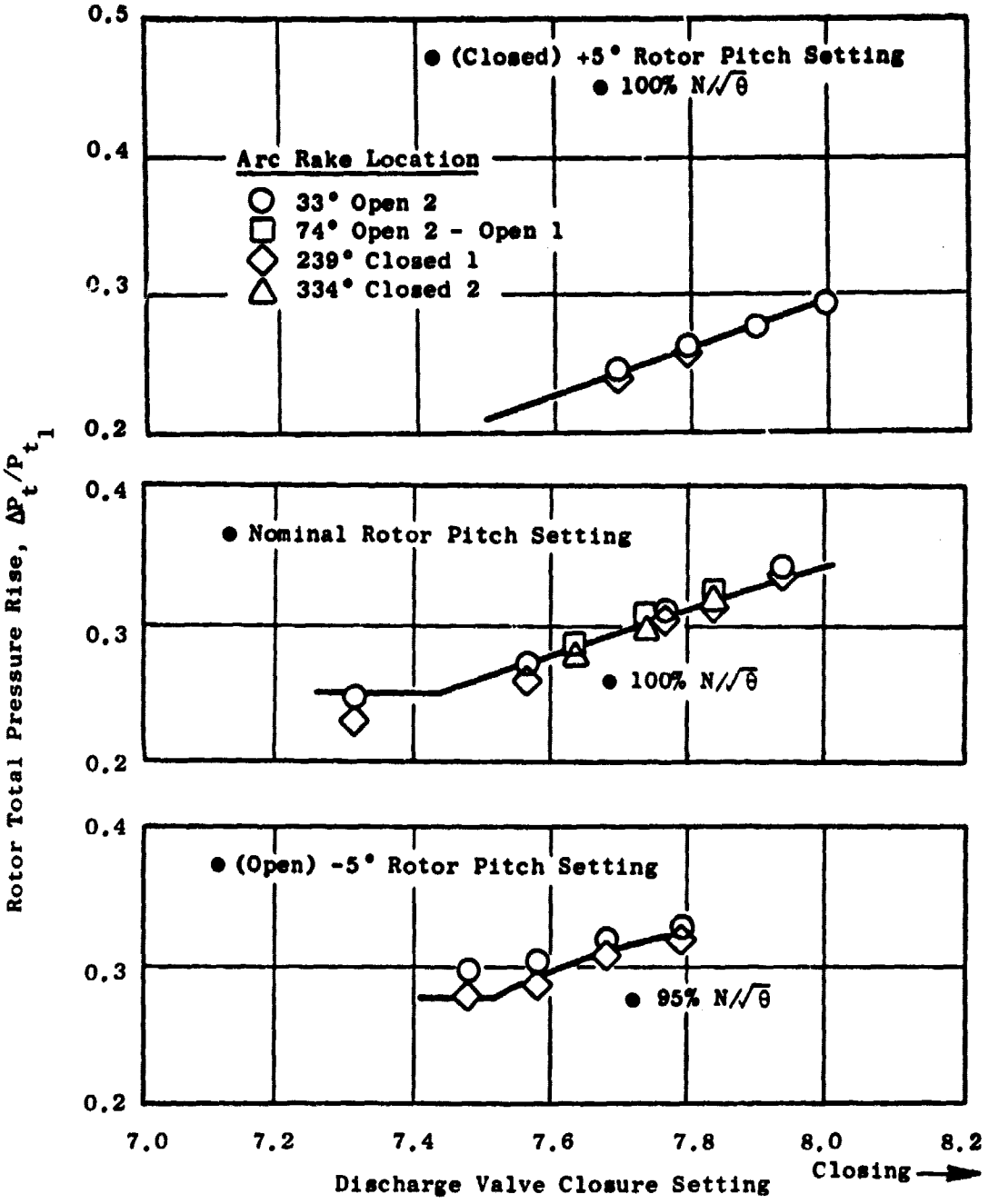

Figure 49. Rotor Total Pressure Rise Versus Discharge Valve Closure Setting.

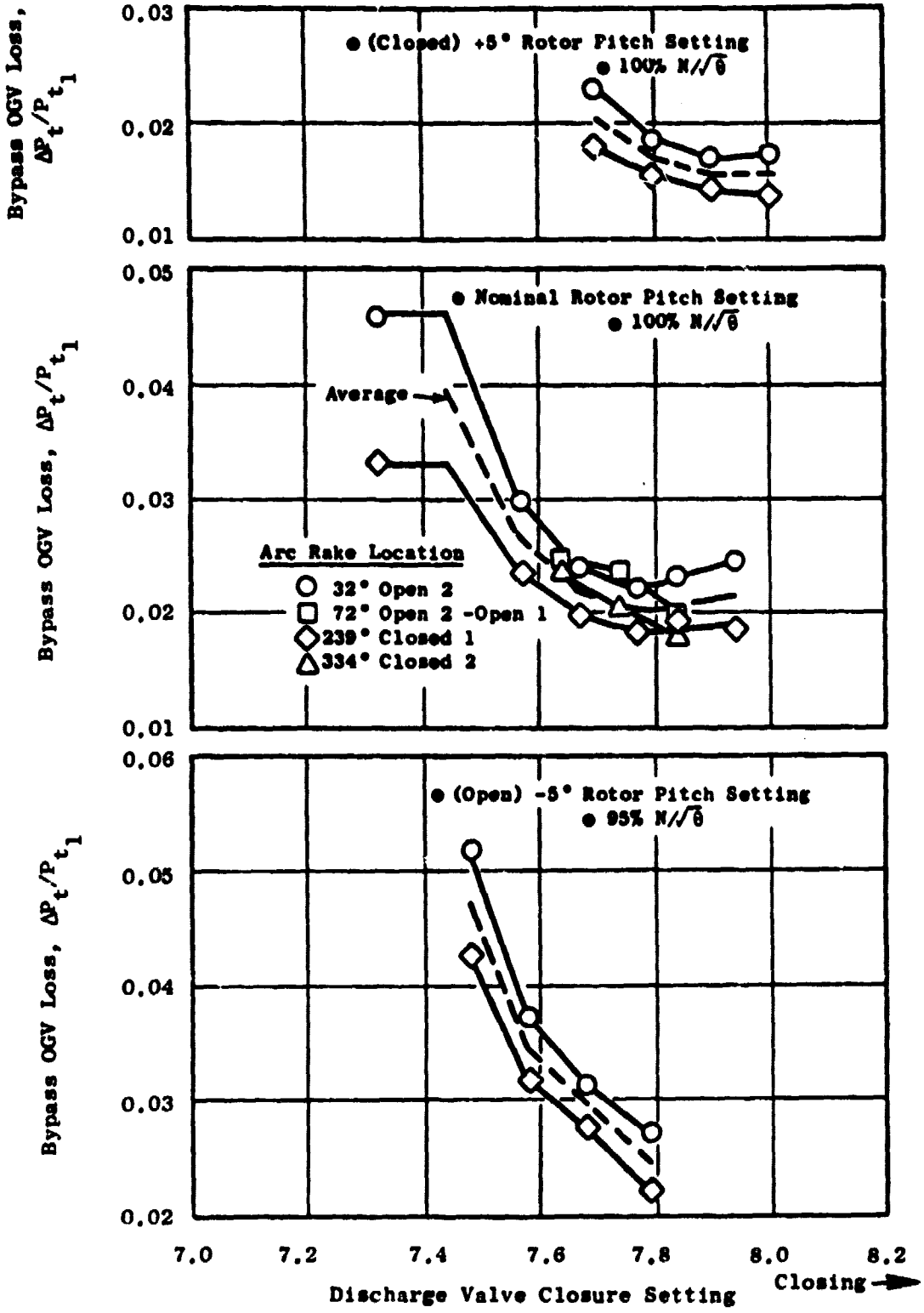

Figure 50. Bypass OGV Total Pressure Loss Versus Discharge Valve Closure Setting.

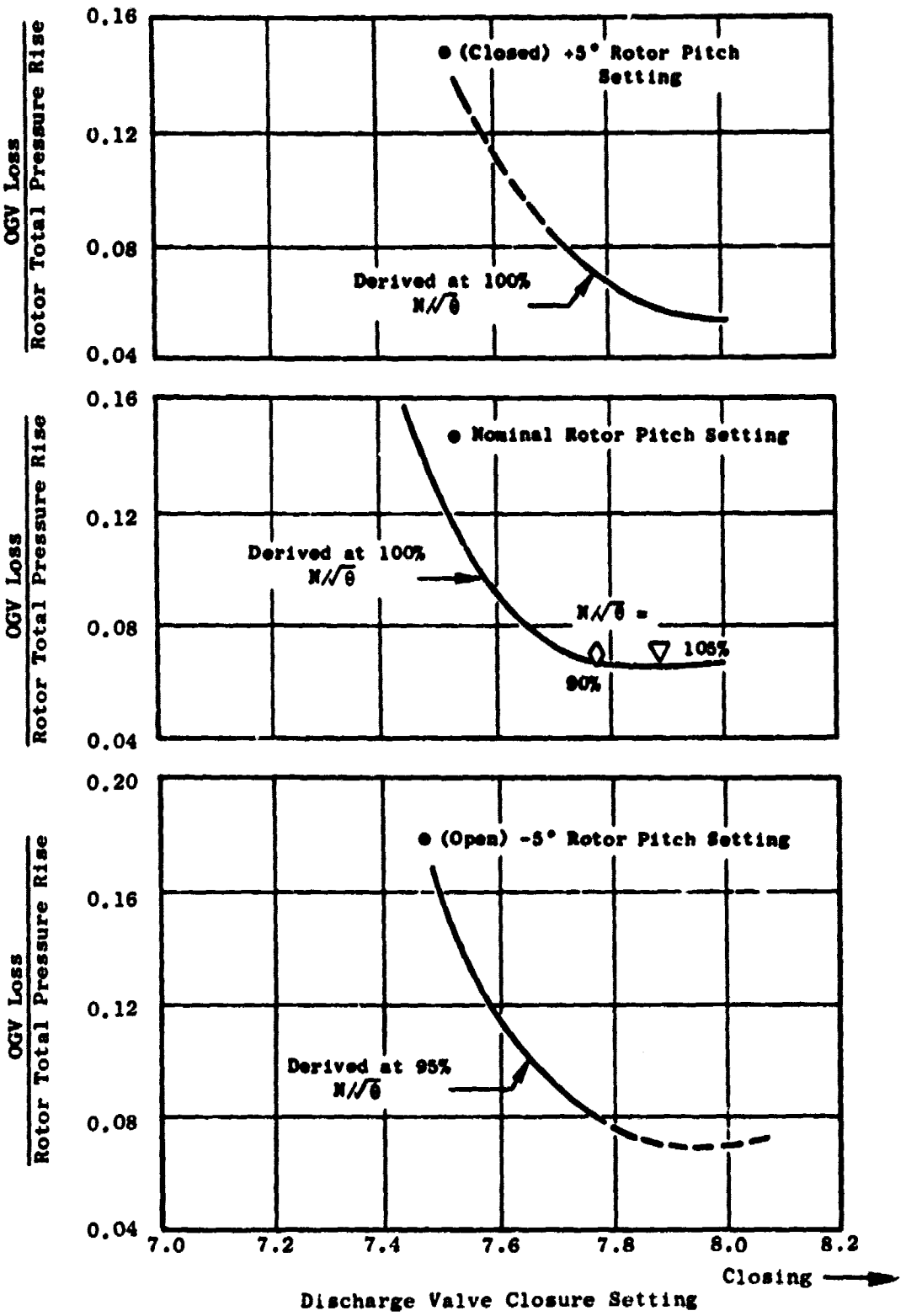

Figure 51. Nondimensionalized Bypass OGV Loss Versus Discharge Valve Closure Setting.

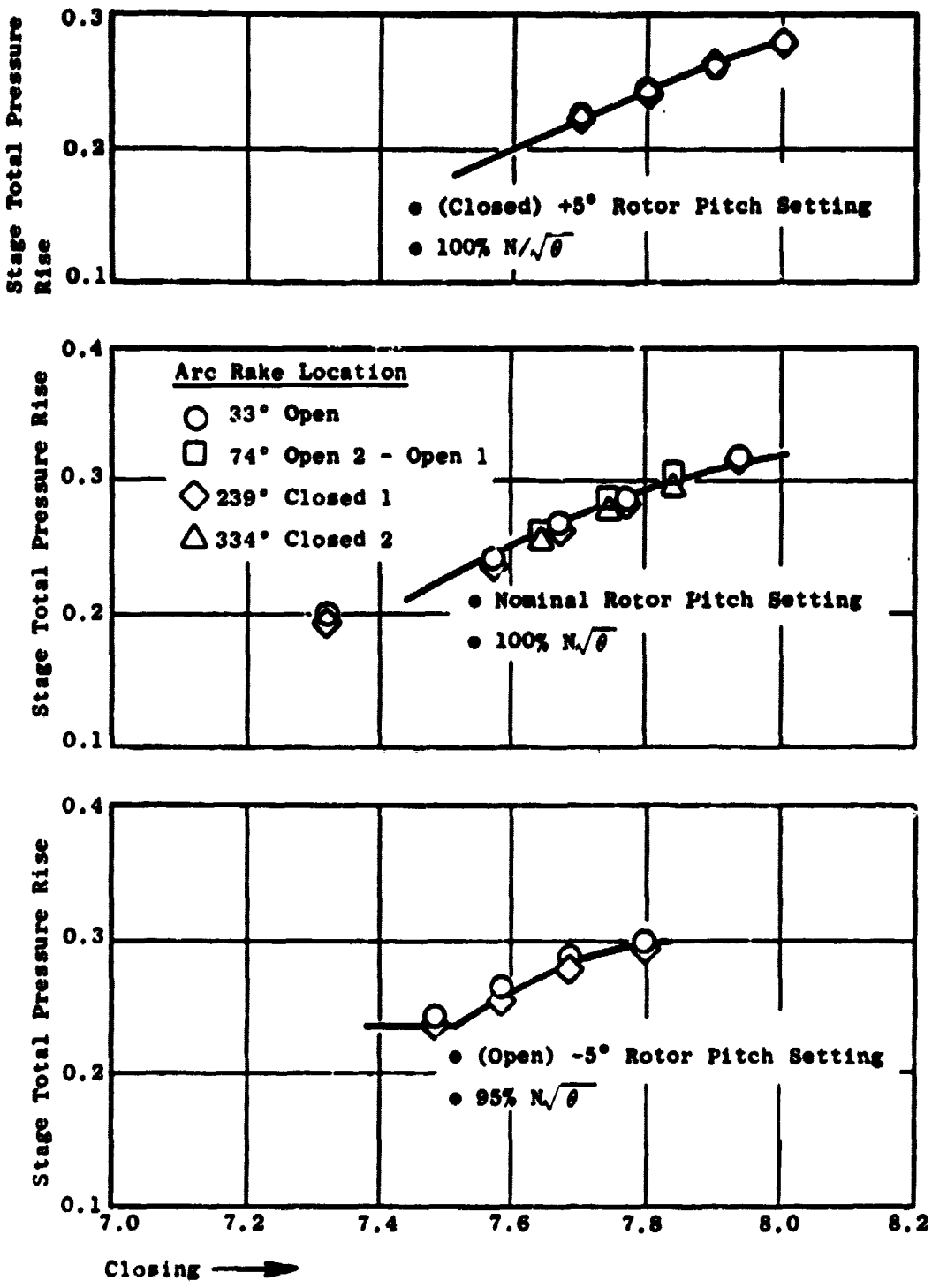

Figure 52. Stage Total Pressure Rise Versus Discharge Valve Closure Setting.

- Both radial and circumferential inlet temperature profiles existed, with variations from the average of about ±3°. A typical pattern is shown in Figure 53 at the fan inlet.

- A significant circumferential temperature variation across the individual vane frame passages was measured by the arc rake (Figure 27).

- The low overall temperature rise across the fan magnified the effect of any small temperature measurement errors on calculated efficiency.

Use of the radial rake (Mode 1) temperatures for efficiency determination had the advantage of being available over the entire aerodynamic test range, but lacked the accountability for the vane passage profile effects. The arc rake data provided a good weighted average across the vane passage, but had the disadvantage of being restricted to selected test conditions. Also, presumably due to the inlet temperature variation, a significant circumferential variation in rotor exit temperature was evident, as illustrated in Figure 54.

For the Mode 1 temperatures, the inlet-rake-wake rotor interaction might be expected to have some impact on the bypass rake 3 measurements. For the two cases with the inlet rake removed, it was observed that the rotor temperature rise measured by bypass rake 3 increased slightly at one DV setting and remained unchanged at the other DV setting. Because of the significant circumferential temperature nonuniformities occurring in the vehicle, it was concluded that a temperature adjustment similar to the pressure adjustment to account for the inlet-rake-wake effect was of dubious value. Accordingly, the fixed rake temperatures were used as is for efficiency calculations.

Figure 55 compares stage efficiency using pressure-adjusted fixed radial rake (Mode 1) rotor efficiency and bypass OGV loss (solid line) to stage efficiency calculated directly from the arc rake traverse (symbols). Relative to the arc rake levels, the fixed rake efficiencies are lower at -5° rotor pitch, higher at 0° pitch, and about the same at +5° pitch. The deduced, fixed-rake efficiencies result in a more realistic trend of peak efficiency versus pitch angle and consequently were adopted for map definition. Due to the aforementioned problems, however, some uncertainty remains relative to absolute efficiency levels.

FORWARD PITCH-HUB FLOW AERO MAP

Fan hub performance was deduced from measurements of total pressure and total temperature with radial rakes positioned between and aft of the core duct struts. In order to determine flow conditions at the core stator discharge plane, the plane at which fan hub performance is assumed in the engine cycle, a transition duct loss must be subtracted from the measured hub total pressure. A total-pressure-loss coefficient, equal to the value used in the engine cycle representation, was assumed for the transition duct. Duct pressure loss was then calculated for each data point from the measured duct

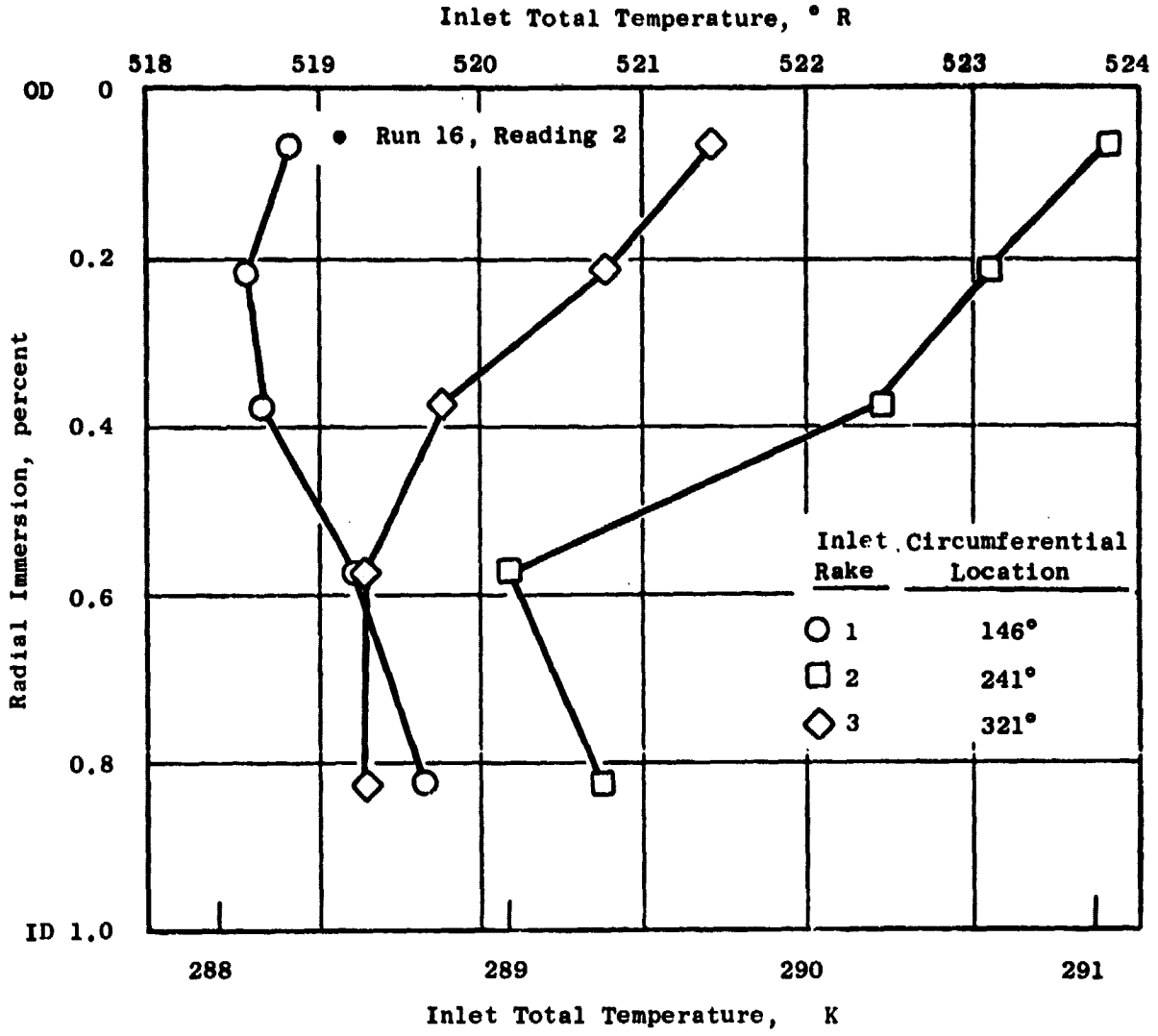

Figure 53. Typical Inlet Radial Total Temperature Distribution at 3 Circumferential Locations.

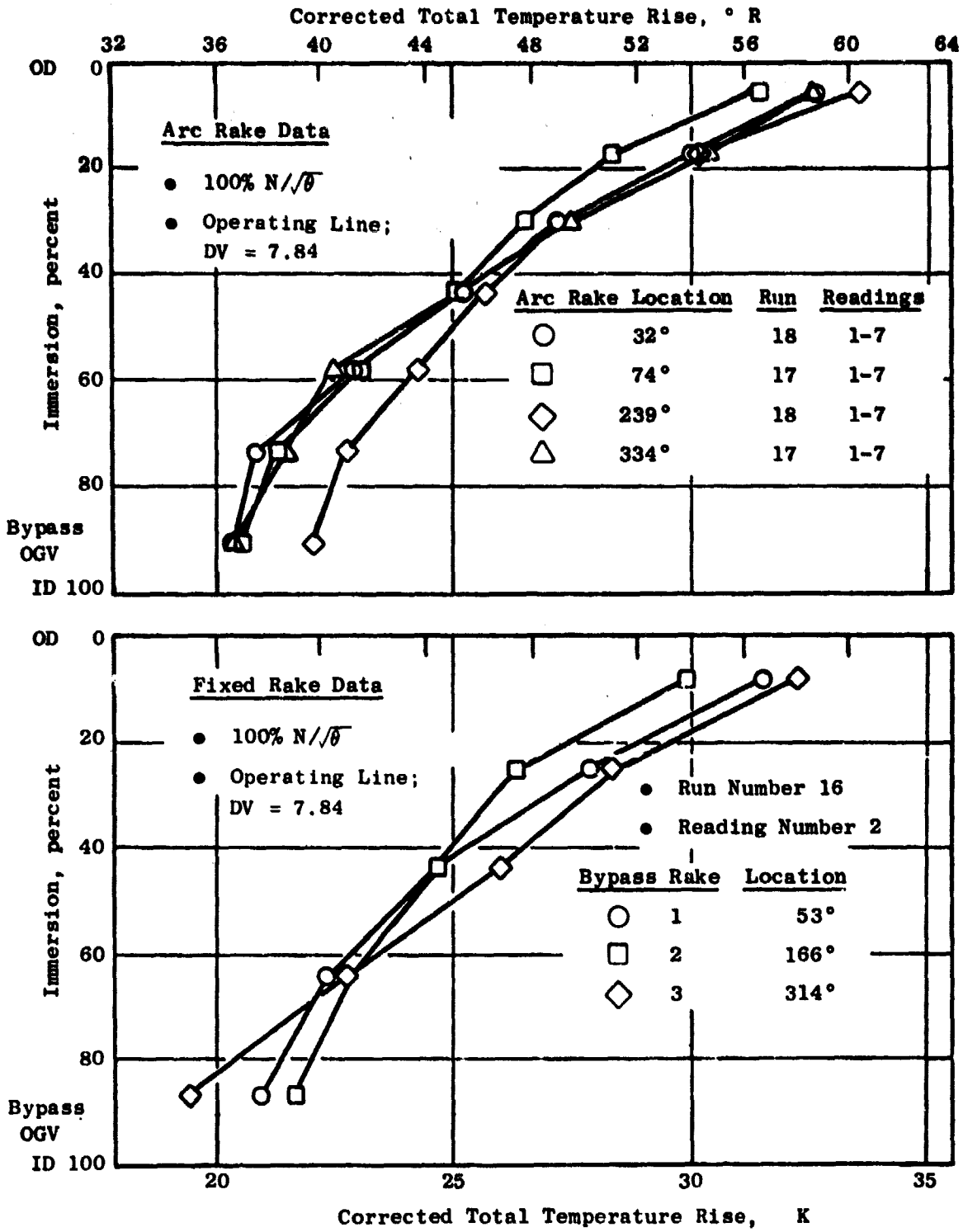

Figure 54. Rotor Exit Total Temperature Radial Profiles.

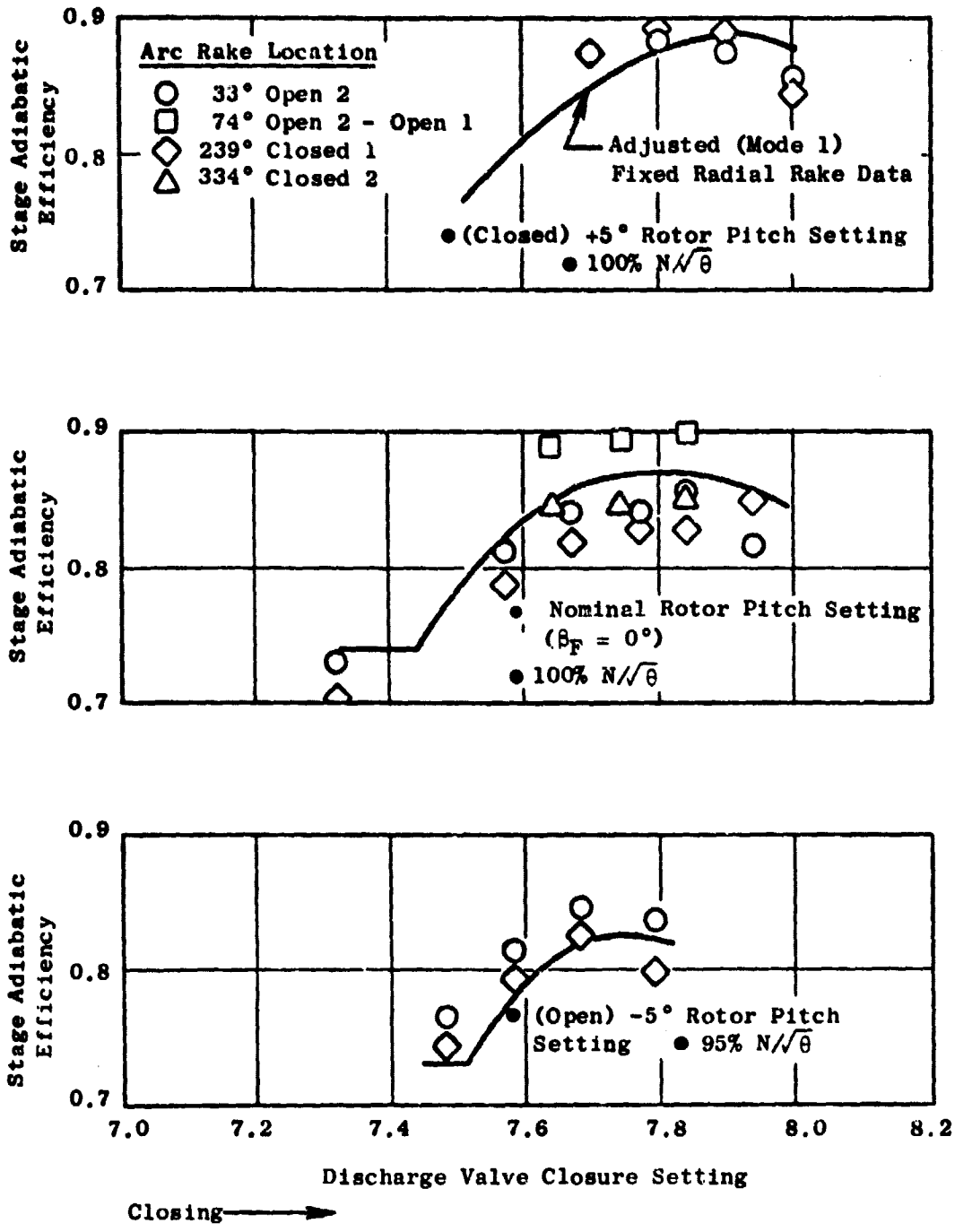

Figure 55. Stage Adiabatic Efficiency Versus Discharge Valve Closure Setting.

corrected flow. All measured total pressures were then adjusted upward by this calculated duct loss. Total temperature was assumed to be unchanged. Fan hub adiabatic efficiency was recalculated to reflect the higher total pressure. The method assumes these total pressures and total temperatures also apply to that portion of the fan hub flow not ingested by the core. The fan hub performance maps present the adjusted core data as representative of the fan hub flow passing below the island.

Representation of the fan hub performance in the UTW engine cycle is described in terms of modifying factors applied to the bypass stream performance maps. Details of the derived correlations for fan hub pressure ratio and efficiency are given in Reference 2.

REVERSE PITCH AERO MAP

Reverse pitch performance was obtained by the procedure outlined below:

- Fixed rake data were taken at several speeds per pitch setting. At a selected speed, the inlet throat was traversed with a wedge and a cobra probe to measure rotor exit total temperature, total and static pressures, and swirl profiles. The traverse data were integrated to obtain flow, thrust, and mass-weighted temperature and pressure. At the reverse-through-stall-pitch settings, the traverse-obtained rotor flow was found to be greater than the flow obtained by subtracting the core flow from the bypass duct calculated flow as illustrated below:

Pitch	Traverse Flow/Exlet Minus Core Flow
-95°	1.038
-100°	1.068
-105°	1.023
	1.043 avg

Possible sources of error in the bypass duct flow measurement include the assumption of an effective area coefficient of 0.97, the assumption of a radially constant total pressure numerically equal to the arithmetic average of the three, five-element radial rakes and the assumption of a radially constant static pressure numerically equal to the hub static pressure. Tip static pressures were excluded from the average because of the influence of local wall curvature. These static pressures read lower than at the hub, as expected. Since reverse thrust calculation utilized the traverse data solely, a multiplier of 1.043 was applied to the bypass duct minus core flow to improve the consistency between the flow maps and the thrust calculation.

- Rotor pressure and temperature rise measured by the fixed rakes were adjusted to agree with traverse results at the common speed. At other speeds, the same adjustment ratio was applied to the fixed rake data to complete the reverse pitch maps. Adjustment ratios are tabulated below:

Pitch Angle	$\frac{\Delta T_{traverse}}{\Delta T_{fixed\ rake}}$	$\frac{\Delta P_{traverse}}{\Delta P_{fixed\ rake}}$
-95°	0.9903	1.0036
-100°	0.9391	0.9455
-105°	0.9034	0.8727
+73°	0.8970	0.8381
+78°	0.8970	0.8381

This adjustment is required, not because of marked differences between traverse and fixed-rake pressures and temperatures at any given immersion, but because of the differences in weighting the immersion values to obtain an overall value. Mass-weighting was used in both cases, but different static pressures were used in determining the immersion weight flows. The chamber pressure (ambient) was used for the fixed-rake data, whereas the actual throat radial static profile was used for the traverse data. Since the actual throat static pressure was less than ambient and varied radially, differences in weighted values would be expected.

- At the reverse-through-flat-pitch settings, the cobra probe was inoperative, and total pressure and temperatures were obtained from the fixed-rake profiles at the standard cobra immersions. The immersion values were then mass-weighted using the wedge probe static pressures.

- Reverse thrust was determined by integrating the inlet throat axial momentum flux and pressure area terms across the throat and lip. These results were ratioed to the axial component of ideal thrust obtained by isentropic expansion of the rotor flow to ambient static pressure.

These results are summarized below:

Pitch	Integrated Thrust/Ideal Thrust X Cos (Exit Swirl)
-95°	0.9223
-100°	0.9438
-105°	0.8823
+73°	0.9161
	0.9161 avg

A relationship of these thrust ratios to the rotor flow ratios described earlier was noted; i.e., where the thrust ratio was high the flow ratio was also high. Accordingly, since an average of the flow ratios was used to adjust the rotor flow, an average of the thrust ratios was used to obtain the final reverse thrust values for all pitch settings.

APPENDIX C

AEROMECHANICAL CHARACTERISTICS OF THE UTW 50.8 cm (20 INCH) SIMULATOR FAN

BACKGROUND

This Appendix deals with the aeromechanical response characteristics of the NASA QCSEE 50.8 cm (20 inch) Under-the-Wing (UTW) Simulator Fan. This simulator fan was designed, built, and tested to provide early acoustic and aerodynamic data applicable to the design of the full-scale QCSEE UTW fan. The simulator fan blade shape and fan flowpath contours at 100% speed are a 20/71 scale of a full-size fan. This fan is shown in Figure 56.

The full-size version of the UTW fan is a flight weight, variable-pitch fan utilizing composite fan blades. This fan is capable of providing reverse thrust for braking by reversing the pitch angle of the blades. Reverse pitch can be accomplished through either open or closed pitch as indicated by Figure 2. The full-scale composite fan blades are mounted on titanium trunnions which are centrifugally restrained by ball-thrust bearings. The blade-pitch actuator is driven through a differential gear by a stationary hydraulic motor.

The simulator version of the UTW fan was designed to provide adjustable pitch blades but not variable when the fan is rotating. A single-piece titanium blade and trunnion replaces the two-piece composite and titanium full-scale design. This blade, with its associated mating components, is shown in Figure 57.

Within the program restraints of cost and timing, the aeromechanical characteristics of the simulator UTW fan were made as similar as possible to the full-scale fan. In addition to the similar blade and flowpath contours, the lower blade vibratory modes (after scaling) are very close to those predicted for the full-scale fan blades. The simulator fan disk is steel instead of titanium and employs a design concept and blade-to-disk stiffness ratio similar to the full-scale disk design. Some significant aeromechanical differences remain in these fans due to the different densities of the blade materials and different methods of blade retention. These differences will be discussed as they apply to the aeromechanical response of the simulator fan.

Dynamic strain gages were installed on blades of the simulator fan and were monitored during aerodynamic tests. Provisions for these gages have been made during the conceptual design of the rotor. This probably contributed to the excellent strain gage reliability during the tests in spite of the complexity and potential for lead-out damage in an adjustable-pitch fan.

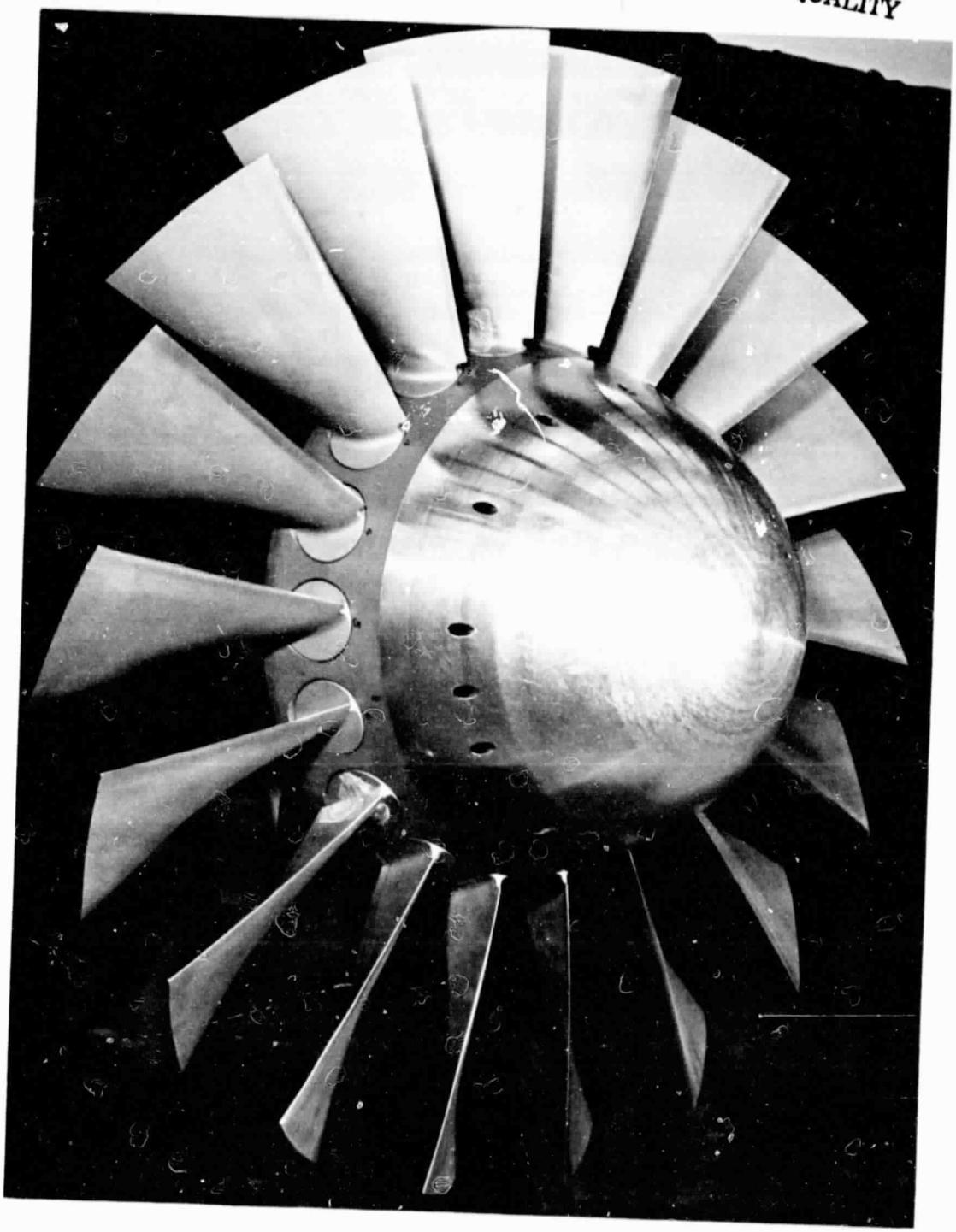

Figure 56. UTW 50.8 cm (20 inch) Variable-Pitch Fan.

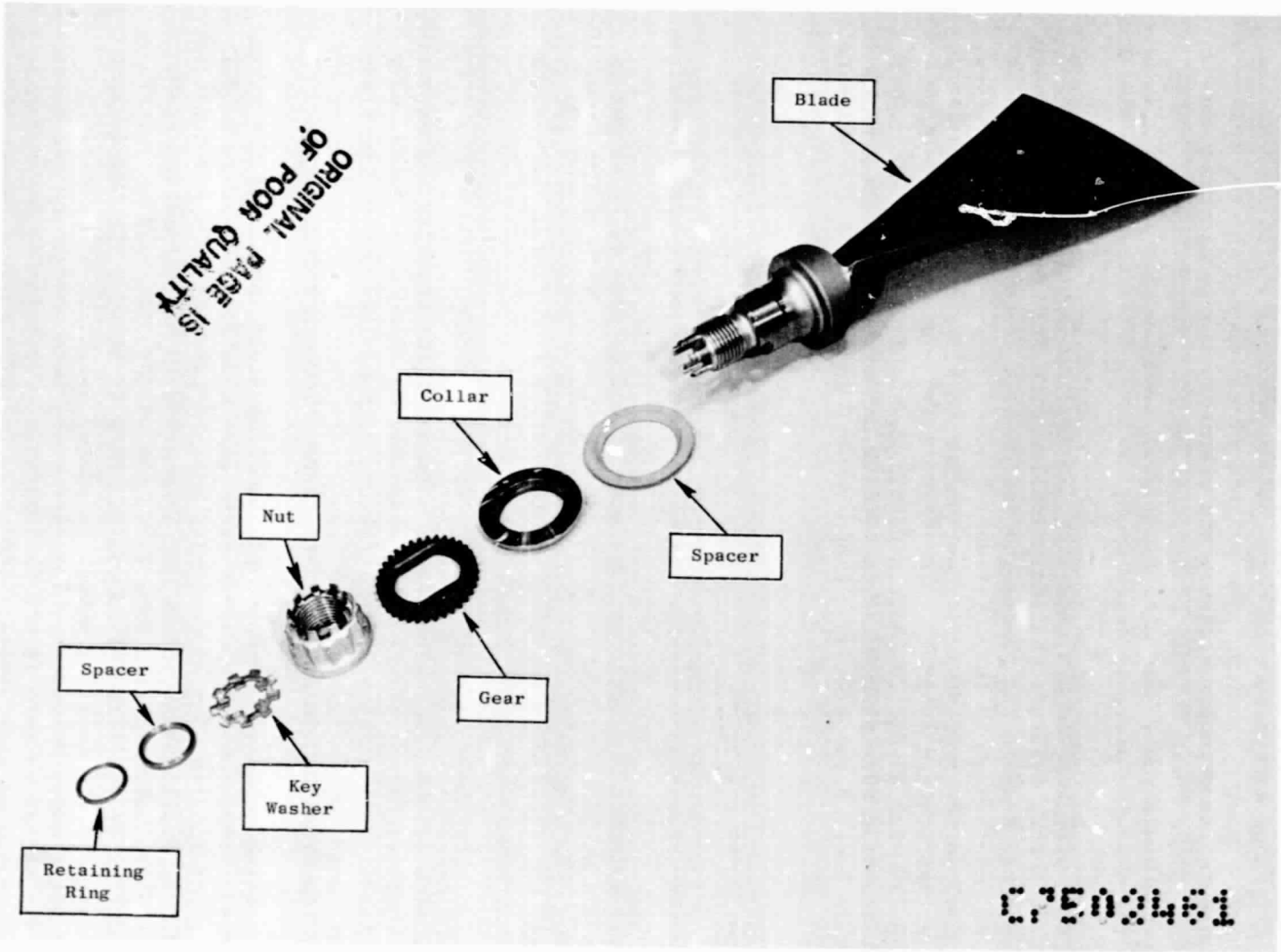

Figure 57. UTW 50.8 cm (20 inch) Fan Blade Hardware.

FAN BLADE FREQUENCY RESPONSE

UTW simulator fan blade frequency response, as measured in laboratory tests, was in good agreement with those values previously predicted by the Twisted-Blade computer program. The program is a cambered and twisted-beam program used for lower-mode frequency and vibratory stress distribution prediction. Since there is some blade cross section discontinuity in the region of the blade root, some analytical adjustment in this region was employed in line with previous experience.

The ring disk for the UTW simulator fan provides a stiff platform for the blade support. As predicted analytically, this disk did not contribute to a discernible drop in the blade-disk system mode frequencies over those measured in the laboratory for individual blades. These blade frequencies, as determined in the laboratory and during fan testing, are shown in Figure 58 and are tabulated in Table VI. The first axial mode on the simulator blade (690-770 cps) should not have a direct counterpart on the full-scale fan. The trunnion restraint locations and trunnion flexibilities that give rise to this mode on the simulator blade are not duplicated in the full-scale design.

STRAIN GAGE SCOPE LIMITS

Vibratory stress patterns for the blade vibratory modes were determined by laboratory tests. Based on these patterns, 3 strain gage locations on the blades were selected. These locations were picked so that at least one of the locations would be responsive to blade vibration in each of the lower 10-blade modes. Care was also taken to select locations where neither the strain gage nor its lead wires were likely to fail from fatigue before the blade.

"Scope limits", or vibratory stress limits for these gages, were calculated for each of the lower-blade modes. These limits normally represent the maximum vibratory stress at which the blade may be allowed to continuously vibrate without initiating a fatigue failure at some location on the blade. This point where the fatigue crack would be initiated is referred to as the "critical location" and is different for each vibratory mode.

The critical location depends upon both the steady state and the vibratory stress. Since the blade steady-state stress pattern increases roughly with the speed squared, the scope limits must be calculated as a function of fan speed. An additional complication is introduced in calculating scope limits for an adjustable pitch fan; i.e., the steady-state stress pattern is also a function of the blade pitch angle. This is because the aerodynamic blade loading and the twisting moment generated by the radial centrifugal field are pitch angle dependent. The effect of these changes on the blade steady-state stress pattern is not insignificant for a fan to be tested in a pitch angle range of approximately 180°. Technically correct blade scope limits would, therefore, require the calculating of a carpet of values as

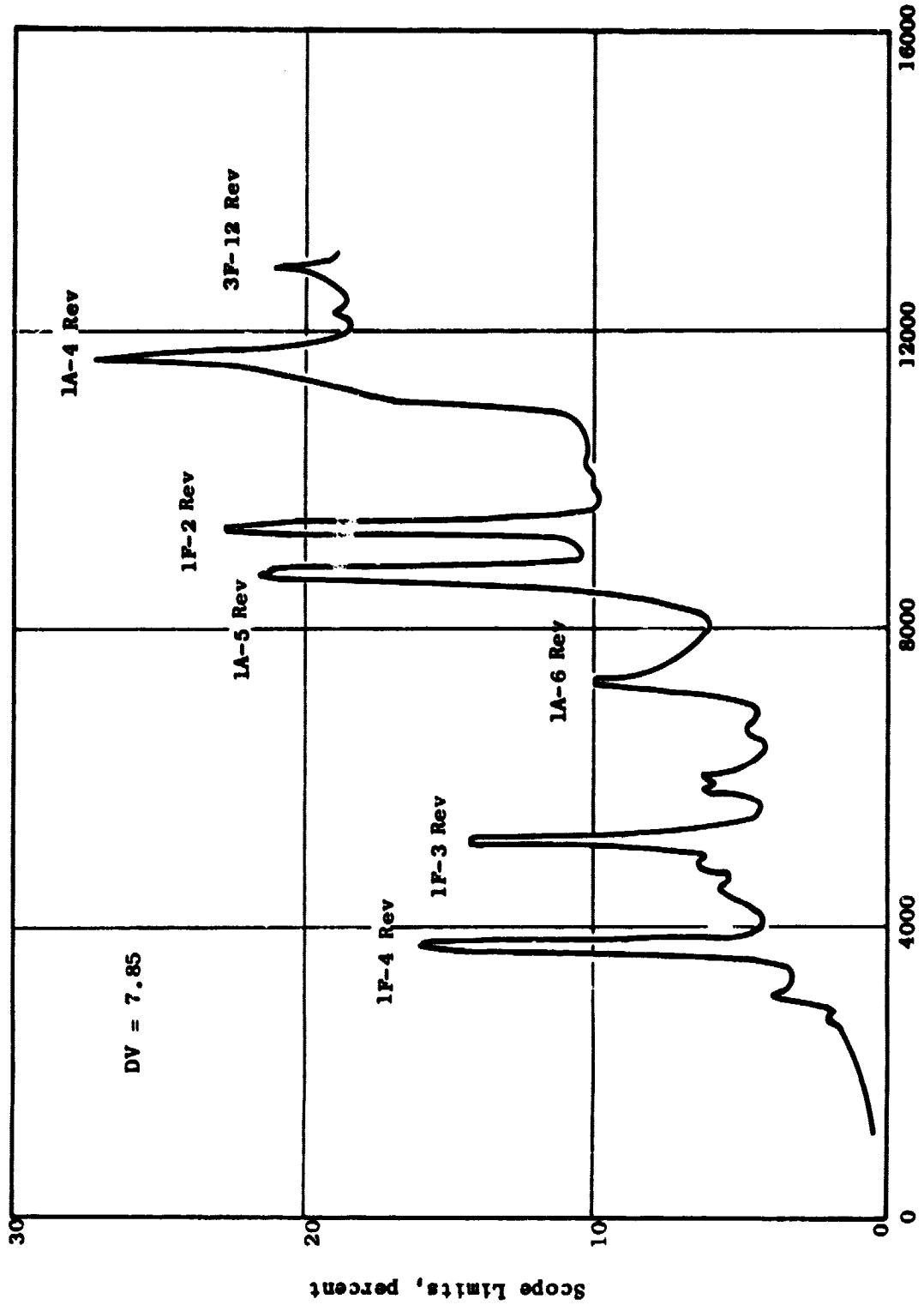

Figure 58. UTW Fan Simulator Vibratory Response with Nominal Blade Pitch, Inlet Bellmouth, Along the Operating Line (DW = 7.84).

Table VI. UTW Simulator Fan Blade Scope Limits.

KSI - Double Amplitude

Mode	Lab. Frequency CPS	Gage No.	Fan Speed			Critical Location
			9000	11516	13820	
1F	237	1	51.4	44.9	40.8	Root
		2	52.0	45.4	41.3	Convex Side
		3	52.6	45.9	41.8	Midchord
1A	690	1	46.4	40.3	37.4	Root
		2	25.3	21.9	20.4	Convex Side
		3	31.2	27.0	25.1	Midchord
1T	986	1	39.7	34.7	31.8	Root
		2	50.1	44.0	40.2	Concave Side
		3	25.1	22.0	20.1	Trailing Edge
2F	1242	1	30.3	28.5	25.5	Root
		2	57.0	47.0	40.3	Fillet
		3	38.2	32.5	29.1	Trailing Edge
3F	2358	1	26.4	23.6	21.2	Root
		2	64.0	57.0	51.3	Concave Side
		3	43.8	38.6	35.2	Trailing Edge
2T	2978	1	28.8	28.8	28.8	Tip
		2	10.8	10.8	10.8	Corner
		3	24.5	24.5	24.5	Trailing Edge

Higher Mode Scope Limits at 100% Speed (11516 rpm)

Mode		7th	8th	9th	10th
Lab. Frequency		3882	4631	5410	5628
Gate No.	1	6.5	31.8	0.7	15.4
	2	47.5	2.6	18.0	39.8
	3	12.2	29.2	4.3	4.2

a function of both speed and pitch angle. This approach was not taken because the extra precision in scope limits achieved was not felt to be worth the considerable effort required. Instead, the steady-state stress pattern for the blade was calculated based on the worst possible combination of aerodynamic and centrifugally induced loads for each blade location. This "dummy" steady-state stress pattern represents the highest steady-state stress possible at each blade location for any blade pitch angle at a given speed. For a given blade pitch angle, the real stress at a point could be equal to, but never greater than, the calculated dummy stress. This insures that the scope limits calculated using this dummy stress pattern would always be conservative.

Blade dummy steady-state stresses above the blade root were calculated using the Twisted-Blade computer program. To calculate the dummy stresses near the blade root, the worst components of moments and forces in this region were determined. Stress-influence coefficients (i.e., stress per unit load) due to these components were experimentally determined for many points in this region. Multiplying these stress-influence coefficients by the appropriate components of the loads and summing determined the dummy steady-state stress distribution.

With both the dummy steady-state stress pattern and the vibratory stress patterns known, the critical points for the various vibratory modes were determined using the fatigue-limit material properties diagram for the airfoil material (6-6-2 Titanium). The Fatigue Limit Diagram used was the average fatigue-limit curve minus three standard deviations which represents the minimum expected material properties.

With the critical point located, with the allowable vibratory stress at this location available, and with the vibratory stress pattern known, the scope limit for a particular airfoil strain gage may be calculated using the following equation:

$$\text{Scope limit} = \frac{2\,(\sigma_{\text{gage}}/\sigma_{\text{critical point}})\sigma_e}{K_1\,K_2\,K_3}$$

where,

σ_e = the single-amplitude endurance limit at the critical point on the blade in this vibratory mode, as determined by the Fatigue Limit Diagram for the blade material and the dummy steady-state stress at the location.

$\frac{\sigma_{\text{gage}}}{\sigma_{\text{critical point}}}$ = the ratio of the vibratory stress at the location of the strain gage to the vibratory stress at the critical point on the blade for the vibration mode being considered.

K_1 = a blade-to-blade vibratory response variation allowance factor (1.3, based on past experience).

K_2 = a factor for allowance for tolerance in the strain gage electronics circuit (1.05).

K_3 = an allowance for the sensitivity of the monitoring gage to slight changes in mode shape, such as might be expected due to manufacturing tolerance, 1/8" gage mislocation, etc. (1.22).

It is easier in practice to read a vibratory stress signal on an oscilloscope from peak-to-peak of the wave rather than its amplitude. Scope limits are, therefore, normally calculated in this manner. This peak-to-peak or double amplitude method of presenting scope limits is the reason behind the "two" in the numerator of the scope-limit equation. The scope limits for the QCSEE Simulator Fan blade are given in Table VI.

AEROMECHANICAL INSTRUMENTATION

1.	Rotor	- The rotor blades were instrumented with nine strain gages; eight were connected to the slip ring.
2.	Core Vanes	- The core vanes were instrumented with three strain gages.
3.	Inlet Rakes	- Three inlet rakes were instrumented with two gages each. Three gages, one from each rake, were monitored throughout all forward mode testing.
4.	Bypass Duct Rakes	- Three bypass duct rakes were instrumented with one gage each. All three gages were monitored throughout all reverse mode testing.
5.	14-Channel Recording and Monitoring System	- A 14 channel recording and monitoring system were sent out to CR&D on a loan basis for use throughout the Simulator Program.

The recording and monitoring system described comprises three racks of equipment on a dolly. Fourteen signals are amplified, presented for monitoring and analysis, and recorded. Each system consists of the following:

1. DC Power supply to excite strain gages.

2. Means for plugging in either strain gages or other signals.

3. Amplifiers to amplify transducer signals over the range of 5 to 5000 Hertz.

4. Probe scope monitor oscilloscopes to observe each of the 14 channels.

5. Over-stress indicators to light a warning lamp when any input exceeds a preset limit.

6. A 12.7 cm (5 inch) oscilloscope for more detailed examination of any signal.

7. A panoramic analyzer to display the frequencies of vibration, expediting analysis.

8. An audio oscillator, for accurate determination of frequencies which have been approximately measured on the panoramic analyzer.

9. A voltage calibrator to adjust amplifiers and recorder for accurate recordings.

10. A tape recorder, capable of recording up to 28 channels of information.

A strain gage connected to the transducer input panel is excited from a constant current supply. Self-generating transducer signals or other external signals may be fed into the transducer input panel through switching phone jacks, which removes excitation from the selected channel.

Each system contains all necessary calibrating equipment, internally wired to appropriate points, except for a means of checking FM oscillator frequency.

The weight of each system is 908 kg (2000 lbs). Overall dimensions including dolly and lifting hardware are: length, 213.4 cm (84"); width 76.2 cm (30"); height, 213.4 cm (84").

Each system requires a 30-ampere power service. All AC wiring in each system is insulated from the cabinets; the green lead in the 3-wire power cord is tied to the cabinets.

TEST PROGRAM

The UTW simulator fan was tested in the G.E. Research and Development Center's anechoic test facilities in Schenectady, New York. Forward and reverse blade orientations are depicted in Figure 2. Tests were conducted with forward pitch angles around the blade nominal position, open pitch angles in reverse thrust-thru-feather and closed pitch angles in reverse thrust-thru-flat pitch. The forward thrust pitch angles tested were -5°

(open), +5° (closed), and 0° nominal. The reverse thrust-thru-feather (open pitch) blade angles were -95°, -100°, and -105°. Two reverse thrust-thru-flat pitch (closed pitch) blade angles, +73° and +78°, were tested.

The fan was tested with a standard inlet and with an accelerating inlet. Both inlets were used in the forward thrust tests. Only the accelerating inlet configuration was utilized in reverse thrust tests. In reverse thrust, the fan "inlet" functioned as an exhaust nozzle.

Maximum physical fan speed encountered in tests was 113% of design speed in forward thrust and 114% of design speed in reverse thrust. The fan physical capability was not speed limiting. The 100% mechanical design speed point was 11,516 rpm.

Fan tests were also conducted with one inlet distortion pattern, a 16% tip radial, in the forward thrust mode, with the bellmouth inlet installed.

AEROMECHANICAL RESPONSE IN FORWARD THRUST

Nominal Pitch Angle Response

Aeromechanical blade stress response of the QCSEE UTW simulator fan remained below the scope limits throughout its normal operating environment. The response with a standard bellmouth is shown in Figure 58. In this configuration, the blade vibratory response was primarily due to the natural modes being forced at integral multiples of the rotor speed. These multiples are referred to as "per-revs" and blade response as "integral order response." These blade resonance responses can be predicted from the blade Campbell Diagram (Figure 59) where the blade frequencies cross the per rev frequencies. The maximum stress encountered was 27% of limits in a first axial mode resonance with 4 per-rev. Other significant first axial mode responses occurred in resonance with the 5th and 6th per-revs. This mode is not expected to be of significance on the full-scale UTW fan due to an axially stiffer blade retention system.

The 1st flexural mode was the blades' second most active mode. In resonance with 2 per-rev, the blade response reached 23% of limits at 82% speed (9400 rpm). Other significant blade 1st flexural resonances occurred with the 3rd and 4th per-revs.

Above 100% fan speed the maximum blade response was a 3rd flexural resonance with 12 per-rev. It reached 21% of scope limits.

The fan exhibited an unusual response to small changes in discharge valve closure settings. Blade vibratory stresses decreased slightly with increased throttling and increased when the throttling was reduced. This is the opposite of what might normally be expected. The maximum increase in stress when operating below the normal operating line was approximately 35%.

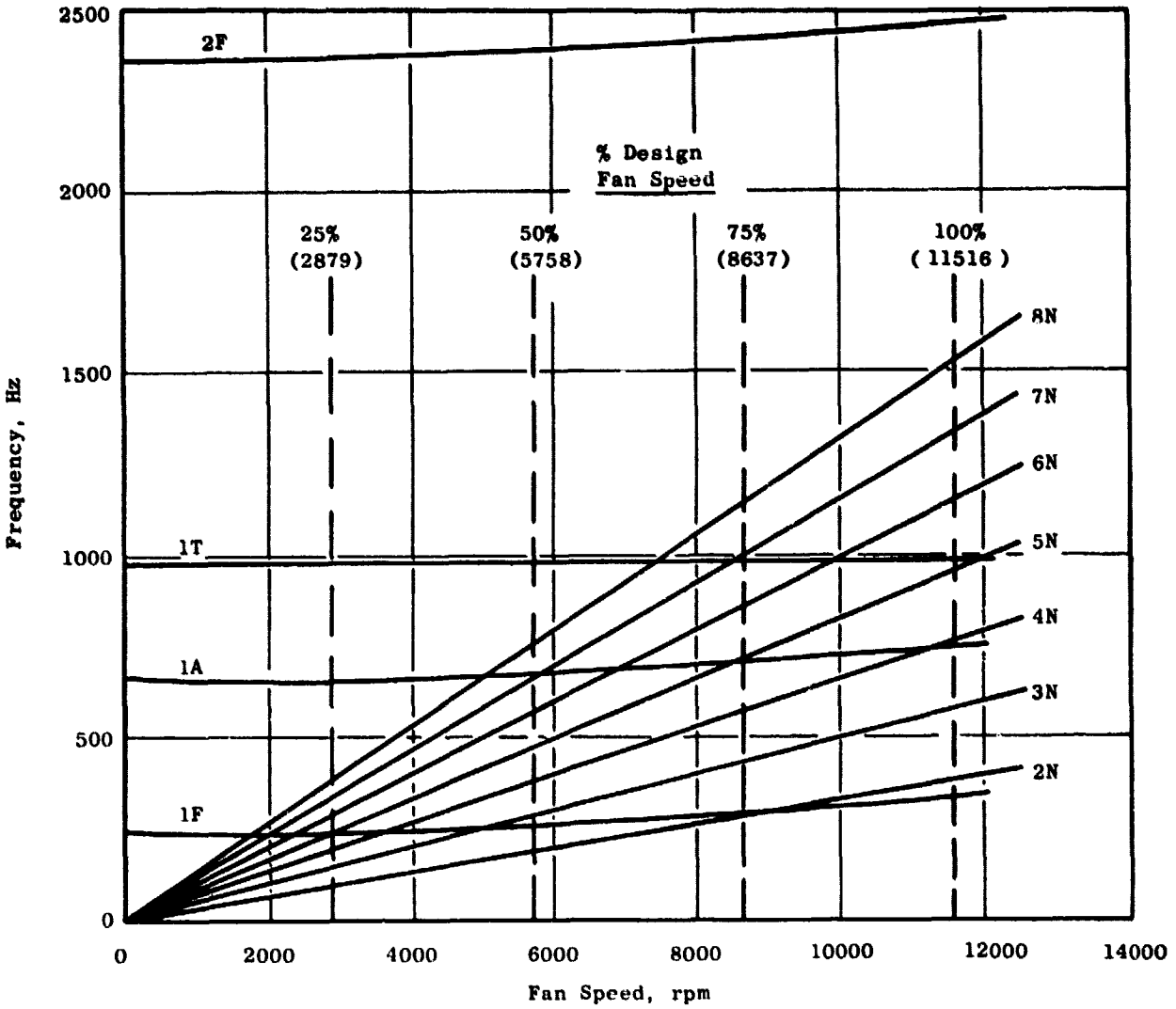

Figure 59. Campbell Diagram, UTW Simulator Fan Blade.

The 1st axial/4 per-rev and the 1st flexural/2 per-rev resonances reached a maximum of 31% and 34% percent of scope limits, respectively.

When the standard inlet was replaced by the accelerating inlet, the blade vibratory stress at corresponding speeds was higher. This inlet had the effect of broadening the resonance response peaks shown in Figure 58. While the blade stresses due to off-center resonances increased approximately 80%, the peak stress points only increased about 20%.

As with the standard inlet bellmouth, the blade stress with the accelerating inlet decreased slightly when the fan was lightly throttled and increased when the throttling was lowered. The 1st torsional/5 per-rev resonance, in particular, was greatly aggravated by lowering the back pressure on the fan with the accelerating inlet. While this resonance was not normally notable, the blade stresses in this mode would rise to 73% of limits on a low operating line at 106% fan speed.

The drop in blade stress with throttling occurred only in the region near the normal operating line. When throttling was continued above this line, the trend would reverse and blade stresses would rise as the stall line was approached. The fan with the accelerating inlet was throttled to "limiting conditions" in the range between 60% and 105% fan speed. The "limiting condition" was defined as either rotating stall or any form of blade excitation which would cause blade stresses to reach a level of concern for continuous operation.

Three different aeromechanical phenomena, including rotating stall, provided the limiting condition over the speed range tested. From 60% to 70% speed, the fan stresses reached 100% of scope limits prior to stall due to separated-flow induced vibration. Separated-flow vibration is normally encountered prior to stall, but it is unusual for it to cause such high blade stress in the intermediate speed range. It's particularly unusual for separated-flow vibration to decrease rather than increase near stall as the fan speed goes from the intermediate to the high speed range, as occurred with this fan. This phenomenon is not well understood, but there is apparently a large spectral energy content from the blade separated flow lying near the blade 1st flexural frequency in this speed range. This limiting condition was not reached until the fan was throttled very close to the projected stall line.

Rotating stall was the limiting condition when the fan was throttled at 80%, 90%, 100%, and 105% fan speeds. The peak blade stresses were near but did not exceed scope limits in these stalls. The blade separated-flow vibration was not as high near stall as had been experienced in the 60% to 70% fan speed range.

At 95% fan speed the limiting condition was blade limit cycle or blade "instability". The instability occurred in the 1st flexural mode with the blades in exactly the same nonintegral per-rev (1.82) frequency. The vibratory phase angle between any two of the three equally spaced strain-gaged

blades was constant and repeatable. This angle was not the same between different sets of these blades, however, and the apparent rotating nodal pattern could not be determined. Prior to stall at 90% fan speed, there had been signs of borderline instability. No indications of incipient instability were detected at 100% fan speed.

OFF-NOMINAL PITCH ANGLE RESPONSE IN FORWARD MODE

The QCSEE UTW simulator fan was tested with the blades at -5° (open) pitch and at +5° (closed) pitch in forward mode. These tests were not as extensive as those with the blade at nominal pitch and did not include stall tests. The standard bellmouth inlet was used with both pitch angles during the aeromechanical monitoring of this fan.

Based on the tests with the blades at nominal pitch, there were no aeromechanical surprises during the off-nominal pitch angle tests. As expected, the blade vibratory stress levels were slightly higher with the blades set at -5° (open) and slightly lower when at +5° (closed). Except for the stress magnitudes, however, the pattern of blade stress vs. fan speed with a nominal fan discharge setting was similar to that depicted for the nominal pitch in Figure 58. With the blade at -5° (open), the blade stresses were about 25% higher than at nominal pitch with the nominal fan discharge valve closure setting. With the blade pitch angle at +5° (closed), the stresses were about 20% lower than at nominal pitch.

With the blade pitch at -5° (open), the higher separated-flow blade vibration which occurs near the stall line (and, therefore, presumably at the stall line) occurs at a more open fan discharge valve closure setting than it did with the blades at nominal pitch. This is the expected result of flowing more air at a given fan discharge valve closure setting and fan speed. The reverse was, of course, true when the blade pitch angle was at +5° (closed).

AEROMECHANICAL RESPONSE IN REVERSE THRUST

Reverse-Through-Flat (Closed) Pitch

Two (closed) blade angles, +73° and +78°, were tested in reverse thrust. While more closed pitch angles could be expected to provide greater reverse thrust, they were not explored due to a serious aeromechanical problem encountered at +78° (closed) pitch. A first torsional "limit cycle" or blade instability was encountered which caused blade vibratory stresses to reach 85% of scope limits at 8080 rpm (70% physical fan speed). At this point the vibratory stresses were increasing rapidly with fan speed; higher speeds were not attempted.

The similarity shared by blade "instability" and separated-flow vibration made it difficult to determine the speed where the blade instability was

initiated. Both excite the blades at their natural frequencies which are generally nonintegral multiples of the pre-rev frequency. Instability is normally differentiated from separated-flow induced vibration by the wave form of the vibratory stress signal. When the blades are operated with a large negative incidence angle, as when they are reversed through flat pitch, separated-flow induced vibration is always a major contributor to the blade vibratory stress. The inception point of instability was not detected against this heavy background of separated-flow vibration.

First torsional vibration was a major contributor to the total blade stress at all speeds. Above 6500 rpm, the blade stress in this mode increased more rapidly and by 7000 rpm had the unmistakable wave form of blade instability. Between 7400 rpm and 8080 rpm the blade vibratory stress continued its rise from 32% to 85% of scope limits.

To clear the instability, the blade pitch angle was opened 5° to +73° (closed). At this angle the blade was free of instability up to the maximum speed tested (114% physical fan speed). The first torsional mode, excited by separated-flow vibration, was the more dominate vibratory mode at all speeds. The blade vibratory stress increased slowly with speed to a moderately sharp peak of 40% scope limits at 11400 rpm (99% speed). Above this speed the vibratory stress level dropped off with speed to 19% of scope limits at 13000 rpm (113% of design speed).

Reverse-Through-Feather (Open) Pitch

Three reverse-through-feather (open) blade angles were tested. They were -95°, -100°, and -105°. All three tests were aeromechanically successful in that no blade vibratory stress condition was encountered that would be of concern for continuous fan operation.

With all three reverse-through-feather blade pitch angles, reverse fan flow was established during acceleration from a standstill. The fan speed at which the stall was cleared was a function of the blade angle and the suction being applied to the core flow of the fan. This speed decreased with more open blade pitch angles and as the core suction was lowered (decreasing core flow). At -105° (open) pitch angle and with only modest core suction, it was possible to start the fan without stall being present. Table III summarizes the observations made of this transition phenomenon from stall to the "normal" type of reverse flow.

There was considerable aerodynamic hysteresis associated with the apparent reverse fan stall. Once the stall was cleared by speeding up the fan, the fan speed could be dropped as low as desired without reencountering stall. The speed at which the stall cleared also varied somewhat from trial-to-trial under fixed operating conditions. The range of the stall and the stall-free zones measured while accelerating the fan from a standstill is shown in Figure 60.

Air flow from the fan underwent a dramatic change between the apparent stalled and the unstalled condition. In the stalled condition the air issued

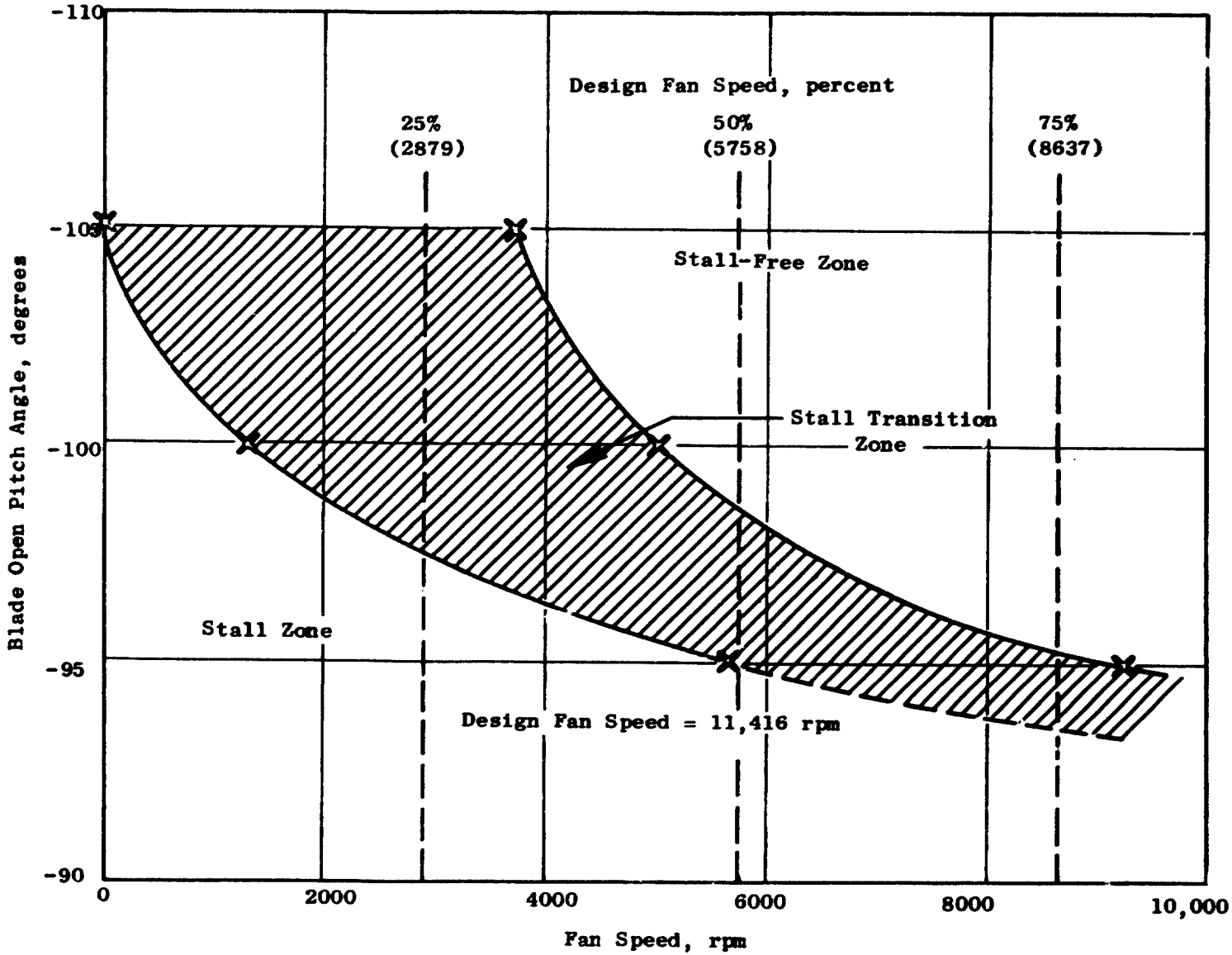

Figure 60. Range of Stall and Stall-Free Zones for the QCSEE Simulator Fan as Measured from Standstill to Operating Fan Speed, Reverse-Thru-Feather (Stall) Pitch.

from the accelerating "inlet" in the form of a large angled cone. Considerable radial flow was present. When the stall cleared, the flow reverted to a rather conventional-appearing nozzle flow with primarily axial flow and little radial flow.

In stall, the blade response was predominately in the 1st flexural mode. The vibratory stress was very random in amplitude as expected in a situation with considerable separated flow.

The maximum speed reached before the stall cleared was 9200 rpm (80% speed). This occurred during a trial with the blades -95° (open) and with heavy core suction (high core flow). Blade vibratory stresses reached approximately 80% of scope limits in isolated bursts. The stresses were very low up to 3600 rpm (31% speed). Between 3600 and 5000 rpm (43% speed) the stresses increased more rapidly to 40% of scope limits. Above 5000 rpm the stress increase with speed was more gradual. At a given speed setting in stall, there was no discernible difference in the blade stress level between the three different open pitch angles tested.

Blade stress levels dropped to lower values when the stall was cleared. The maximum stress encountered in the unstalled region was 40% of limits at 9670 rpm (84% speed) with the blades at -95° (open). The blade stress level dropped significantly when the blade pitch angle was opened from -95° to -100°. A further decrease in the stress levels was noted between -100° and -105°. The maximum vibratory stress levels in the unstalled region with the blades at -100° and -105° (open) pitch was 29% and 22%, respectively. These points occurred at 100% fan speed.

REFERENCES

1. Advanced Engineering and Technology Programs Department: Quiet Clean Short-Haul Experimental Engine (QCSEE). Under-the-Wing Final Design Report. NASA CR-134847, Unissued.

2. Advanced Engineering and Technology Programs Department: Quiet Clean Short-Haul Experimental Engine (QCSEE). The Aerodynamic and Mechanical Design of the QCSEE Under-the-Wing Fan. NASA CR-135009, March, 1977.

3. Advanced Engineering and Technology Programs Department: Quiet Clean Short-Haul Experimental Engine (QCSEE). UTW Fan Preliminary Design. NASA CR-134842, Febuary, 1975.

4. Advanced Engineering and Technology Programs Department: Quiet Clean Short-Haul Experimental Engine (QCSEE); Bilwakesh, Kashi R. and Clemons, Arthur. Acoustic Performance of a 50.8 cm (20 in.) Variable Pitch Fan and Inlet. Volume I. NASA CR-135117, Unissued.